A SCATTERED LIGHT PHOTOELASTIC ANALYSIS OF INTERLAMINAR MATRIX STRESSES IN FIBROUS COMPOSITE MODELS

A Thesis

Presented to

The Faculty of the Division of Graduate

Studies and Research

by

Robert W. Waddell Aderholdt

In Partial Fulfillment

of the Requirements for the Degree

Doctor of Philosophy in

The School of Engineering Science and Mechanics

Georgia Institute of Technology

December, 1973

A SCATTERED LIGHT PHOTOELASTIC ANALYSIS OF

INTERLAMINAR MATRIX STRESSES IN

FIBROUS COMPOSITE MODELS

Approved:

Chairman

Date approved by Chairman: 11-27-73

ACKNOWLEDGMENTS

It is a pleasure to acknowledge the contributions of the following:

Mr. M. G. Turner, who fabricated many of the experimental parts.

Dr. C. E. S. Ueng, for his suggestions on fiber orientation in the four-layer model.

Dr. S. L. Passman, with whom the authors had an interesting discussion on the nature of stress.

Mrs. Loretta Pharris, who typed this thesis.

Since the graphs and figures used in this work were originally a part of a report submitted to the National Science Foundation, special permission was received from the Graduate Division to use form of caption varying from that of the thesis manual.

TABLE OF CONTENTS

LIST OF TABLES

LIST OF ILLUSTRATIONS

SUMMARY

This project consists of a scattered light photoelastic analysis of stresses in the matrix of multilayered fiber composite models. Two tensile specimens are tested. The first contains two mutually normal layers of fibers which are approximately one half inch in diameter with a one inch spacing and permits solution for all components of the stress tensor in the region between the fiber layers. The second model is similar to the first, but contains four layers of approximately one quarter inch fibers for direct solution of matrix interlaminar shear stress. In both models fibers are oriented $\pm 45^{\circ}$ with respect to the tensile load.

Least-squares methods are used to utilize excess information available from the photoelastic data and the stress equilibrium equations. Dimensional analysis and specially devised molding techniques are used to produce the models.

The results indicate that matrix stress magnitudes are a function of proximity to the fibers and that they are significantly higher than the composite stresses commonly obtained using mathematical models.

CHAPTER I

INTRODUCTION

Composite Materials

The advantages of composite materials have been known and used for centuries[1]. Modern fiber reinforced composites generally consist of a layer or layers of very high strength, high modulus fibers embedded in a light weight, low modulus matrix. The combination of high strength and low weight has prompted continuing development of these materials for structural applications.

Of obvious critical importance for a material whose high strength is its greatest feature, is an understanding of the nature of its failure under load. Studies performed on single fibers and on multi-fiber composite specimens indicate that failure is a function of fiber and matrix strength characteristics, the bond strength between the fiber and the matrix, and the distribution of matrix shear stresses in the vicinity of the fiber[2,3]. In multilayer composites matrix stresses are found between the layers as well as between the fibers within each layer. An understanding of matrix stress distribution is considered to be important in understanding failure behavior of the material[4]. Of particular interest have been the interlaminar shear stresses (in planes normal to the layers)[5]. Theoretical models of composites have differed in the assumptions made regarding constituent composition and behavior and have yielded different results for the interlaminar shear stresses[6-10].

It is the objective of this research to examine experimentally the interlaminar matrix stresses in multilayer fiber composites.

Stress, Strain and Composite Materials

Fibrous composites are heterogeneous structures. The various elements of the structure (fibers and matrix) interact with each other at boundaries throughout the material.

To obtain a theoretical description of the internal stress distribution of a composite specimen, various mathematical models have been used. These models generally consist of a sandwich stack of plates[11]. The individual plates have different properties, associated with fiber layers or the interlaminar matrix. The fiber layers are assumed to be anisotropic, but homogeneous[12]. The anisotropy is stated with respect to direction for the mechanical properties (stiffness or compliance) of the layer. The layer is assumed to be homogeneous with respect to constituents from point to point within the layer. Not all analyses include an isotropic matrix layer between the orthotropic layers. Such region of matrix containing no fibers does exist in layered fiber composites as the fibers are ideally surrounded by matrix material.

Early classical laminated plate theory assumed that each orthotropic layer or plate contained plane stresses only[12,13]. The deficiencies of the stress distributions near the boundaries, prompted the use of analyses admitting stresses in planes normal to the layers. These stresses are often called interlaminar stresses. The various analyses have differed in their assumptions. They have alternately admitted only interlaminar shear stress[6], interlaminar normal stresses[7], and have con-

sidered the multilayered specimen as a three dimensional bounded solid with appropriate boundary conditions[8]. Stress variations normal to the plane have also been considered[9]. Various numerical approaches have been employed for formulating and solving these problems[8-10]. While the results have differed, all have shown that interlaminar shear stresses are present and are relatively high near the free edges of the layers.

Differences in the theoretical assumptions and results, their inevitably approximate nature, and the need to study stresses in specimens containing stress concentrations and other irregularities have spurred application of experimental methods of stress analysis to composite materials. In addition to the study of stress distributions throughout the field of the composite, experimental study has been given to stresses in the vicinity of individual fibers.

These experimental analyses have generally taken one of two directions: 1) Analyses using models of fibrous composites, or 2) Analyses using fibrous composite material specimens.

Use of fibrous composite models has permitted examination of the relative behavior of the fibers and the matrix. Most prominent has been the use of photoelastic models. These models have often been scaled up in size, but examination has also been performed using the small fibers with suitable magnifying instruments. Most experiments have been performed using transmitted light photoelasticity. (A discussion of photoelasticity follows in a later section.) Such tests have necessarily used plane models or models which have been analyzed as plane models. Examination has been performed to study shear stress distribution along a single fiber[14], and to determine the effect of fiber geometry and fiber

fracture on stress concentrations in the matrix[15-18]. The effect of load direction has also been examined[19]. Marloff and Daniel have studied shrinkage and load stresses in a three dimensional model using photoelastic freezing and slicing techniques[20]. Scattered light photoelastic techniques have been applied to composite models containing from one to three fibers[19,21]. A recent study by Rollins includes a two layered model containing an internal reflective surface to permit isolation of the transmitted light photoelastic effect in the two layers[22]. In addition to photoelastic experiments, models have also been used to observe dynamic fracture of composites[23], fiber to matrix deformation relationships[24], and composite failure[25].

Experimental methods used with composite specimens generally include measurement of surface effects; for the most part what has been considered to be strain. Measurements have been made using birefringent coatings[5,26-28], Moire fringes[5,27-31], and electrical resistance strain gages[5,28]. The strains thus determined are used with material properties for the various layers (assumed homogeneous) to determine stresses both on the surface and inside the specimen[5,27-31].

The use of these methods and the results and conclusions drawn from them suggest that a reconsideration of the traditional understanding of stress is in order. The stress vector (after Cauchy) is traditionally considered to be defined at a point in a continuous body as in[32,33]:

$$\vec{\sigma}_n = \lim_{\Delta A \to 0} \frac{\Delta \vec{F}_n}{\Delta A}$$

where ΔA is the surface area of an element in the body and ΔF_n is the force acting on this area. The subscript, n, denotes the direction of the normal to the area element. Or stress is the load intensity at the point taken with respect to an infinitesimally small area at the point. The implications for fibrous composites are significant insofar as these composites are structures consisting of many constituents. The stress at a given point in the structure must be understood in terms of the constituent at that point. Stated more directly, the stress in fibrous composites must be stated as being the stress in a fiber or in the matrix, whichever constituent occupies the point in question. The theoretical treatments[6-13] of stress distribution require no such restriction because the mathematical model consists of a sandwich of homogeneous, albeit anisotropic, plates. Within each plate, the stress may be spoken of without specifying the constituents at the point.

In addition to problems of definition of stress, the stress distribution within a small subregion consisting wholly of a single constituent will be influenced by the heterogeneous nature of the surrounding composite structure. Thus, stress magnitudes within the matrix, between fiber layers for example, will vary as a function of proximity to fibers specifically, rather than as a function of proximity to a fiber layer alone.

These stress analysis problems are inherent in the structure of the fibrous composite. They are important particularly from the standpoint of failure where the various failure modes are functions of fiber or matrix fracture or fiber to matrix separation. Any analysis of the interlaminar stresses in an actual multilayered fibrous composite must

include a reasonable modeling of the heterogeneous structure.

Study of strain in fibrous composites is subject to the same problems as is the study of stress. Strain[34] is understood in terms of deformation kinematics at a point in a structure. Strain in either of the constituents in a fibrous composite must be understood in terms of deformation experienced by that constituent in a sufficiently small vicinity of the point. While experimental methods for observing surface strain are sensitive to surface deformation over a large area, the assumption made to assure the validity of inferences regarding strain at a point is that this latter strain does not vary significantly from the "average strain" measured in the experiment. For structures which are homogeneous and continuous this assumption is usually true enough. For fibrous composites, strain can vary greatly from one constituent to another, as may be seen in scaled-up models[24]. Hence this assumption is valid only if the measurement method can discern these differences.

Experimental methods of strain measurement used with composite materials include electrical resistance strain gages, Moire fringes and birefringent coatings. These methods are generally insensitive to field variations of the order of magnitude of the fiber and/or fiber layer size. Thicknesses of photoelastic coatings used are too great (0.04 in.) to quantitatively discern the separate effects of motions in the matrix and in the fibers which have a separation smaller than 0.005 in. Strain gages must also be placed over several fibers. Even the use of embedded minature strain gages places the gage over 15 or more fibers. Moire fringes have been used both to observe large displacements and also local displacements due to matrix-fiber interactions. The average

strains measured over an area containing several fibers may vary greatly from strains at points in either the fiber or the matrix[24].

The above methods have been used to determine average strains on composite specimens and stress-strain relations for isotropic hemogeneous plate layers have been used to determine stresses[5,26,30]. The stresses which are so obtained are subject to a source of error other than local imprecision. Stress-strain relations commonly used are based on the constitutive equations for anisotropic solids[35]. These equations define the various anisotropic moduli in terms of stresses and strains. These moduli are determined using various mixing theories, or they are determined experimentally using total specimen loads and large field displacements[23,36-39], or stacked photoelastic models[40]. Moduli thus determined cannot be considered to give local stresses in terms of local loads in the tradition of Cauchy[33], even if these stresses are considered to be average values for the vicinity of the point in question. This is true because the constitutive equations and the moduli they include are formulated for a bounded structure different than that which is locally present (near the edges of the specimen for example). The local stresses in the composite structural layer are a function of the local load distribution alone.

The application of the constitutive equations for material properties when using anisotropic but homogeneous plate theory to study heterogeneous fibrous composites has been a valuable tool for study relationships between distributed loads and the resulting deformations. These methods cannot, as they have been applied, give accurate analysis

of actual composite strains and stresses*. It is the latter stresses which are important with respect to failure of fibrous composites. A study of such stresses as interlaminar should include a sufficiently accurate representation of the lamina structure.

In addition to the above-mentioned methods of strain analysis, Moire fringes have been used to study local strain in the vicinity of fibers near surfaces[41].

Also, there have been efforts to experimentally devise a stress-optic relationship for fibrous composites consisting of fibers and matrix having the same index of refraction[42-44]. Experiments have been performed to obtain isochromatic fringes showing correlation with the orthotropic stress-optic relationships devised. There has been no vector-optic derivation of any relationship between the two basic birefringent phenomena; rotation and retardation, and their photoelastic manifestations; isoclinic and isochromatic fringes. The stress optic-law quoted[44] is really a plane-stress idealization of one of the two "laws" of Neumann and Maxwell[45,46]. While this idealization may be valid for a unidirectional laminate, it can not be so for a bidirectional laminate.

---

*For an analogous example, a coil spring modulus is commonly considered as the ratio of normal load to normal spring deflection. This may be extended to "stress" (as the ratio load to gross cross sectional area of the coil) and "strain" (as the deflection divided by the free length of the spring). Such modulus would obviously not be useful to obtain yield stress from deflection for yielding of the spring. Such yield stress is found considering local torsional and flexural effects with the spring wire.

CHAPTER II

PHOTOELASTICITY; SCATTERED LIGHT

The photoelastic effect, which is widely used to study stress distributions in complex members, may best be stated in two laws formulated by Neumann and Maxwell[45]:

1. At any point in a stressed transparent solid the axes of polarization of light passing through the solid are parallel to the directions of the principal stresses in the plane of wave front at that point.*

2. The difference in the velocities of the two polarized rays at the point is proportional to the difference of these two principal stresses and is independent of the stresses perpendicular to the plane of the wavefront.*

This effect has traditionally been applied to engineering problems by studying the polarization changes produced in polarized monochromatic light which is transmitted through a two dimensional sheet of transparent elastic material containing stresses. In practice, the two dimensional model is placed between two polarizing filters, which have mutually orthogonal polarization directions. The polarization changes are manifested in a pattern of light and dark bands, or fringes, in the plane of the model.

Two types of fringes are present. The first type is associated with the first law. These consist of dark bands wherever the principal directions are aligned with the polarization directions of the filters.

---

*Neumann stated the effects as functions of strain rather than stress.

These fringes are isoclinics. The second type of fringe is associated with the second law. These fringes are called isochromatics and are due to the changes in the velocity difference. The isochromatics are related to the stress state by:

$$p - q = \frac{1}{c}\frac{n}{h} \tag{1}$$

where p and q are the principal stresses, c is the stress-optical material constant, h is the thickness of the model, and n is the fringe order, associated with the dark bands.

To study three dimensional models using transmitted light, stresses may be "frozen" into the models[47]. The models may then be sliced in various directions and these slices may be studied as two dimensional models. To analyze such slices Equation (1) may be rewritten:

$$p' - q' = \frac{1}{c}\frac{n}{h} \tag{2}$$

where p' and q' are the secondary principal stresses[48].

During the past several years increased use has been made of light which is scattered by a model when a polarized light beam is passed through it. It was first shown by Weller[49] that the interference patterns formed along the light beam path give information about stresses in planes perpendicular to the light beam. These interference patterns called fringes may be observed by viewing the light beam perpendicular to its propagation direction. It may be shown[50] that the time average intensity of light observed at a point of interest along the beam (Figure 1) is given by

$$I = \nu (\cos^2\theta \sin^2\beta - 2 \sin\theta \cos\theta \sin\beta \cos\beta \cos\psi + \sin^2\theta \cos^2\beta) \quad (3)$$

where ν is a scattering constant for the material, θ and β are given in Figure 1. ψ is the accumulated relative retardation of the light beam components caused by the secondary principal stress difference between the point where the light beam enters the material and the point of interest. The secondary principal stresses are in planes normal to the light beam.

For θ and β fixed it is seen that points of maximum intensity occur when $\cos\psi = -1$ (eq. 3) or $\Psi = m\pi$, m = 1,3,5... and minimum intensity occurs when $\cos\Psi = 1$ or $\psi = m\pi$, m = 0,2,4.... Points where $\cos\psi = 1$ are called whole order fringes and points where $\cos\psi = -1$ are called half order fringes. It may be shown that for the case where one of the secondary principal directions passes between the polarization direction and observation direction, the half order fringes will be minimum intensity points and the whole order fringes will be points of maximum intensity.

The stress optic laws previously mentioned may be related to the observed effects using scattered light. The first of the laws concerns the direction of the secondary principal stresses and the polarized light components at the point. This effect is manifested in the variation of fringe clarity with θ and β. (If θ and/or β are zero, there are no fringes). Methods have been developed[51,52] to determine the secondary principal directions.

The second law is found quantitatively in:

$$p' - q' = \frac{1}{c} \frac{dn}{ds}$$

where p' and q' are the maximum and minimum secondary principal stresses, s is the distance along the light beam path and n is fringe order.

Therefore from scattered light photoelasticity the directions and the difference in magnitude of the secondary principal stresses may be found. From these values the normal stress difference and the shear stress may be determined for a given coordinate system:

$$\sigma_x - \sigma_y = (p' - q') \cos 2\theta = \frac{1}{c} \frac{dn}{dz} \cos 2\theta_z \tag{4}$$

$$\tau_{xy} = \frac{1}{2} (p' - q') \sin 2\theta = \frac{1}{2c} \frac{dn}{dz} \sin 2\theta_z \tag{5}$$

where the light beam is directed along the z axis and θ_z is measured with respect to the x axis. For light passage in the x direction:

$$\sigma_y - \sigma_z = \frac{1}{c} \frac{dn}{dx} \cos 2\theta_x \tag{6}$$

$$\tau_{yz} = \frac{1}{2c} \frac{dn}{dx} \sin 2\theta_x \tag{7}$$

where θ_x is measured with respect to the y axis. For light passage in the y direction:

$$\sigma_z - \sigma_x = \frac{1}{c} \frac{dn}{dy} \cos 2\theta_y \tag{8}$$

$$\tau_{xy} = \frac{1}{2c} \frac{dn}{dy} \sin 2\theta_y \tag{9}$$

Although these six equations (eqs. 4-9) contain experimental information relating the six stress tensor components, the equations are not independent because

$$\sigma_x - \sigma_z = (\sigma_x - \sigma_y) + (\sigma_y - \sigma_z) \tag{10}$$

Additional independent information is provided by the stress equilibrium equations and by the boundary conditions at a free surface.

The stress-equilibrium equations are often used in finite difference form. This process, called the shear difference method, was developed for transmitted light work in three dimensional problems[53] and has also been adapted for scattered light analysis[54].

Scattered light photoelasticity requires a highly columnated, monochromatic light source of high intensity. It is also necessary that the emitted light beam have a relatively small diameter so that information at points along the beam may be obtained. The light produced by the laser has been found to be ideally suited for scattered light investigations[55]. The polariscope used in this experiment employed a continuous wave helium-neon laser for the light source. The light emitted was in the visible red range (wave length = 6328 angstroms). The features of the polariscope are described in a later section.

Scattered light photoelasticity has many distinct advantages for studying stresses in fiber composite models. The thermal stresses which would be associated with the stress freezing of three-dimensional transmitted light analysis are avoided in the heterogeneous model. Stresses and other ill effects associated with slicing such models are also avoided. The model need not be destroyed and can be used again. The load on the model can be an experiment variable.

CHAPTER III

PHOTOELASTIC MODELS

Because of the small fiber spacing in actual glass-resin composites, the use of photoelastic techniques in the interlaminar regions is almost impossible. Therefore, in order to carry out a photoelastic analysis of the interlaminar stresses, scale models of typical fibrous composite elements were fabricated. The choice of the particular models used in this study was based on previous composite investigations, similarity to real fibrous composites, and the relative ease in obtaining the photoelastic data.

Two different models were constructed. The first contained only two fiber layers, separated sufficiently to permit a fairly thorough investigation of the total stress tensor in the matrix region between the fiber layers. The second model contained four fiber layers and was constructed to examine the interlaminar shear stress.

Based on the studies previously referenced, it was decided that a fibrous composite element, subjected to an in-plane state of stress, would be sufficiently general to justify this investigation. As pointed out by Azzi and Tsai[36], a general state of in-plane stresses in a composite may be attained by the application of a tensile load in a direction other than one of the "natural axes" of the composite. The natural axes of a fibrous composite layer are parallel and perpendicular to the fiber directions. For example, the natural axes for the two-layer model are the x and y axes for either layer (see Figure 2). The coordinates

and fiber orientations chosen for the models constructed in this study are practically the same as those of previous investigations.

A load frame was designed and fabricated so that a tensile load could be applied to the models in the desired direction. The design provided maximum visual access and sufficient strength and rigidity. Figure 3 shows the load frame with the two-layer model installed. Spherical seats were machined in the two rectangular bars at either end of the frame to match spherically shaped bolt heads, in order to transmit a pure tensile load to the model. A strain gage was attached to one of the end plates of the load frame, then the entire frame was calibrated with the aid of tensile testing machine. Because the load frame was calibrated, the load on the model could be continuously monitored by the use of a strain indicator. Thus during set up and data taking, it was possible to determine early whether the load on the model had changed. Over a period of about five hours, a load relaxation of approximately one percent was noted. This was thought to be due to the creep behavior exhibited by most epoxy resins.

The fiber spacing (center to center) in each case (two-layer and four-layer designs) was chosen to be about equal to twice the fiber diameter. For the complete solution desired in the two-layer model, a fiber spacing of one inch was found to be satisfactory. With this fiber spacing sufficient data could be extracted at the points of interest. Although transparent, the models were optically as well as physically inhomogeneous. In photoelasticity it is necessary to pass light through the models in various directions. The light beam was distorted when passed through a fiber. Therefore, when the light was directed in the

z direction, an incomplete set of data was obtained at points between the fiber intersections. Stresses at these hidden points were found, however, because of the solution method employed. The differences in the indices of refraction of the glass fibers and the epoxy matrix also occasionally caused undesirable reflections of the light beam. By changing the observation direction, viewing of the reflections could be eliminated.

Dimensional Analysis

Dimensional analysis is summarized by Buckingham's theorem: "If an equation is dimensionally homogeneous, it can be reduced to a relationship among a complete set of dimensionless products"[56]. A dimensionally homogeneous equation is one having the same form regardless of the fundamental units of measurement employed. Then according to Buckingham's theorem an equation such as

$$y = g\ (x_1, x_2, \ldots, x_\ell) \tag{11}$$

can be reduced to an equation of the form

$$\pi_1 = f\ (\pi_2, \pi_3, \ldots, \pi_m) \tag{12}$$

where $\pi_1 \ldots \pi_m$ constitute a complete set of dimensionless products (π terms) of the variables $y, x_1, x_2, \ldots, x_\ell$. Any of the π terms may be represented as a function of the other $(m - 1)$ π terms. Model study utilizes the fact that the function f depends only on the dimensionless products $\pi_2 \ldots \pi_m$, so that:

$$\pi_{1_{Pr}} = \pi_{1_{Mo}}$$

$$\text{if} \qquad \pi_{i_{Pr}} = \pi_{i_{Mo}} \qquad i = 2, \ldots, m, \tag{13}$$

where the subscripts Pr and Mo denote the prototype and model respectively. By arranging the π terms such that π_1 contains the variable of interest (dependent variable), the behavior of this variable in the prototype may be studied by testing a model constructed such that all the remaining π terms are matched.

The complete set of dimensionless products can be determined systematically as discussed by Langhaar[56]. Accordingly, the first step is to decide what independent variables, $x_1, \ldots, x_\ell$, affect the dependent variable y. Next the dimensional matrix is formed and its rank, r, computed. The dimensional matrix consists of an array of the exponents of the fundamental units of the dependent and independent variables. The rank is defined as the order of the largest non-zero determinant contained within the dimensional matrix. If there are k variables (including the dependent variables), then k - r dimensionless products constitute a complete set.

In the case of elastic deformation of a composite, assuming the dependent variable to be a stress component σ_{ij}, the independent variables are:

Fiber Volume Fraction* ..... V_f

---

*The matrix volume fraction is not included because it is not independent of the fiber volume fraction, i.e. $V_m = 1 - V_f$.

Young's Modulus of Fiber ..... E_f

Poisson's Ratio of Fiber ..... ν_f

Young's Modulus of Matrix ..... E_m

Poisson's Ratio of Matrix ..... ν_m

Fiber Orientation Angle ..... α

Width of Specimen ..... w

Thickness of Specimen ..... t

Tensile Load ..... F

One variable not present in the list is the aspect ratio of fiber diameter length to model width. The nature of the scattered light investigation between the fiber layers necessitated use of relatively short fibers. The model otherwise was fabricated geometrically similar to the prototype, thereby eliminating geometry as a variable.

Employing the Mass, Length, Time (M, L, T) unit system, the dimensional matrix is shown in Table 1

Table 1. Dimensional Matrix for Model Variables

	σ_{ij}	V_f	E_f	ν_f	E_m	ν_m	α	w	t	F
M	1	0	1	0	1	0	0	0	0	1
L	-1	0	-1	0	-1	0	0	1	1	1
T	-2	0	-2	0	-2	0	0	0	0	-2

The largest non-zero determinant that can be formed from the dimensional matrix is of second order, thus r equals two. There are ten variables therefore,

$$k - r = 8$$

A complete set of dimensionless products consists of eight π terms:

$$\pi_1 = \frac{\sigma_{ij}}{s}$$

$$\pi_2 = V_f$$

$$\pi_3 = \frac{E_f}{E_m}$$

$$\pi_4 = \nu_f \tag{14}$$

$$\pi_5 = \nu_m$$

$$\pi_6 = \alpha$$

$$\pi_7 = \frac{w}{t}$$

$$\pi_8 = \frac{s}{E_f}$$

where $s = \frac{F}{tw}$. According to Buckingham's theorem

$$\frac{\sigma_{ij}}{s} = f\,(\pi_2, \pi_3, \pi_4, \pi_5, \pi_6, \pi_7, \pi_8) \tag{15}$$

and if

$$\pi_{i_{Pr}} = \pi_{i_{Mo}} \qquad i = 2, 3, \ldots, 8 \tag{16}$$

then

$$\frac{\sigma_{ij_{Pr}}}{s_{Pr}} = \frac{\sigma_{ij_{Mo}}}{s_{Mo}}$$

Solving for $\sigma_{ij_{Pr}}$ yields:

$$\sigma_{ij_{Pr}} = \frac{s_{Pr}}{s_{Mo}} \sigma_{ij_{Mo}}$$

Equation (18) may be used to relate the stresses in the prototype to those in the model, provided equation (16) is satisfied. A comparison of the π terms for the two models and a typical glass-resin composite (prototype) is listed in Table 2 [57].

Table 2. Comparison of Dimensionless Products for Models and Prototype

	V_f	$\frac{E_f}{E_m}$	ν_f	ν_m	α	$\frac{w}{t}$	$\frac{s}{E_f}$
Two-Layer Model	.20	19.6	.20	.42	$\pm 45^o$	2.0	.000013
Four-Layer Model	.20	19.6	.20	.40	$\pm 45^o$	1.8	.000013
Prototype	.20-.60	20.0	.20	.42	$\pm 45^o$	1.5-10.0	.000013

From Table 2, it is clear that the two models will closely represent a prototype composite even though two π terms (V_f and $\frac{w}{t}$) are on the extremes of the prototype ranges. The value of the volume fraction V_f for the models was chosen so that the experimental data could be extracted accurately. The ratio $\frac{w}{t}$ is believed to have a relatively small effect on the stress distribution [58]. Selected stresses in the four-layer composite model with the same over all dimensions as the two-layer model, but with fibers one-half size, will be compared to the stresses found in the latter to evaluate the effects of boundary proximity, number of layers and fiber size relative to model size.

Model Fabrication

The complete models are shown in Figures 3 and 4. The dimensions and coordinate systems used for the two models are shown in Figures 2 and 5. The overall dimensions of the two models were approximately the same. Flint glass rods were selected for the fibers. A room temperature curing epoxy[59] was chosen for the matrix material in both the two-layered and four-layered models. This particular epoxy has very good photoelastic properties, a low percentage of shrinkage during curing, good machineability and elastic properties similar to many common resin systems. By carefully controlling the temperature of the epoxy during the cure cycle, the exothermic reaction rate was substantially reduced. This was necessary to minimize the thermally induced stresses which would result if bonding between the fibers and the matrix occurred at an elevated temperature. The difference in thermal expansion rates for the fibers and matrix was large enough to cause such stresses[59].

The room temperature epoxy consists of three main components. Two resins, ERL 2774* and ERL 2795, were mixed in proportions so that the desirable properties of each resin could be utilized. The catalyst ZZL 0803 was used for the purpose of slowing the reaction down; thereby reducing the exothermic reaction rate. The ratios of the components were two pbw ERL 2774, two pbw ERL 2795 and one pbw ZZL 0803. A silica gel, Cab-o-sil**, was added to the mixture to increase the clarity of the scattered light fringes; five milliliters per pound of mixture was found to

---

*The designations ERL 2774, ERL 2795 and ZZL 0803 are trade names of Union Carbide Corporation, New York, N. Y.

**Cab-o-sil is a trade name of the Cabot Corporation, Boston, Mass.

be optimum.

The two-layer model was fabricated first. The glass fibers were suspended in an aluminum mold. Fiber spacing and locations were maintained by the mold side plates. The inner surfaces of the mold were polished with a buffing wheel and Brasso*, then cleaned with acetone to remove any film left during polishing. These surfaces were then sprayed with Surfak** mold release which had proven earlier to be an exceptional release agent for epoxy. Immediately before the mold was assembled, the glass rods were cleaned with "metal conditioner" and "neutralizer" in that order. These chemicals are commonly used to prepare surfaces for application of electrical resistance strain gages, and practically the same procedure is used for applying strain gages to glass with an epoxy adhesive; therefore, the glass-resin bond was assumed to be sufficiently strong.

After assembling the mold with the fibers in place, all the joints were sealed with an RTV*** adhesive. During assembly, care was taken to keep the mold release off the fibers. The epoxy system was mixed for one hour; then the mixture was evacuated until the air, entrapped during mixing, had been removed. The mixture was poured in the mold carefully to avoid introduction of air bubbles in the model. After pouring, the epoxy was allowed to cure at room temperature ($75^{o}F$) for 96 hours. The

---

*Brasso is a liquid polish manufactured by R. T. French Co., Rochester, N. Y.

**Surfak is a trade name of Surfak Products, Chicago, Ill.

***Manufactured by General Electric Co.

model was then removed from the mold and post cured at 105°F for 96 hours. By making several simple glass-epoxy models, it was found that a post cure temperature significantly higher than 105°F caused measurable stresses near the fiber-matrix interface when cooled to room temperature. Even with the precautions mentioned, small residual stresses were observed, photoelastically, near the edges of the model at room temperature. The magnitudes of these stresses were negligible compared to the stresses induced by loading.

The design and construction of the four layered model was based on the same considerations which led to the use of the two layered configuration. The fiber volume fraction (V_f) was the same in each case so that the results could be compared. The four layered design included a more versatile mold, with the possibility of various fiber orientations, spacings and sizes. An unassembled view of the four-layer mold is shown in Figure 6. The process of assembly is pictured in Figures 7 through 9. Silicone rubber was used to form the interior sides and ends of the mold. The bottom surface of the mold was covered with a Teflon* sheet; therefore, no release agent was needed. Prior to assembly, the glass rods were cleaned in the same manner as previously described. The fiber lay-up in the four layered model was $+45^{\circ}$, -45°, -45°, $+45^{\circ}$ with reference to the longer sides of the model.

The casting and curing procedures used here provided the desired results, with respect to desired model dimensions, model transparency and residual stresses. Molded surfaces were extremely smooth and required no

---

*Teflon is a registered trade mark of the Du Pont Co.

polishing. The top surface of both models (the free surface during casting) was machined to remove any surface irregularities, and to obtain the desired dimensions. Two holes were reamed in each end of the models for the purpose of applying the tensile load.

Data Collection

For the purpose of taking data, the model under consideration was mounted in the scattered light polariscope on the support arm. This support arm, made of 2½ in. diameter steel pipe, was attached to a set of heavy duty, two directional, precision ways. The location of the model with respect to the light beam* could be easily and accurately (within 0.001 in.) determined from extended range dial indicators, providing unambiguous readings. Three rotational motions of the model were provided by the bracket which connected the load fixture to the support arm. Figure 10 shows the scattered light polariscope. The two-layer model is shown suspended in the immersion tank in Figure 11. The various angles were measured with an inclinometer. After the model was oriented in the desired configuration, the immersion tank was raised, so that the model was submerged in immersion fluid. Both models were loaded axially to 500 lb during the experiment. The immersion fluid used was a mixture of 50 parts of Arochlor** and 15 parts of light mineral oil. This mixture of immersion fluid was found, through testing, to be relatively inert with respect to the epoxy used here. A sample of the room temperature epoxy was left submerged for approximately six months with no apparent

---

*The light beam used in this polariscope is the output from a Helium-Neon laser; it has a fixed location and direction.

**Arochlor is a hydrocarbon manufactured by Monsanto Chemical Co.

physical or optical changes. The Arochlor oil (a hydrocarbon), however, does dissolve many common plastics, including the plastic faces on laboratory instruments. Additionally, extended periods of vapor inhalation or skin contact with the Arochlor oil was not recommended. These disadvantages mentioned did not appreciably hinder the data taking operations.

The indices of refraction of the model matrix and the immersion fluid were closely matched by the Arochlor-mineral oil mixture. In fact, the match was sufficient to give the models the appearance of layers of glass fibers suspended in the immersion fluid. The matching of the indices of refraction is necessary, so that the light beam will enter a skewed boundary of the model, and remain collinear with its original direction.

Scattered light data was collected in the regions of interest as indicated in Figures 2 and 5. The regions of interest were about 3.3 in. x 1.0 in. x 0.5 in. in the two layer model and 2.0 in. x 0.7 in. x 0.2 in. for the four layer model. Where possible, the light beam was transmitted in the three coordinate directions x, y and z at each point of interest. Points in the region were spaced at 0.100 in. intervals in a cubic grid pattern. Fringe locations (points of maximum and minimum light intensity) were recorded directly on graph paper by means of a photometric scanner[60]. Images of the fringe patterns were magnified and focused at a convenient plane with the aid of a camera mounted on an optical bench. The optical bench and immersion tank could be rotated as a unit about the light beam (vertical axis of the polariscope); thereby providing generous visual access. A photomultiplier tube (scanner tube) was situated at the plane of the focused fringe pattern image. By moving the scanner tube along

the fringe pattern, the variations in scattered light intensity were sensed by the scanner and converted to electrical signals. The electrical signals were amplified and used to drive the y displacement of an x-y recorder; the x displacement was controlled by the location of the scanner along the light beam. Figure 12 shows the photometric scanner. At some points, photographs of the fringe patterns were helpful in interpreting the data. The bulk of the data, however, was recorded using the previously mentioned scanner. The data recording system proved to be a reliable, accurate and, as importantly, an objective observer.

CHAPTER IV

SOLUTION METHODS

The solution methods for the two-layer and four layer models differed significantly. Solution in the two-layer model was for the full stress tensor (three normal stresses and three shear stresses in the interlaminar region between the fiber layers). To obtain all stresses required other than photoelastic information, specifically uses of the boundary conditions and the field equations of elasticity. In the four-layer model solution was obtained only for the interlaminar shear stress. This was found using only photoelastic data.

Two-Layer Model

The solution was obtained in the region ABCDA between the fiber layers as seen in Figure 2. A three dimensional network of solution stations was established in this region with a uniform station spacing of 0.1 in. The x,y,z co-ordinates identify the three directions used in the analysis and stress solution. The stresses obtained were then transformed to obtain values in a co-ordinate system (1,2,3) aligned with the model instead of with the fibers. Use of the region and first co-ordinate system aligned with the fibers provided good optical access for obtaining the scattered light data.

To determine the stresses: σ_x, σ_y, σ_z, τ_{xy}, τ_{xz}, τ_{yz}, the following sources of information were used: 1) photoelastic data, 2) boundary conditions, 3) stress-equilibrium relations. After obtaining

the photoelastic data in the three co-ordinate directions, full stress solutions were obtained with each plane normal to the z axis of the solution station network. Certain of the stress components could be obtained from photoelastic data alone. The remaining components were determined using a least-squares solution of a system of linear equations (Appendix A) obtained from the aforementioned information sources.

Photoelastic stress information at all stations may be given (Equations 19, 20, 21, 22)

$$(\sigma_y-\sigma_z)_{i,j,k} = \frac{1}{C}\left(\frac{dn}{dx}\right)_{i,j,k} (\cos 2\theta_x)_{i,j,k} \tag{19}$$

$$(\tau_{yz})_{i,j,k} = \frac{1}{2C}\left(\frac{dn}{dx}\right)_{i,j,k} (\sin 2\theta_x)_{i,j,k} \tag{20}$$

$$(\sigma_z-\sigma_x)_{i,j,k} = \frac{1}{C}\left(\frac{dn}{dy}\right)_{i,j,k} (\cos 2\theta_y)_{i,j,k} \tag{21}$$

$$(\tau_{xz})_{i,j,k} = \frac{1}{2C}\left(\frac{dn}{dy}\right)_{i,j,k} (\sin 2\theta_y)_{i,j,k} \tag{22}$$

where i, j and k denote station location in the y, x and z directions. These equations were used at all points in the region to determine the two shear stresses and the two normal stress differences without need of other information. The fringe derivatives were obtained using smoothed cubic splines (Appendix B) with extrapolated end regions identical to those described by Berghaus and Cannon for scattered light photoelasticity[61].

The third shear stress and one normal stress remained to be determined and thus yield the total stress tensor. To determine these values

a system of linear equations relating σ_x, σ_y and τ_{xy} was developed. Use of two normal stresses was necessary due to the inclusion of two stress-equilibrium equations in the solution. The system of equations over-determined the solution and provided opportunity for use of a weighted least-squares solution.

The system of equations may be developed in a manner similar to that used for two dimensional transmitted light photoelasticity[62].

Photoelastic information may be used at stations where the passage of the light beam in the z direction is not obstructed by a fiber. Thus:

$$(\sigma_x)_{i,j,k} - (\sigma_y)_{i,j,k} = \frac{1}{c}\left(\frac{dn}{dz}\right)_{i,j,k} (\cos 2\theta_z)_{i,j,k} \qquad (23)$$

$$(\tau_{xy})_{i,j,k} = \frac{1}{2c}\left(\frac{dn}{dz}\right)_{i,j,k} (\sin 2\theta_z)_{i,j,k} \qquad (24)$$

where i, j, and k indicate the appropriate location in the y, x, and z direction respectively of the solution station.

In addition at all points in the region σ_x and σ_y are related through the normal stress differences obtained from passage of the light beam in the x and y directions. Thus:

$$(\sigma_x)_{i,j,k} - (\sigma_y)_{i,j,k} = -(\sigma_z - \sigma_x)_{i,j,k} - (\sigma_y - \sigma_z)_{i,j,k} \qquad (25)$$

where $(\sigma_z - \sigma_x)_{i,j,k}$ and $(\sigma_y - \sigma_z)_{i,j,k}$ are obtained from Equations 21 and 19 respectively.

Stresses at the various stations may be related using the stress-equilibrium equations[63].

$$\frac{\partial \sigma_x}{\partial x} + \frac{\partial \tau_{xy}}{\partial y} + \frac{\partial \tau_{xz}}{\partial z} = 0 \tag{26}$$

$$\frac{\partial \tau_{xy}}{\partial x} + \frac{\partial \tau_y}{\partial y} + \frac{\partial \tau_{yz}}{\partial z} = 0 \tag{27}$$

These equations are commonly employed for two and three dimensional photoelastic analysis in the shear-difference method[53,54,64]. Finite difference approximations for equations (26) and (27) are used to proceed from the region boundary into the region in a sequential manner. For the present solution method the finite difference approximations are linear equations used together with equations from the other sources of information to obtain a solution for the stresses using least-squares. The finite difference approximations may be obtained using the mean value theorem as has been done previously[62]. For a point $(i + \frac{1}{2},j,k)$, midway between stations (i,j,k) and $(i + 1,j,k)$, if the station spacing is not great

$$\left(\frac{\partial \sigma_y}{\partial y}\right)_{i + \frac{1}{2},j,k} \approx \frac{1}{y_{i+1,j,k} - y_{i,j,k}} \left[(\sigma_y)_{i+1,j,k} - (\sigma_y)_{i,j,k}\right] \tag{28}$$

Furthermore, if the station spacing is not great

$$\left(\frac{\partial \tau_{xy}}{\partial x}\right)_{i + \frac{1}{2},j,k} \approx \frac{1}{2}\left[\left(\frac{\partial \tau_{xy}}{\partial x}\right)_{i+1,j,k} + \left(\frac{\partial \tau_{xy}}{\partial x}\right)_{i,j,k}\right] \tag{29}$$

and

$$\left(\frac{\partial \tau_{yz}}{\partial z}\right)_{i + \frac{1}{2},j,k} \approx \frac{1}{2}\left[\left(\frac{\partial \tau_{yz}}{\partial z}\right)_{i+1,j,k} + \left(\frac{\partial \tau_{yz}}{\partial z}\right)_{i,j,k}\right] \tag{30}$$

For equation (29)

$$\left(\frac{\partial \tau_{xy}}{\partial x}\right)_{i+1,j,k} = \frac{1}{x_{i+1,j+1,k} - x_{i+1,j,k}} \left[(\tau_{xy})_{i+1,j+1,k} - (\tau_{xy})_{i+1,j,k}\right]$$

Similar expressions may be obtained for all partial derivatives in equations (29) and (30). Recognizing that all displacement differences are equal due to the uniform station spacing equation (27) may be rewritten

$$(\sigma_y)_{i+1,j,k} - (\sigma_y)_{i,j,k} + \frac{1}{4}\left[(\tau_{xy})_{i+1,j,k} - (\tau_{xy})_{i-1,j,k} + (\tau_{xy})_{i+1,j+1,k} - (\tau_{xy})_{i-1,j+1,k}\right] = \frac{1}{4}\left[(\tau_{yz})_{i,j,k-1} - (\tau_{yz})_{i,j,k+1} + (\tau_{yz})_{i+1,j,k-1} - (\tau_{yz})_{i+1,j,k+1}\right] \quad (31)$$

In a similar manner, equation (26) may be approximated:

$$(\tau_{xy})_{i+1,j,k} - (\tau_{xy})_{i,j,k} + \frac{1}{4}\left[(\sigma_x)_{i+1,j,k} - (\sigma_x)_{i-1,j,k} + (\sigma_x)_{i+1,j+1,k} - (\sigma_x)_{i-1,j+1,k}\right] = \frac{1}{4}\left[(\tau_{xz})_{i,j,k-1} - (\tau_{xz})_{i,j,k+1} + (\tau_{xz})_{i+1,j,k-1} - (\tau_{xz})_{i+1,j,k+1}\right] \quad (32)$$

In equations (31) and (32) all terms on the left side are unknowns, those on the right are obtained from equations (7) and (9).

For solution stations on the free boundary of the region if θ is the angle between the x axis and the normal to the boundary, the stress transformation equations[65] yield

$$(\sigma_x)_{i,j,k} \cos^2(\theta)_{i,j,k} + (\sigma_y)_{i,j,k} \sin^2(\theta)_{i,j,k}$$

$$+ 2 (\tau_{xy})_{i,j,k} \cos(\theta)_{i,j,k} \sin(\theta)_{i,j,k} = \sigma_n \tag{33}$$

for the normal stress, and

$$\left[(\sigma_x)_{i,j,k} - (\sigma_y)_{i,j,k}\right] \cos(\theta)_{i,j,k} \sin(\theta)_{i,j,k}$$

$$+ (\tau_{xy})_{i,j,k} \left[\sin^2(\theta)_{i,j,k} - \cos^2(\theta)_{i,j,k}\right] = \tau_{nt} \tag{34}$$

for the surface shear stress in the xy (and nt) plane. For all boundary stations $\theta = -45^{\circ}$, $\sigma_n = 0$, $\tau_{nt} = 0$. Thus equation (15) becomes

$$\frac{1}{2} (\sigma_x)_{i,j,k} + \frac{1}{2} (\sigma_y)_{i,j,k} - (\tau_{xy})_{i,j,k} = 0 \tag{33a}$$

and equation (16) becomes

$$(\sigma_x)_{i,j,k} - (\sigma_y)_{i,j,k} = 0 \tag{34a}$$

Having a matrix of equations for the stresses in the region, the solution may proceed using least-squares. For the region in this problem, there were too many unknowns and equations to solve for the entire region at one time using the available computer. Therefore the region was broken up into subregions (Figure 13). Stresses were computed in the first subregion containing the free boundary. The solution then proceeded to each of the other subregions in a sequential manner. The stresses along the network line shared by two adjacent subregions were

obtained from the solution for one subregion and then used as boundary conditions for the solution of the next subregion. A list of the number of unknowns and equations for each region is given in Table 3.

Table 3. Numbers of Unknowns and Equations for Subregions of Two-Layer Model

Region	Unknowns	Equations
1	108	156
2	114	199
3	132	203
4	132	203
5	132	233
6	132	213
7	132	193
8	132	223
9	132	223
10	99	149

Stresses obtained from the solution in a given subregion were used in the solution for the succeeding subregion in an additional way. Because the fiber layers contained fibers at closely controlled, uniformly spaced intervals, and because the model was in a state of uniform uniaxial tension (away from the load application pins), the stress component values were considered to repeat themselves periodically along the model, with the length of the period equal to the fiber separation (along the length of the model). Because the solution region and subregions were placed symmetrically across a fiber in the x direction, stresses along the left edge (line AB) from one subregion could be used

as boundary condition values at appropriate stations along the right edge (line CD) in the stress solution for a succeeding subregion.

Certain of the equations were weighted[62]. Because the value of $(\sigma_x)_{i,j,k} - (\sigma_y)_{i,j,k}$ in equation (25) is obtained using the difference of two derivatives, it was considered to be much less accurate than the difference obtained from equation (4). Equation (25) was given a weight of one tenth (0.1) at each solution station.

Following solution for stresses in all subregions, the values were then transformed from the x,y,z co-ordinate system to the 1,2,3 co-ordinate system. The transformation equations for each station become (without station subscripts):

$$\sigma_1 = \frac{1}{2}(\sigma_x + \sigma_y) + \tau_{xy} \tag{35}$$

$$\sigma_2 + \frac{1}{2}(\sigma_x + \sigma_y) - \tau_{xy} \tag{36}$$

$$\sigma_3 = \sigma_z \tag{37}$$

$$\tau_{12} = \frac{1}{2}(\sigma_y - \sigma_x) \tag{38}$$

$$\tau_{23} = \frac{1}{\sqrt{2}}(\tau_{yz} - \tau_{xz}) \tag{39}$$

$$\tau_{13} = \frac{1}{\sqrt{2}}(\tau_{yz} + \tau_{xz}) \tag{40}$$

So that comparisons could be made more easily, stresses in the rectangular region ALNDA of Figure 13 were desired. It was noticed that the triangular area DFED was equivalent to region AKFA, and that area FGHEF was the same as area KMNFK. The triangular area KLMK was

made up of two smaller triangles, GBHG and HCEH. Signs of the shear stress components τ_{23} and τ_{13} were changed in the region GBHG to account for relocation of this area. In addition to this relocation, the transformed stresses were normalized with respect to the average tensile stress applied to the model. The transformed, normalized stresses are plotted for the region ALNDA in Figures 14 through 53. An explanation for the various items in the figures is found preceding Figure 14.

Four-Layer Model

The four-layer model was constructed to study directly the interlaminar shear stress in the matrix between two fiber layers and to compare results with the two layer model. The two outer layers were normal to the two inner layers, to produce a symmetric model.

Analysis was performed between two crossed fiber layers. Data was taken by passing the light beam between the layers, parallel to them and normal to the side of the model (Figure 4). Thus for passage of the light beam in the x direction:

$$\tau_{yz} = \frac{1}{2c} \frac{dn}{dx} \sin 2\theta_x$$

In this equation, n is again the fringe order and θ_x is direction with respect to the horizontal (z axis) of greatest principal stress. The x,y,z coordinate system is completely different for this problem.

Data was recorded photographically because the distortions present when viewing the trace through the first layer of fibers could not be reliably observed with the scanner and plotter. Three exposures were made side by side on a single film plate by rotating the observation

camera of the scanner to three different view directions (45^{o} between directions). This provided opportunity to view all positions of the trace in at least one view without observing through the fibers (Figure 54). Fringe locations were measured using a scale. Secondary principal directions were determined by observing maximum or minimum fringe definition.

The fringe derivatives were calculated again using a smoothed cubic spline. Because the derivative fluctuations were pronounced near the boundary on most traces, the second derivative term for the extrapolation parabola was determined from a least square parabola fitted to the five data points immediately adjacent to the boundary[61]. Continuous curves for the secondary principal directions were obtained using least-squares cubic polynomials. Thus the cubic spline and the cubic polynomial provide continuous curves of τ_{yz} over the length of the trace. The results are shown in Figures 55-69. An explanation of the various items in the figures is found preceding Figure 55.

CHAPTER V

DISCUSSION OF RESULTS

The results for both models yield much higher matrix stresses than theoretically determined composite stresses. When these high values were obtained, the stress-optical constant of the epoxy and the load calibration factor of the load frame were checked and found to be very close to their original values. The steps in the solution method were checked and no inconsistencies were found. Therefore, these were not considered to be sources of error.

The specific results for the two models are discussed separately.

In the two-layer model the results for all six components show no strong tendency for a monotonic variation from model edge to center. Where fibers in the two layers intersect the 1-3 plane at the same place, the normal stresses and the shear stress, τ_{12}, often vary erratically. This may be due to the proximity of the two fibers, but is probably also due to the lack of data from a light beam in the 3 direction at these locations. The inability to pass a light beam in the 3 direction where two fibers lie in the path prevents use of equations (23) and (24) at solution stations in these locations. This does not affect values of τ_{13} and τ_{23} whose values are determined from photoelastic data alone and not from the least squares solution.

The results for the two-layer model are given at solution stations only in all figures. The line segments connecting the values aid in distinguishing the various stress components but are not intended for inter-

polation.

Results for the four-layer model show a ripple effect superposed on a rather linear decrease of the interlaminar shear stress, τ_{yz}, from the edge to the center of the model. Such decrease is predicted theoretically for composite interlaminar stress although the rapid decrease (nonlinear) adjacent to the edge is not present in the four-layer model. A comparison of the matrix interlaminar shear stress magnitudes with composite interlaminar shear stress obtained by theoretical methods indicates experimental matrix stresses are one order of magnitude higher in the edge region. The theoretical stresses may be obtained from the results of Pipes and Pagano using the appropriate stress-strain and transformation relationships[7,13].

The ripple effect has the same period as the fiber spacing in the xy plane. This effect produces a relatively low magnitude shear stress as the light beam passes close to a fiber in the upper layer. A relatively high magnitude shear stress is produced when the light beam passes between fibers in the upper layer. The magnitude of ripple fluctuations is generally greater when the light beam is transmitted along a section (xy) plane where the fibers of both layers intersect this xy plane at the same location.

Relatively high stresses tend to be near the edge when the fiber intersects the xy plane near but inside the free boundary.

There does not appear to be a significant difference in values from the three solution planes.

CHAPTER VI

CONCLUSIONS

The results of this investigation provide an experimental solution to the problem of determining interlaminar stresses in the matrix of a multilayered fibrous composite. The use of dimensional analysis permits the implications of the results obtained from these photoelastic models to be extended to prototype fibrous composites which are similar. Insofar as comparisons are possible, the results of the two-layer and four-layer models show good agreement. The generally higher values of the interlaminar shear stress in the four-layer model may be due to smaller aspect ratio for this model. This factor may also account for the more pronounced linear decrease in shear stress magnitude from the edge to the center of the model. In view of the independence of the analyses the agreement of the results tends to give credibility to the methods employed.

Comparisons with similar experimental analyses verify the relatively high stress concentrations found here. In particular, the investigations performed by Azzi and Tsai[36] and Tsai[66] showed that little strengthening is provided by the fibers in tensile specimens with off-axis fibers. Azzi and Tsai used as one case unidirectional model whose fibers were oriented 45^{o} from the applied tensile load. The fracture strength of such a model was found to be less than the fracture strength of the matrix itself; thereby, indicating the existence of stress con-

centrations.

An average stress concentration of 1.5 was found by Tsai. The model tested was a three layered $\pm 45^{o}$ fiber orientation, glass-resin, fibrous composite. The average stress concentration factor of 1.5 could be due to relatively high stresses in the interlaminar region as indicated here.

Daniel[67] found a stress concentration factor of about 2.0 in a composite tensile model whose fibers were normal to the direction of the applied tensile load.

Comparisons of the results with the relevant theoretical analyses are not as good. The tendency toward very high shear stresses adjacent to the specimen edges predicted by Pipes and Pagano[7] was not evidenced uniformly in these results (see stress τ_{13}). This tendency was more apparent in the four-layer model; possibly due to the larger width-to-fiber diameter ratio. In any case, the "edge effect"[7] did not seem to dominate the shear stress distributions. There was a general trend in most of the σ_1 and τ_{12} curves (two-layer model) to decrease near the outer boundary as discussed by Pipes and Pagano[7]. However, the fluctuations in the stresses away from the boundary observed in the experiments were not predicted theoretically. The frequency of these variations were found to be approximately in phase with the fiber locations. The theoretical analyses assume homogeneity.

With respect to the normal stress σ_1 (parallel to the applied tensile force) in the two-layer model, an average stress concentration factor of approximately 3.4 was found in the interlaminar region of the two-layer model. While this seems excessive at first glance, it accounts

for only 51% (Appendix C) of the applied load. This means the stress σ_1 would have to be relatively low over the rest of the model. The stress component σ_2 generally behaved as expected; i.e. σ_2 approached zero near the outer boundary of the model (Station 1).

The use of the least squares method to effect the complete solution in the two-layer model was the first such application in a three dimensional problem and justifies further use in this field.

The most significant result is the high value of the various matrix stresses, particularly the interlaminar shear stress. Insofar as matrix stresses are important factors in composite failure, the results of this report indicate that theoretical studies which assume homogeneous layers in composites do not yield correct values for them. High matrix strains have been predicted previously for certain types of fiber orientation and loading relations in unidirectional composites[68]. It has been shown that the matrix strains can be higher than the fiber strains by a factor of the order of the ratio of fiber modulus to matrix modulus[69]. These experiments show that such values can also be expected in crossply composites when loaded at 45° with respect to perpendicular crossply fibers. The results of this study should be of help in any refinement of the hypotheses concerning stress distribution in composites.

The computer techniques may be adapted to other problems through minor modifications. Photoelasticity is ideally suited to the use of the least squares approach in obtaining solutions. The use of finite difference approximations to the field equations of elasticity together with experimentally derived stress relationships (stress-optic law) usually provides the opportunity to structure an overdetermined set of

linear algebraic equations. The field of photoelasticity would benefit by utilizing the least squares technique as a standard solution method.

In addition to the potential contributions to the study of composites, this investigation also demonstrates the versatility of scattered-light photoelasticity. The particular polariscope[60] used here greatly simplified the data gathering procedure. The automatic fringe recording feature supplied accuracy virtually unattainable with the standard photographic fringe record.

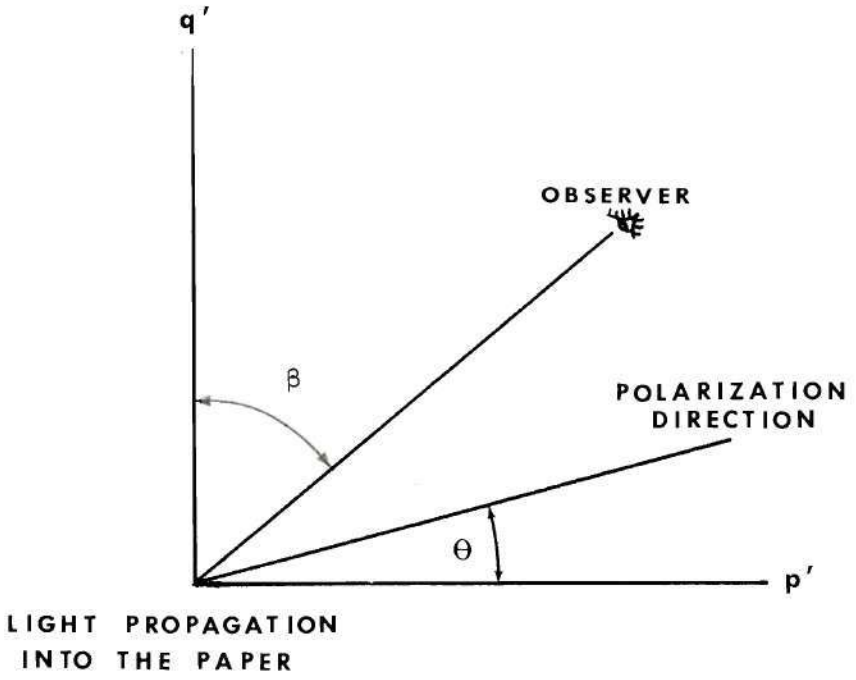

Figure 1. Optical directions and secondary principal stresses for scattered light photoelasticity.

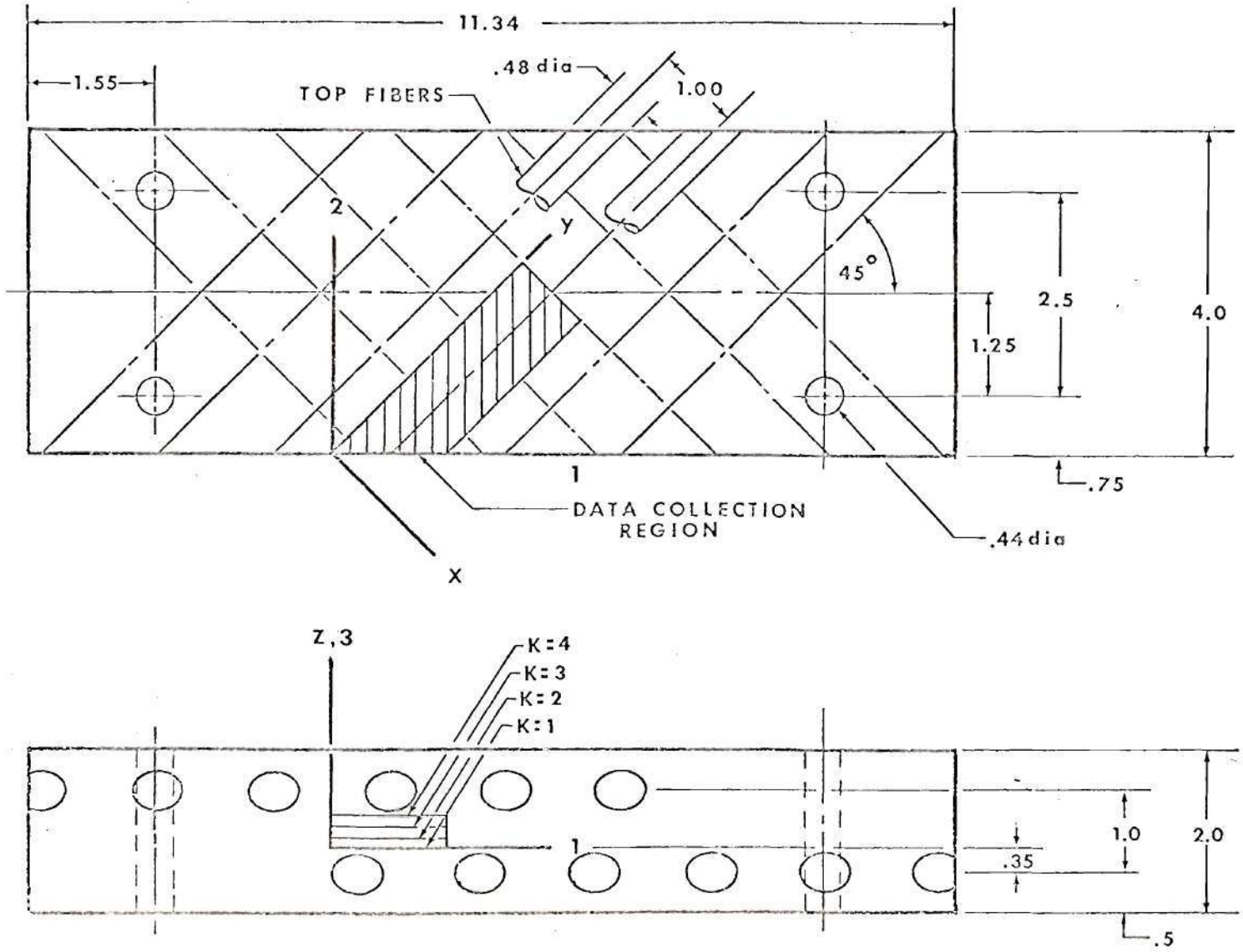

Figure 2. Configuration of two-layer model.

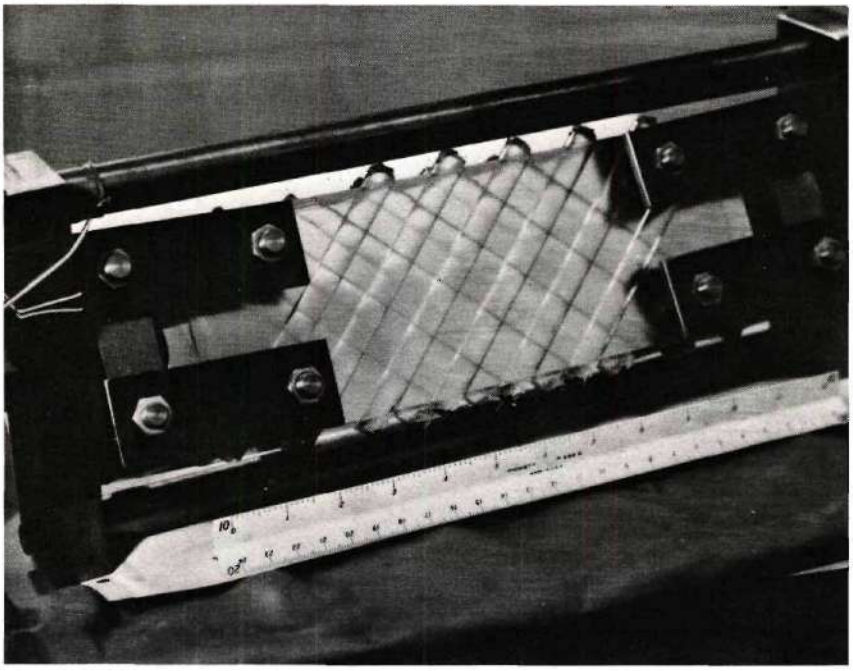

Figure 3. Two-layer photoelastic composite model in load frame.

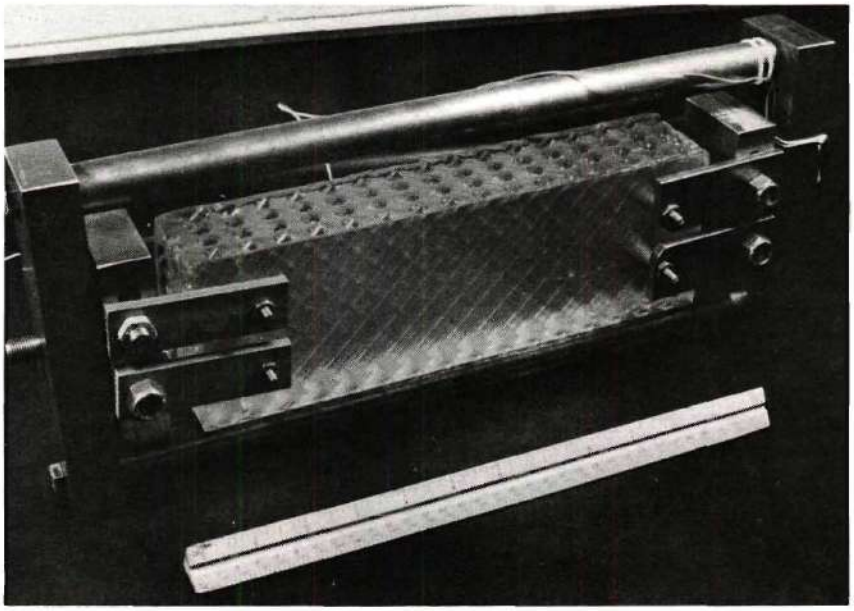

Figure 4. Four-layer model in load frame.

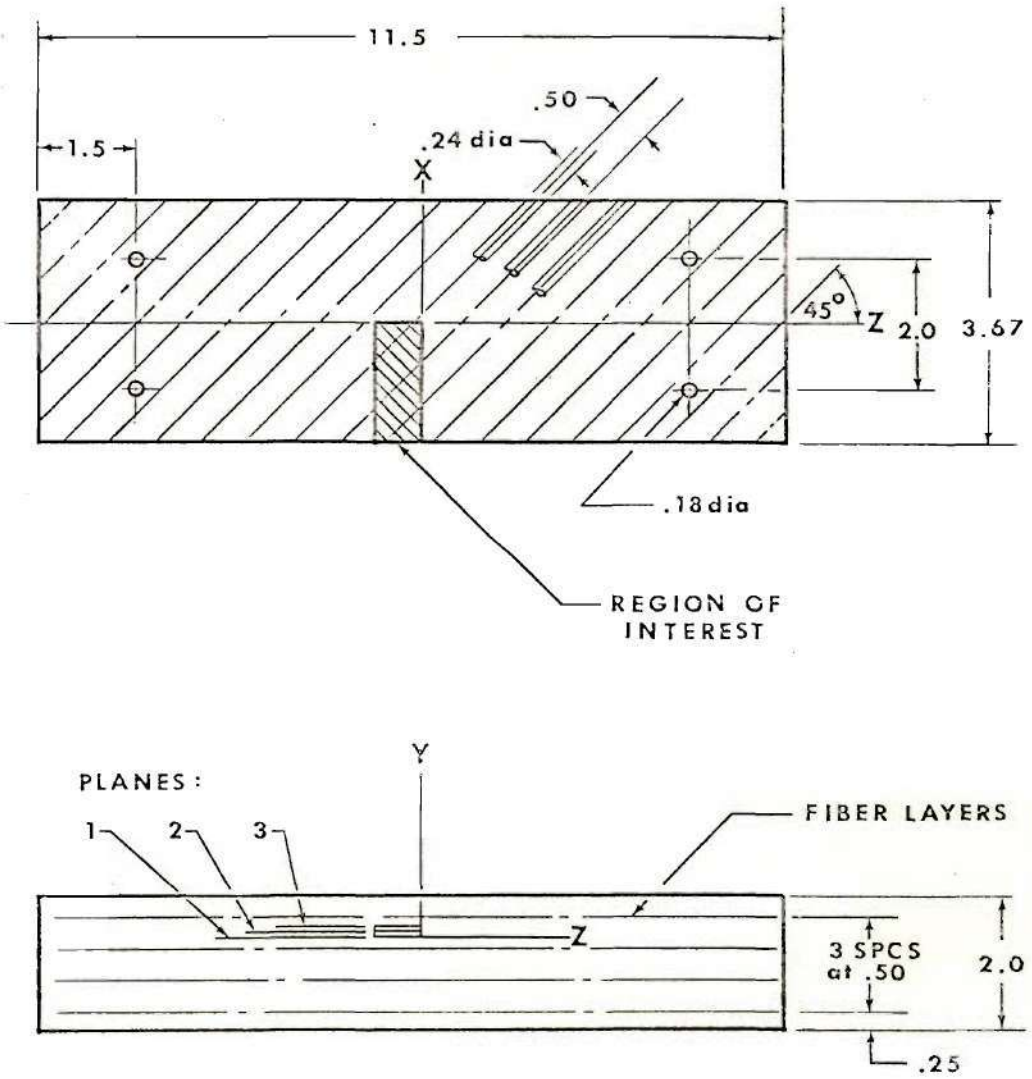

Figure 5. Configuration of four-layer model.

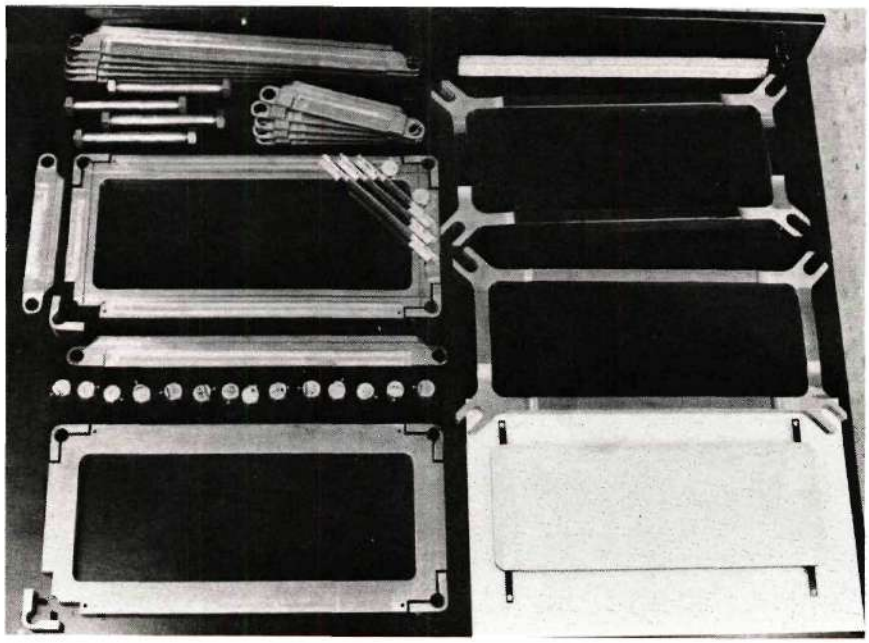

Figure 6. Unassembled mold for four-layer model.

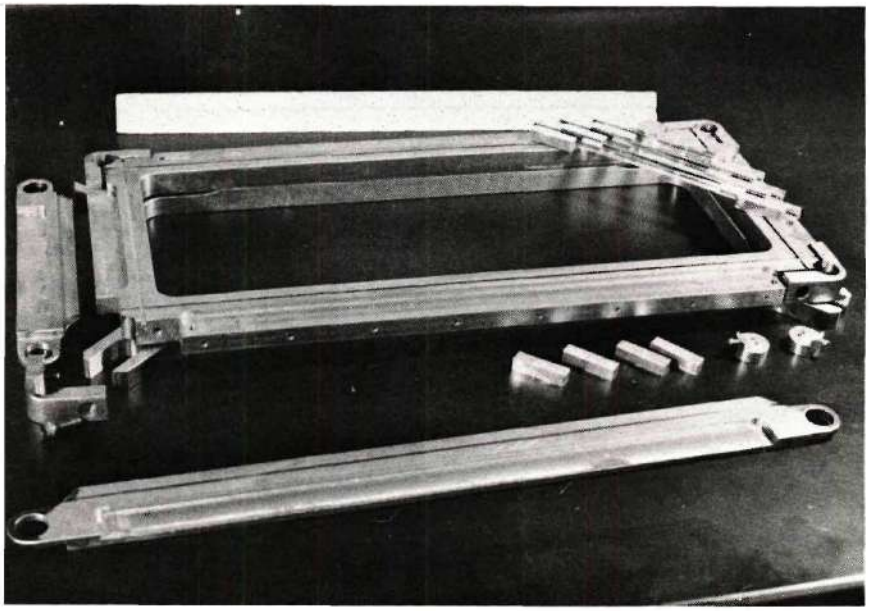

Figure 7. First fibers in place in mold.

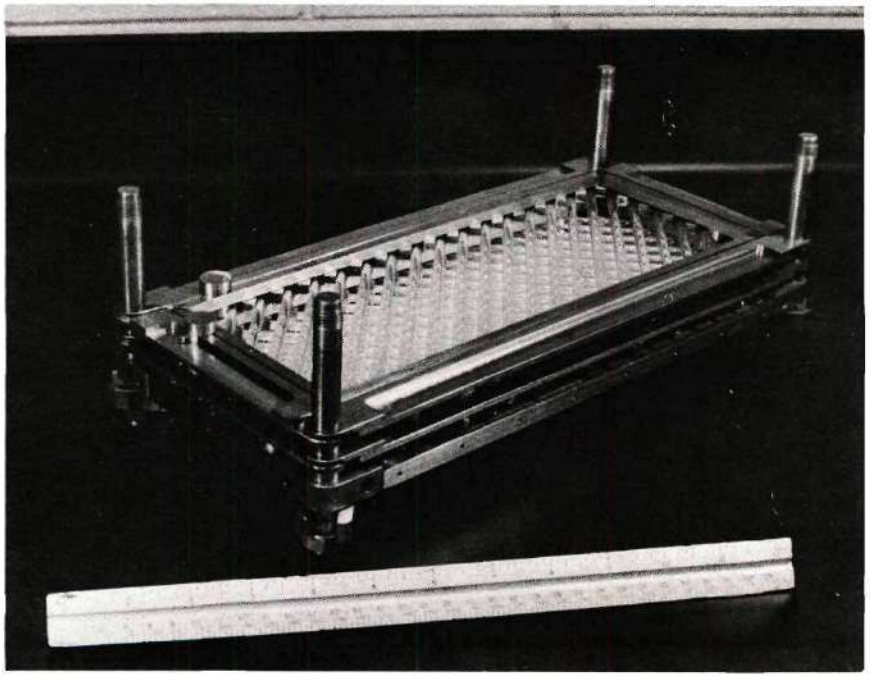

Figure 8. Two fiber layers in place in mold.

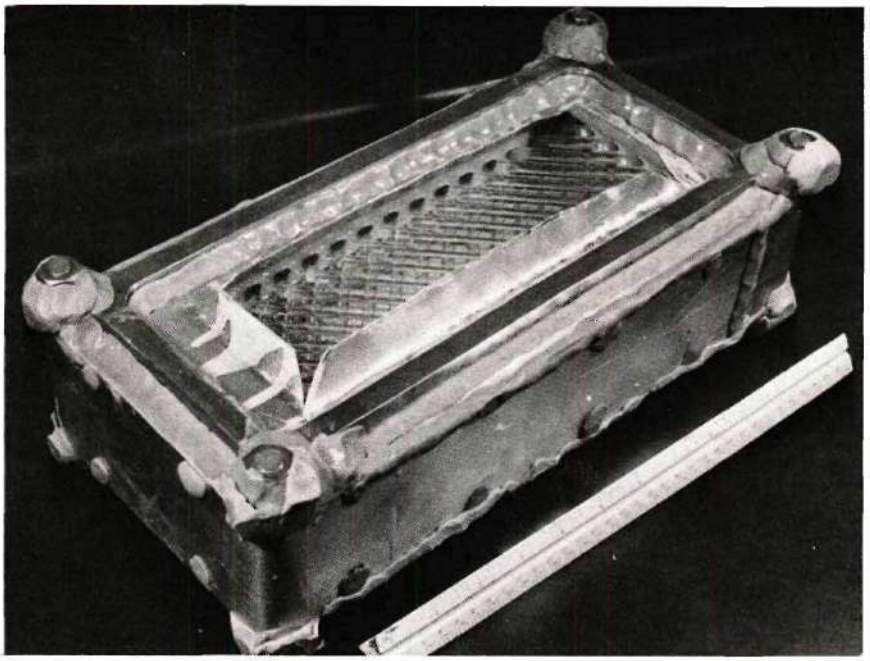

Figure 9. Completed mold with all fibers in place prior to addition of epoxy.

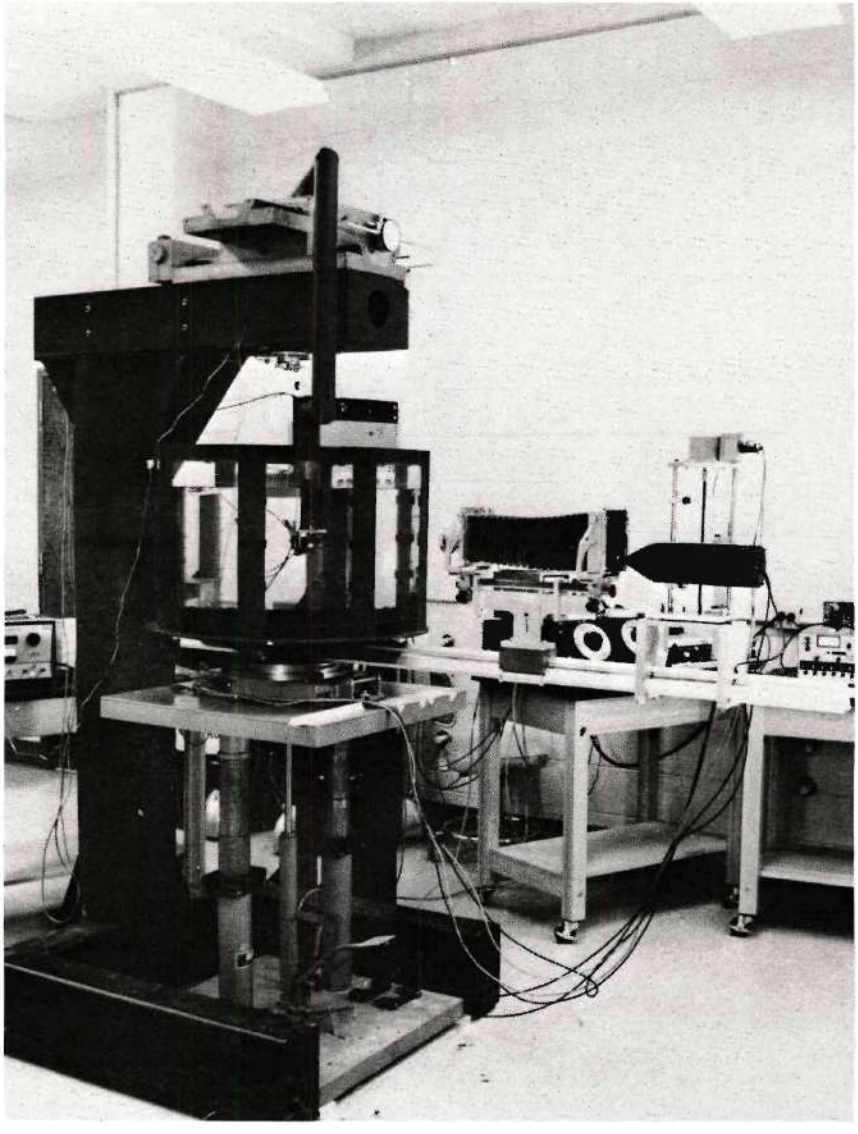

Figure 10. Scattered light polariscope

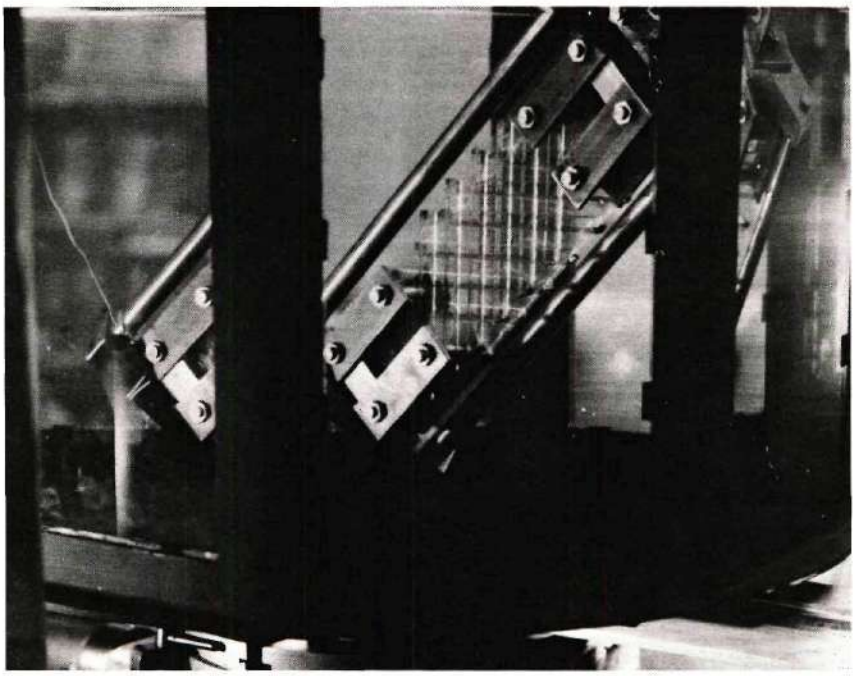

Figure 11. Two-layer model suspended in immersion tank.

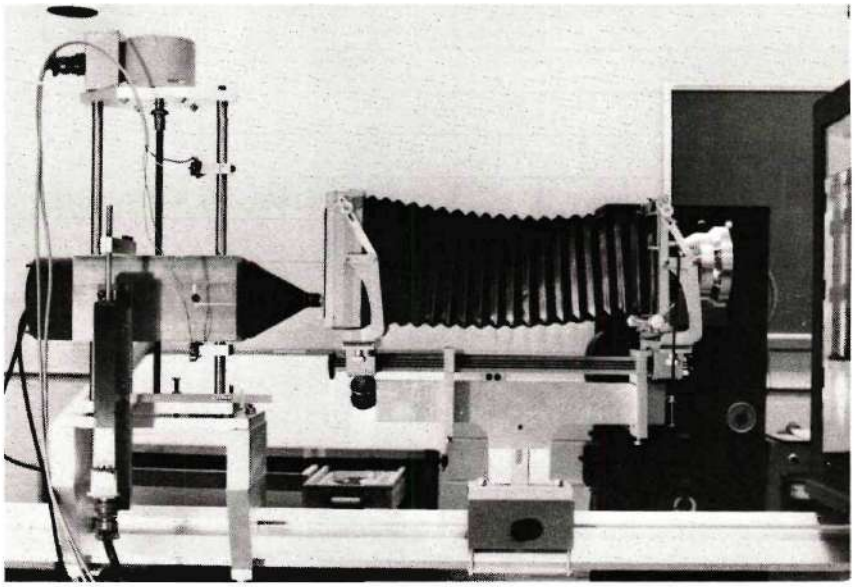

Figure 12. Photometric scanner

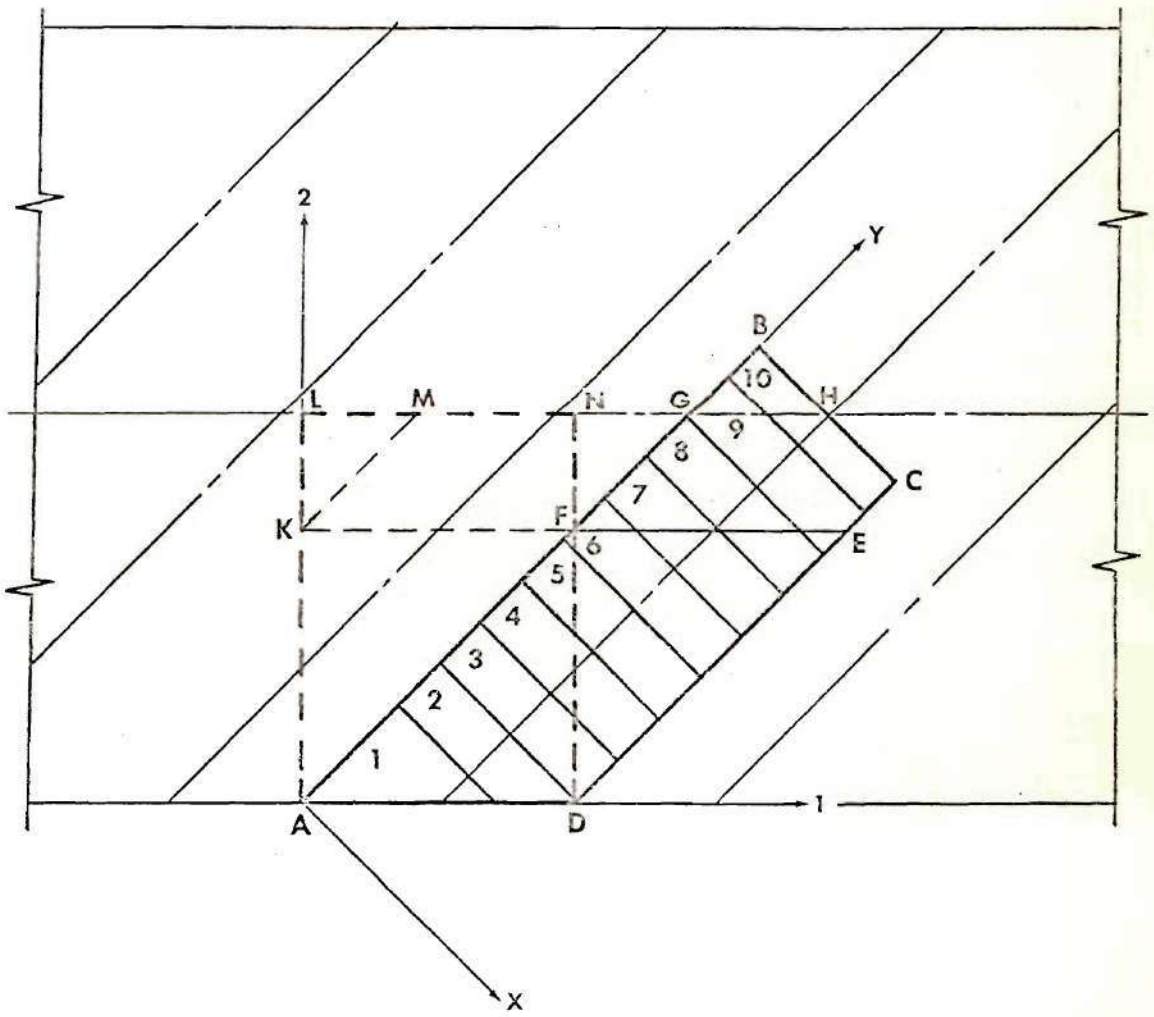

Figure 13. Solution region of two-layer model showing subregions and transformation axes.

Graphs of Stresses in Two-Layer Model

The graphs which follow (Figures 14-53) contain the stress distributions found in the matrix of the two-layer model. In each figure, the stresses in the upper set of curves represent the three normal stresses: σ_1, σ_2, and σ_3. The three curves in the lower half of the figure represent the three shear stresses: τ_{12}, τ_{23}, and τ_{13}. All stress values have been normalized by dividing each stress by the average normal stress, S, aligned with the model.

The ordinates of the graphs give the value of the normalized stress component. Values of the index I' (location of each solution station along the 2 axis) are given on the abscissa of the graphs. Stations proceed from adjacent to the free boundary (on the left) to the center of the model (on the right). In the 2 direction the stations are 0.14 in. apart. The location of each station is given uniquely by the three indices, I', J', and K. Thus, for each figure the indices J' and K are given in the caption. Stations along the 1 axis correspond to values of J'. Planes located by the four values of K are shown in Figure 2.

Fiber locations in the appropriate 2, 3 plane are indicated by the stars. Horizontal locations have the same scale value as the solution stations. Vertical fiber locations on the graphs are scaled closer than horizontal locations. To obtain a vertical scaled distance from the abscissa (which now represents the location, K, of the row of solution stations), the distance on the graph should be multiplied by 1.7. Figure 14 shows fiber cross sections at the fiber intersections. The cross section ellipses have the same scale (the horizontal scale) in the vertical and horizontal directions.

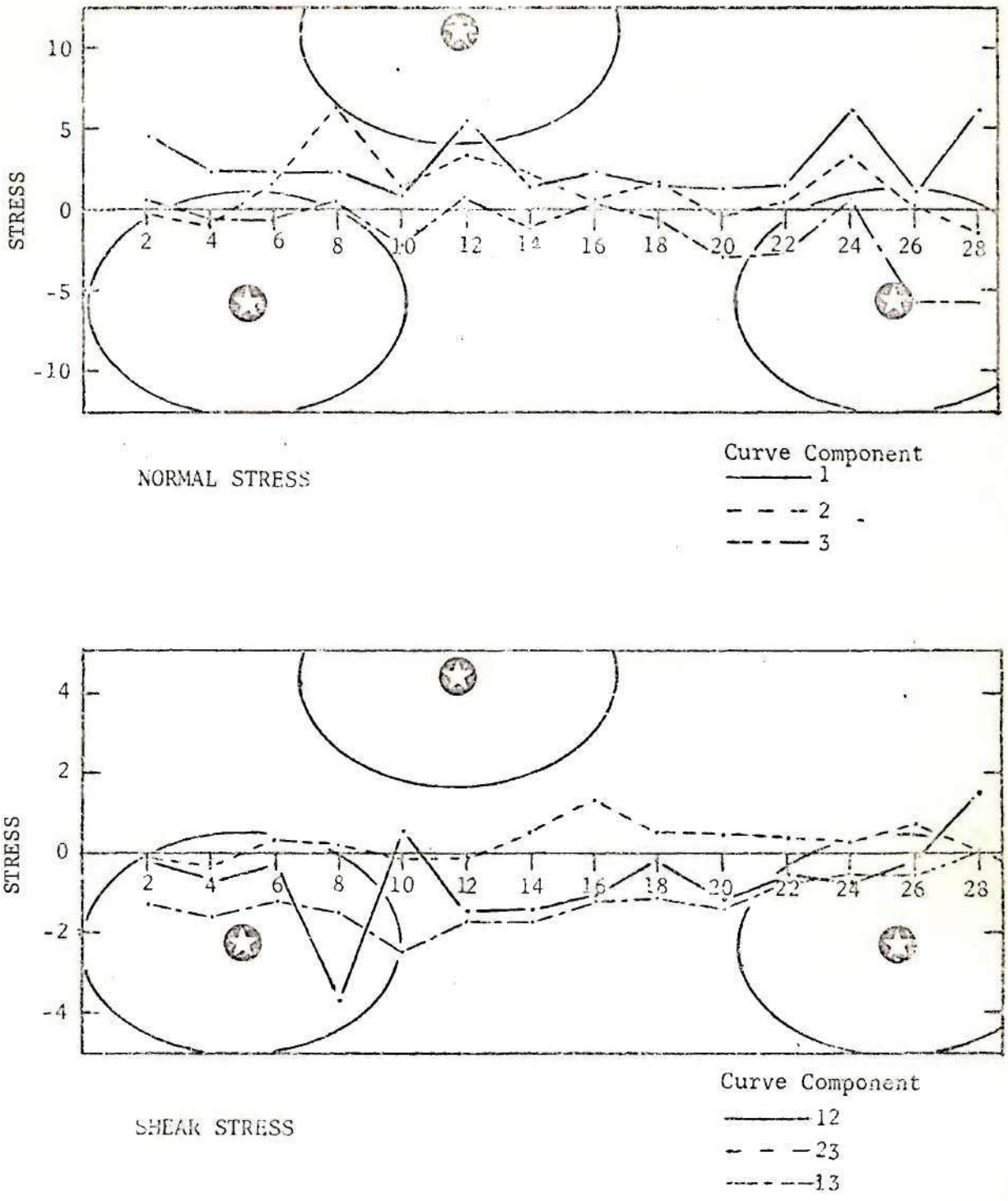

Figure 14. Normal and shear stress results for two-layer model for solution stations (I') in 2 direction for J' (1 direction) = 2, K = 1.

Refer to explanation preceding Fig. 14 and to Figs. 2 and 13.

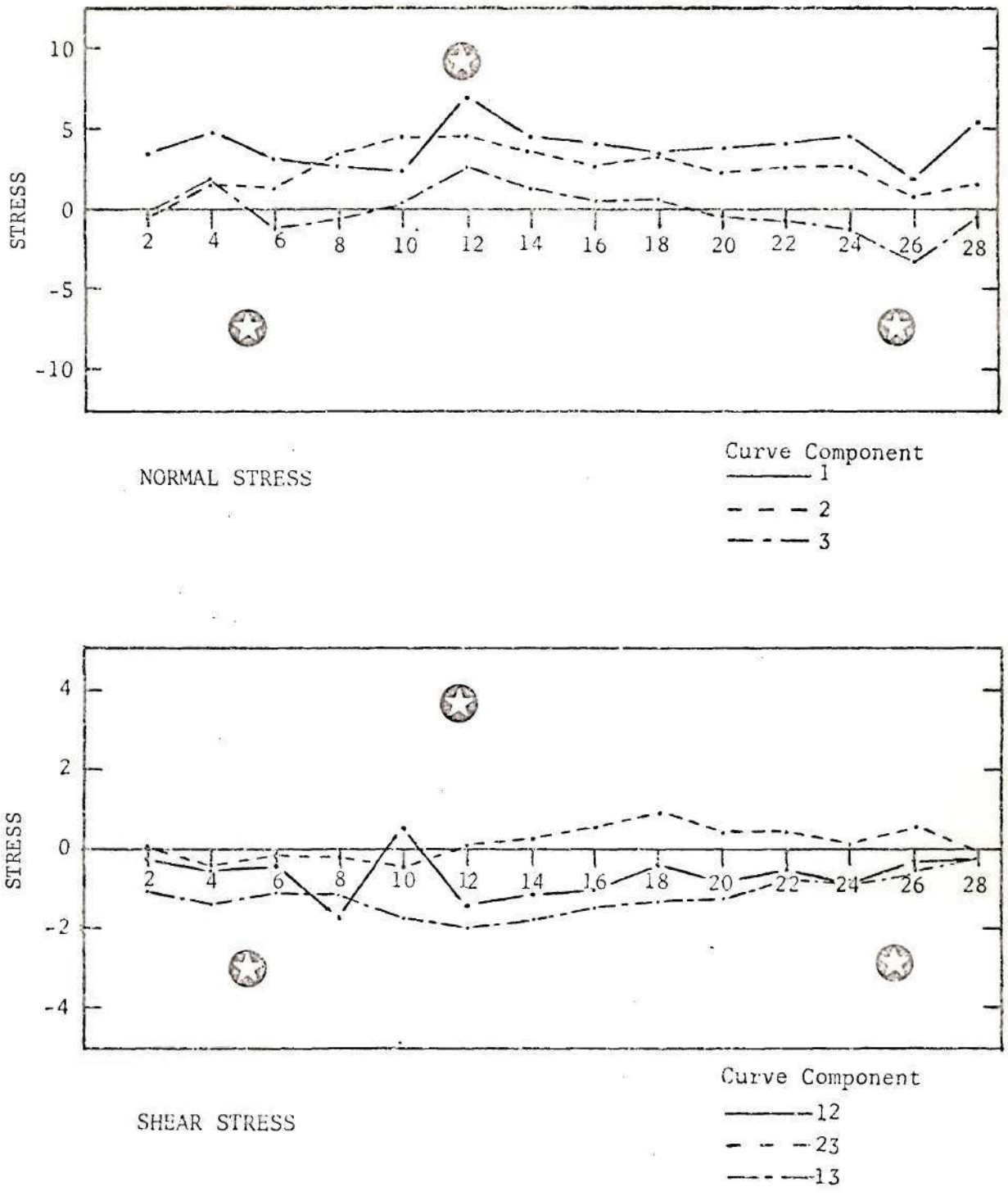

Figure 15. Normal and shear stress results for two-layer model for solution stations (I') in 2 direction for J' (1 direction) = 2, K = 2.

Refer to explanation preceding Fig. 14 and to Figs. 2 and 13.

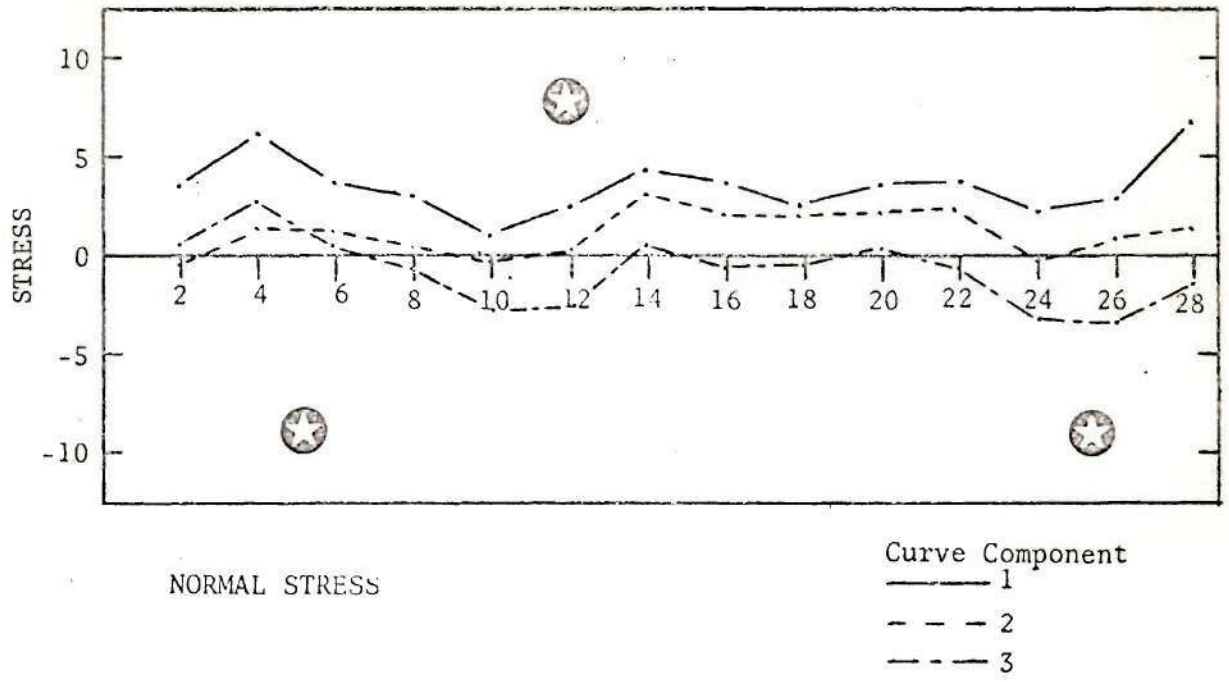

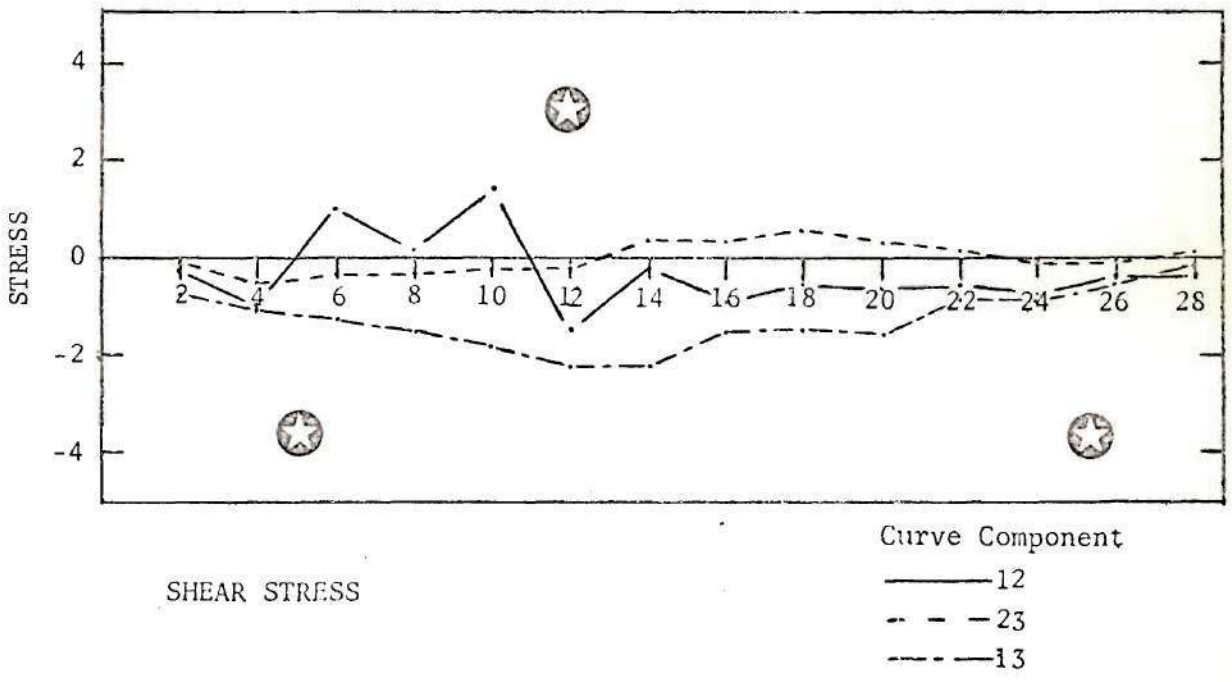

Figure 16. Normal and shear stress results for two-layer model for solution stations (I') in 2 direction for J' (1 direction) = 2, K = 3.

Refer to explanation preceding Fig. 14 and to Figs. 2 and 13.

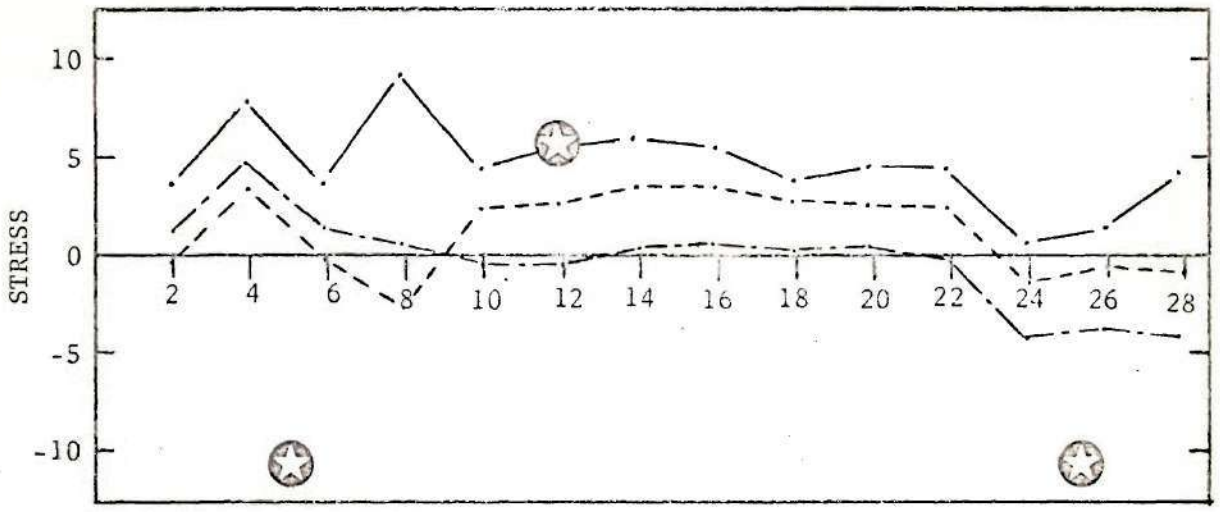

NORMAL STRESS

Curve Component
1
2
3

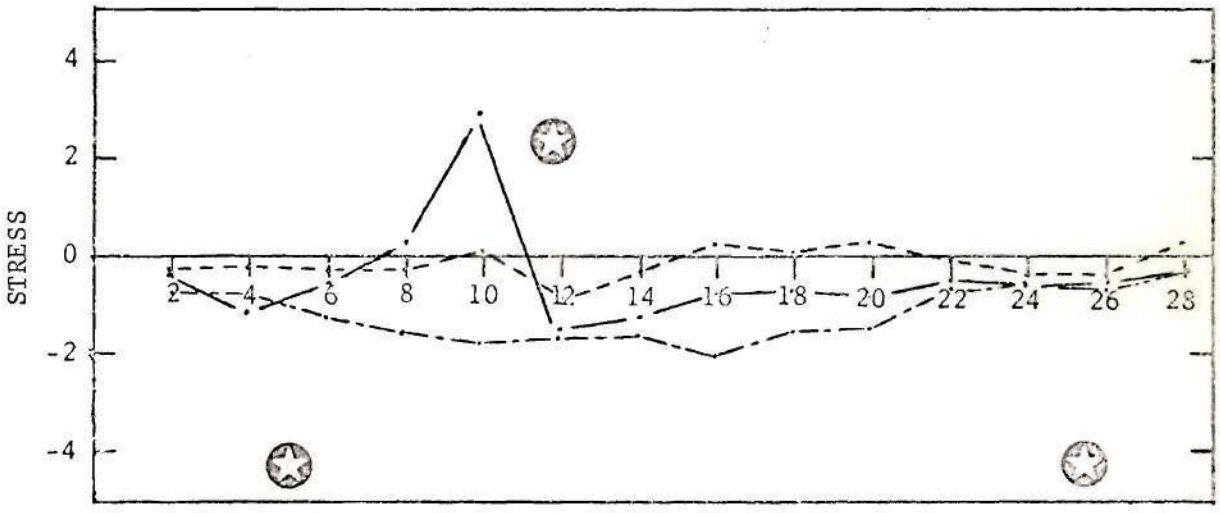

SHEAR STRESS

Curve Component
12
23
13

Figure 17. Normal and shear stress results for two-layer model for solution stations (I') in 2 direction for J' (1 direction) = 2, K = 4.

Refer to explanation preceding Fig. 14 and to Figs. 2 and 13.

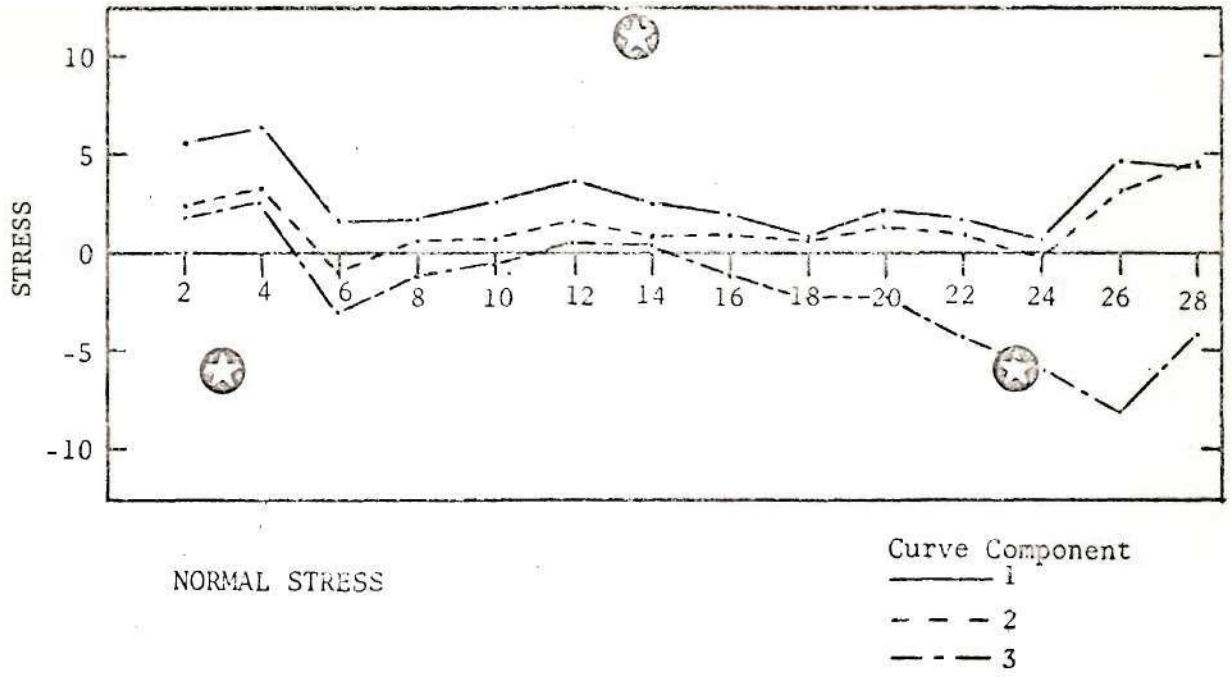

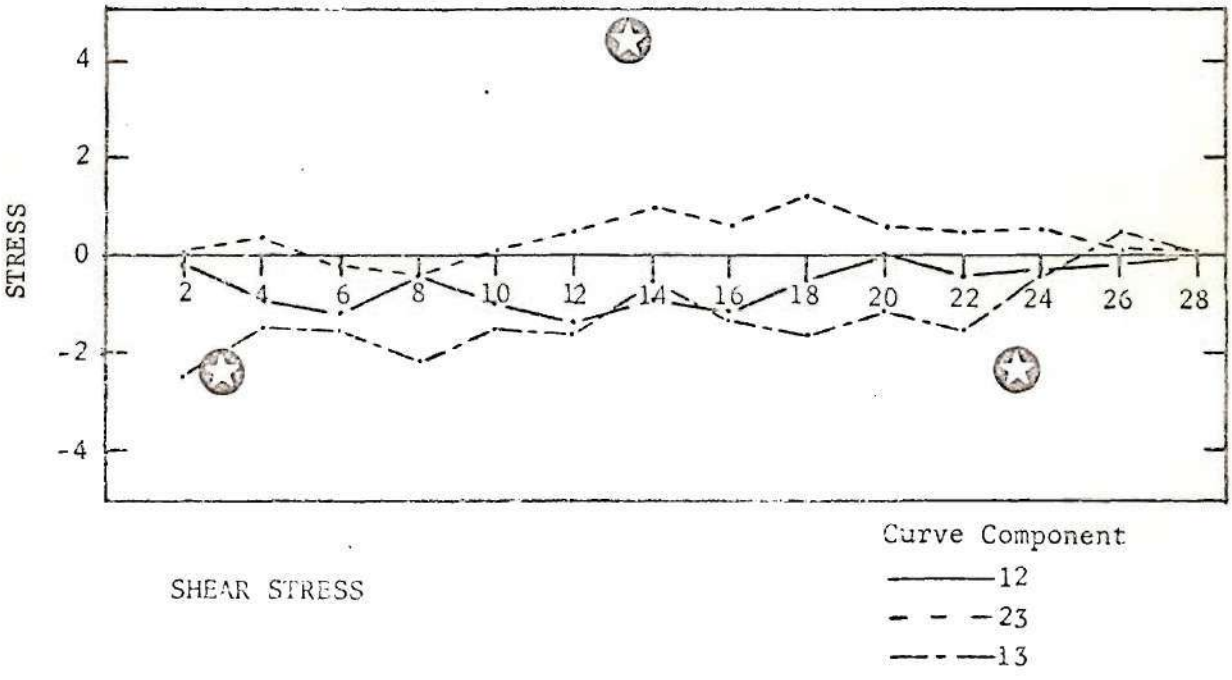

Figure 18. Normal and shear stress results for two-layer model for solution stations (I') in 2 direction for J' (1 direction) = 4, K = 1.

Refer to explanation preceding Fig. 14 and to Figs. 2 and 13.

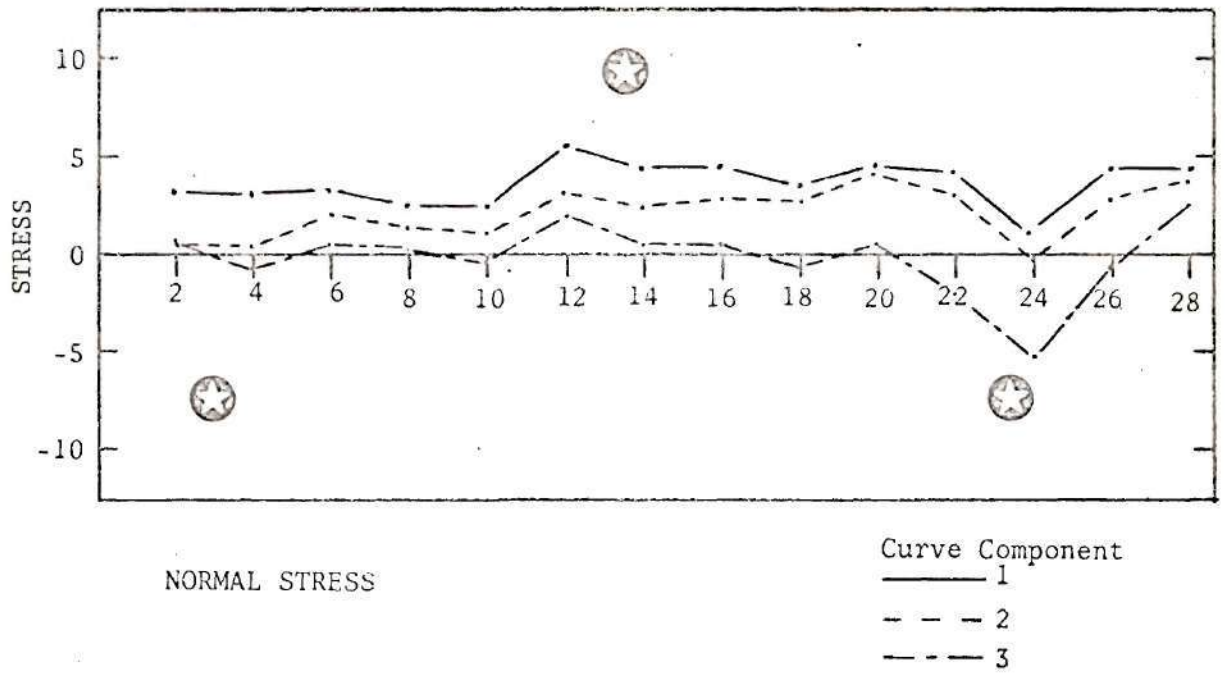

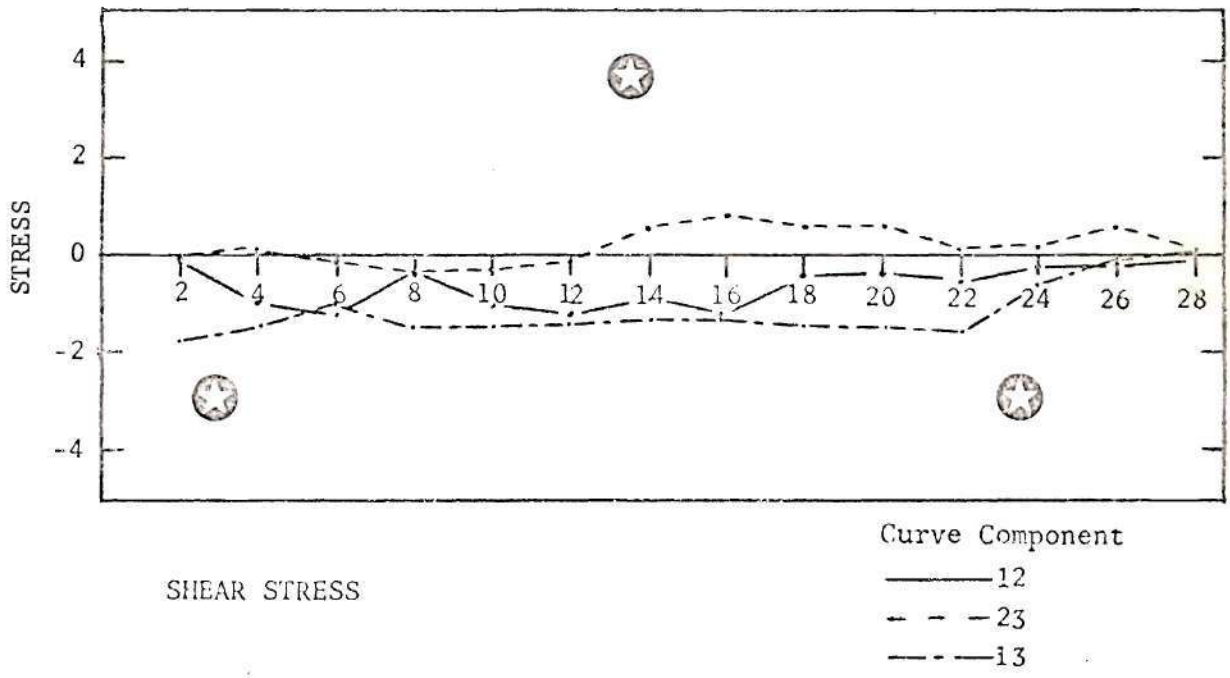

Figure 19. Normal and shear stress results for two-layer model for solution station (I') in 2 direction for J' (1 direction) = 4, K = 2.

Refer to explanation preceding Fig. 14 and to Figs. 2 and 13.

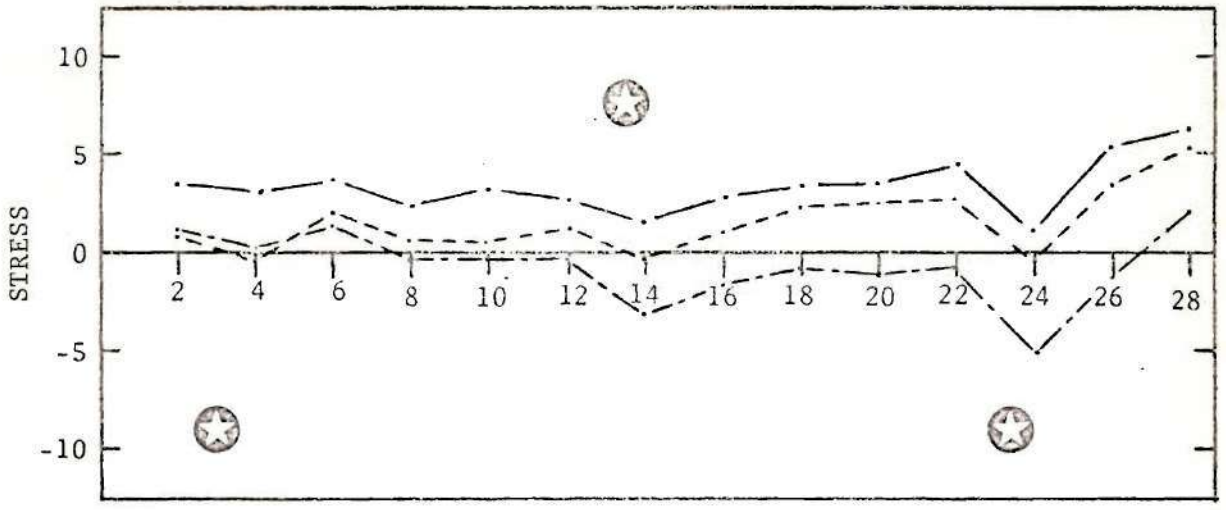

NORMAL STRESS

Curve Component
1
2
3

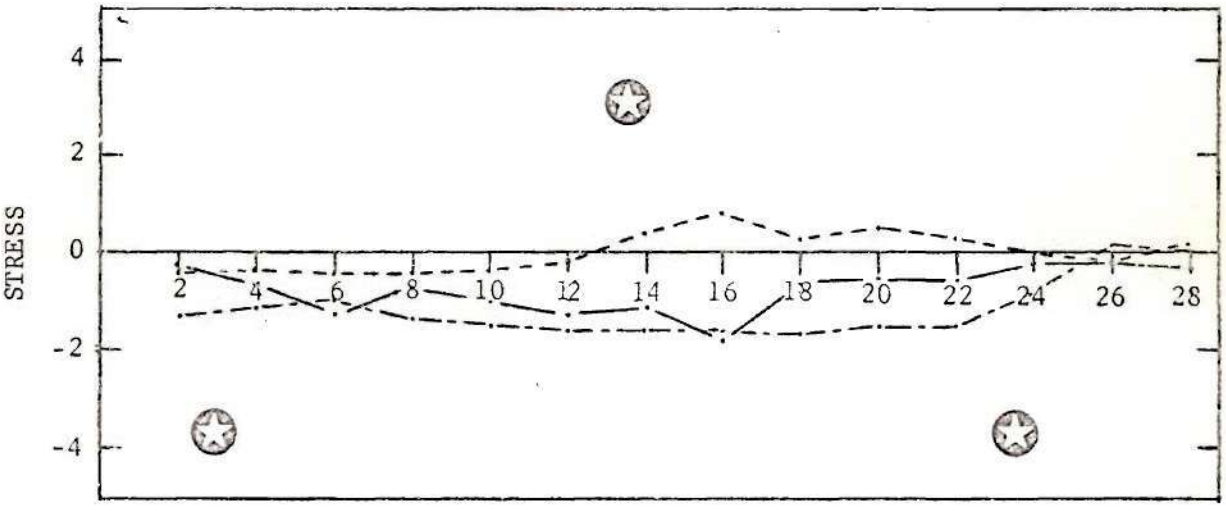

SHEAR STRESS

Curve Component
12
23
13

Figure 20. Normal and shear stress results for two-layer model for solution station (I') in 2 direction for J' (1 direction) = 4, K = 3.

Refer to explanation preceding Fig. 14 and to Figs. 2 and 13.

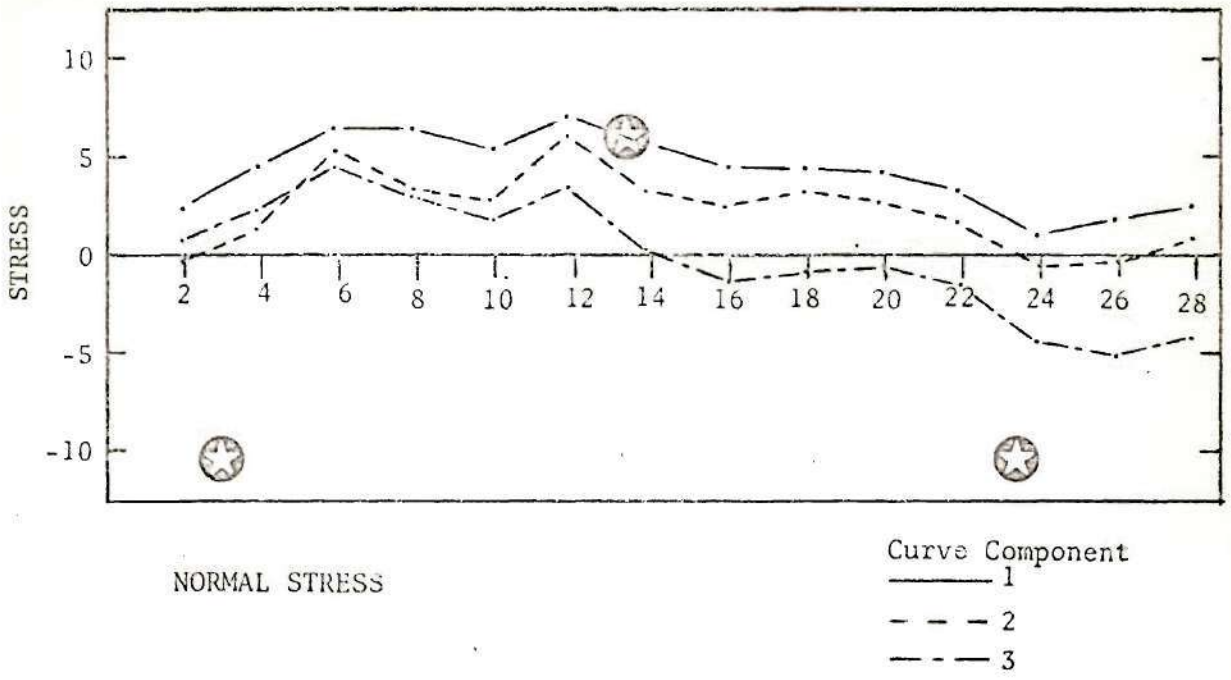

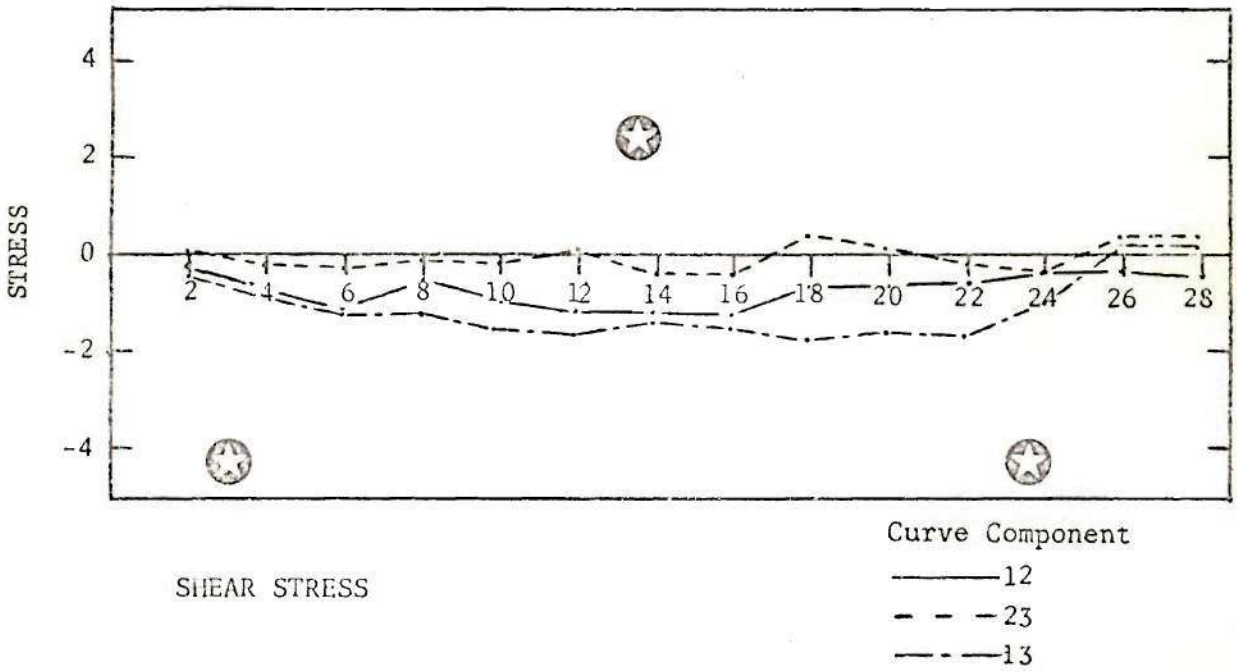

Figure 21. Normal and shear stress results for two-layer model for solution station (I') in 2 direction for J' (1 direction) = 4, K = 4.

Refer to explanation preceding Fig. 14 and to Figs. 2 and 13.

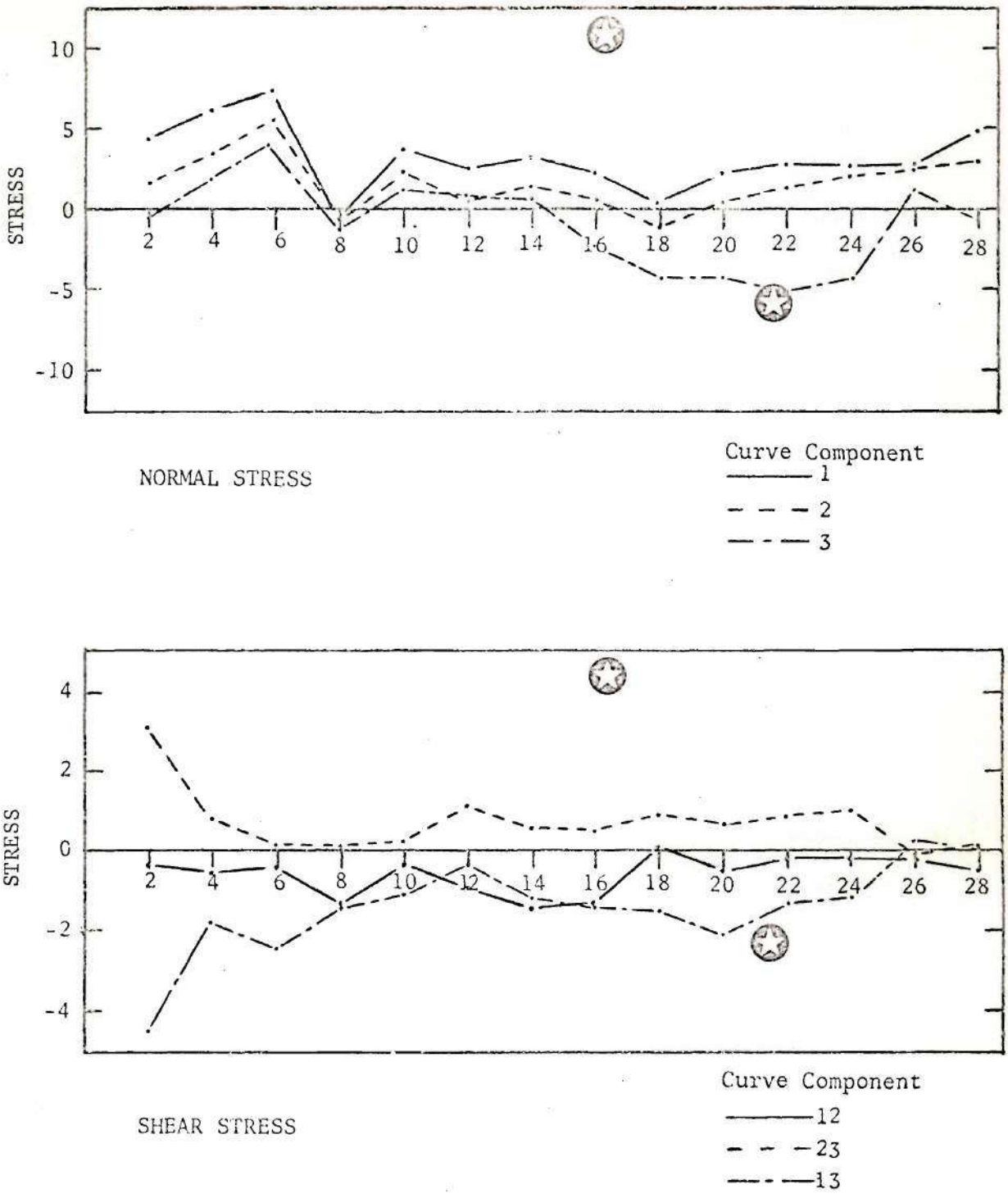

Figure 22. Normal and shear stress results for two-layer model for solution station (I') in 2 direction for J' (1 direction) = 6, K = 1.

Refer to explanation preceding Fig. 14 and to Figs. 2 and 13.

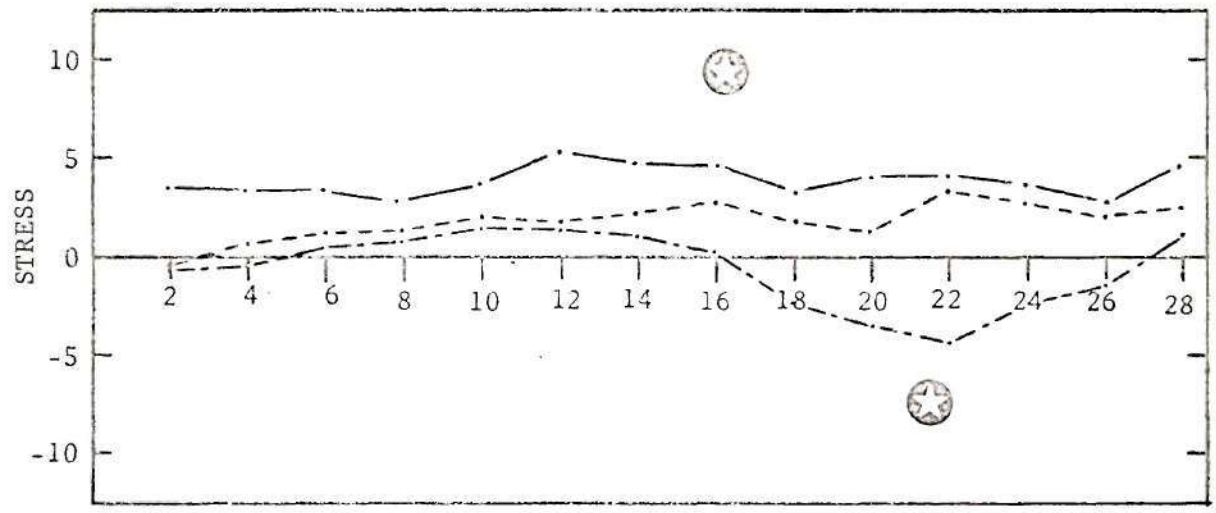

NORMAL STRESS

Curve Component
1
2
3

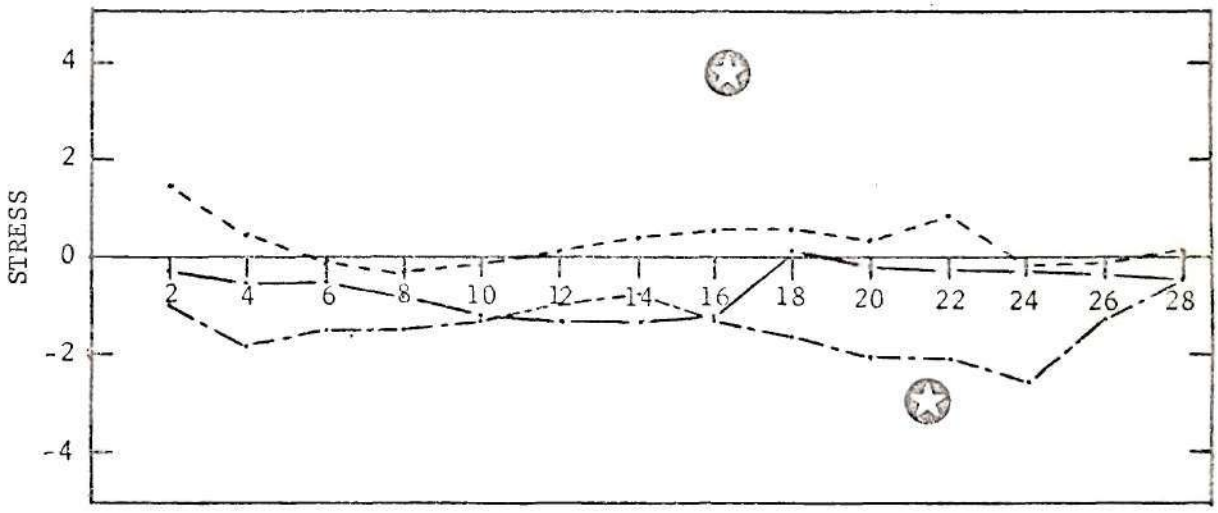

SHEAR STRESS

Curve Component
12
23
13

Figure 23. Normal and shear stress results for two-layer model for solution station (I') in 2 direction for J' (1 direction) = 6, K = 2.

Refer to explanation preceding Fig. 14 and to Figs. 2 and 13.

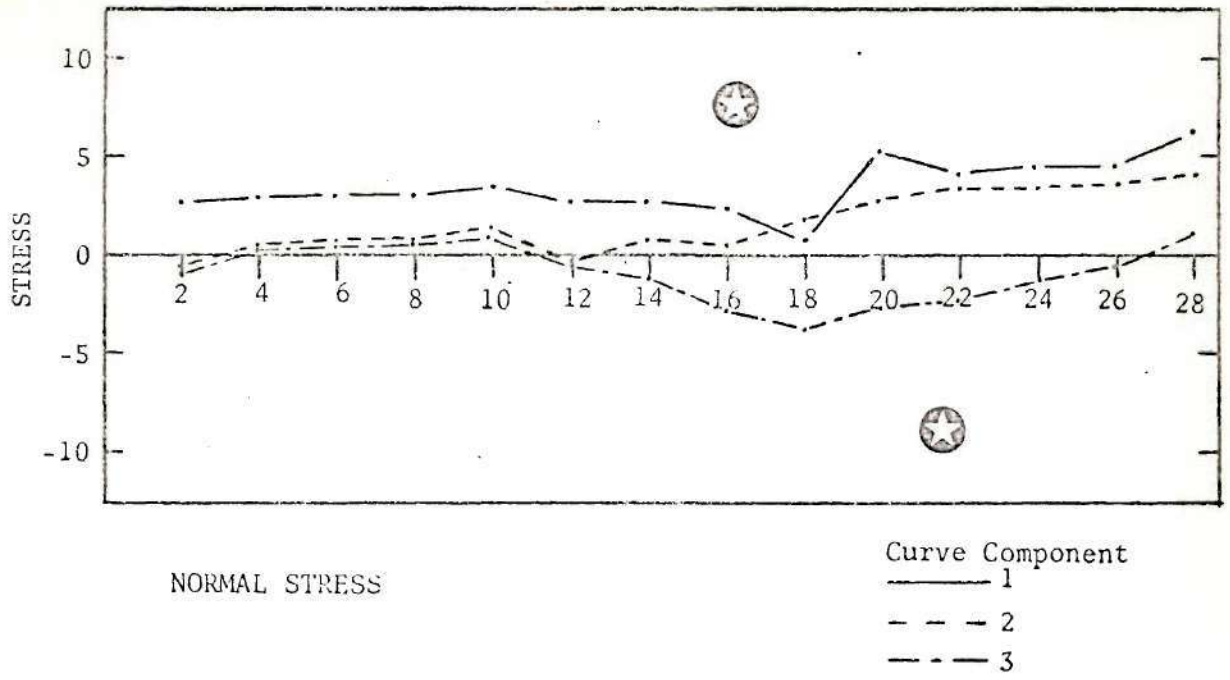

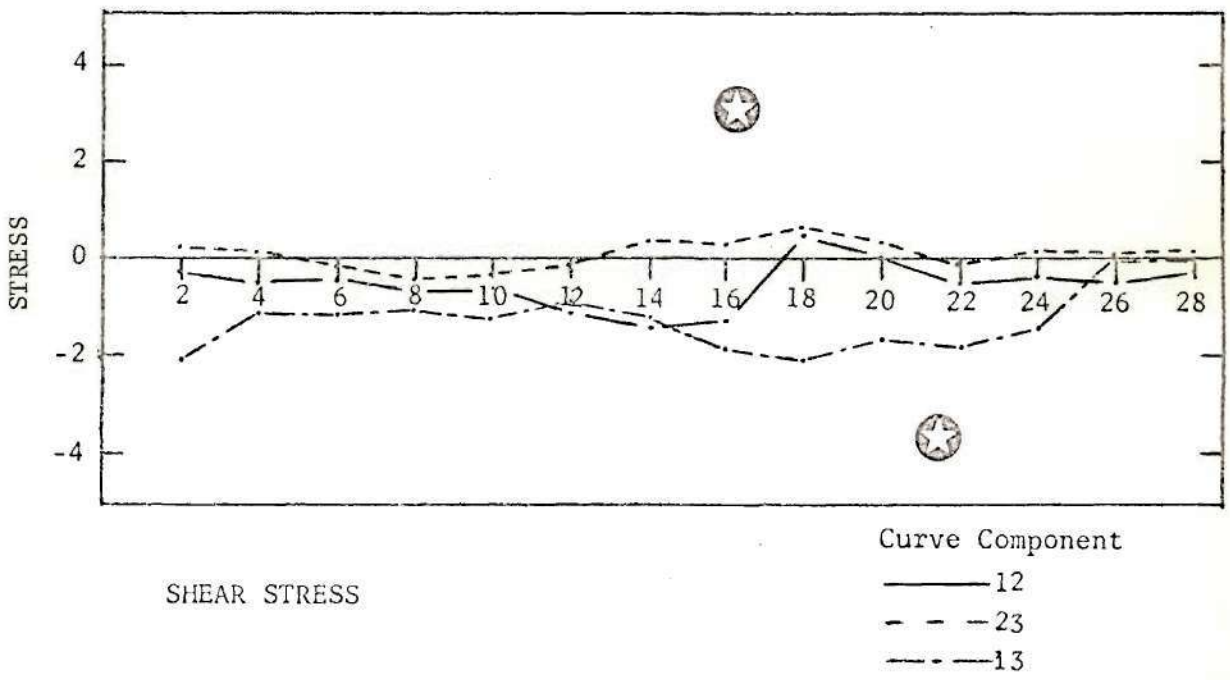

Figure 24. Normal and shear stress results for two-layer model for solution station (I') in 2 direction for J' (1 direction) = 6, K = 3.

Refer to explanation preceding Fig. 14 and to Figs. 2 and 13.

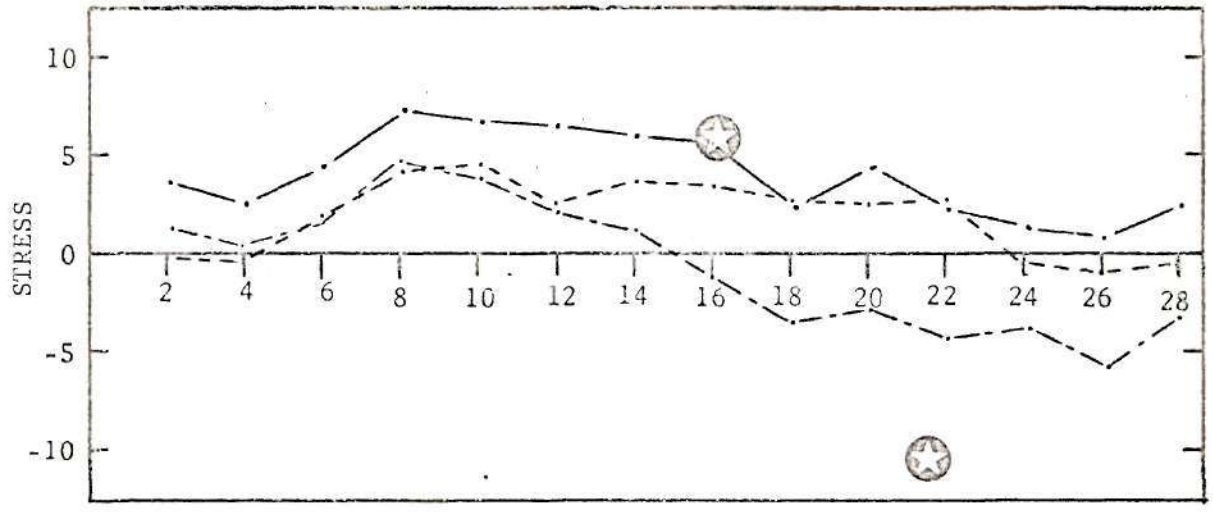

NORMAL STRESS

Curve Component
1
2
3

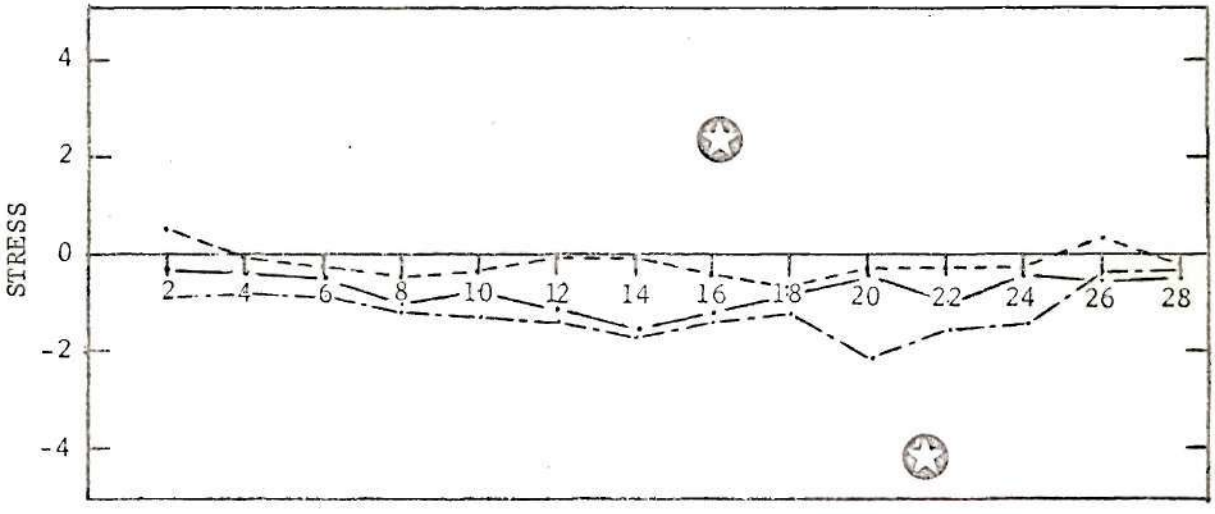

SHEAR STRESS

Curve Component
12
23
13

Figure 25. Normal and shear stress results for two-layer model for solution station (I') in 2 direction for J' (1 direction) = 6, K = 4.

Refer to explanation preceding Fig. 14 and to Figs. 2 and 13.

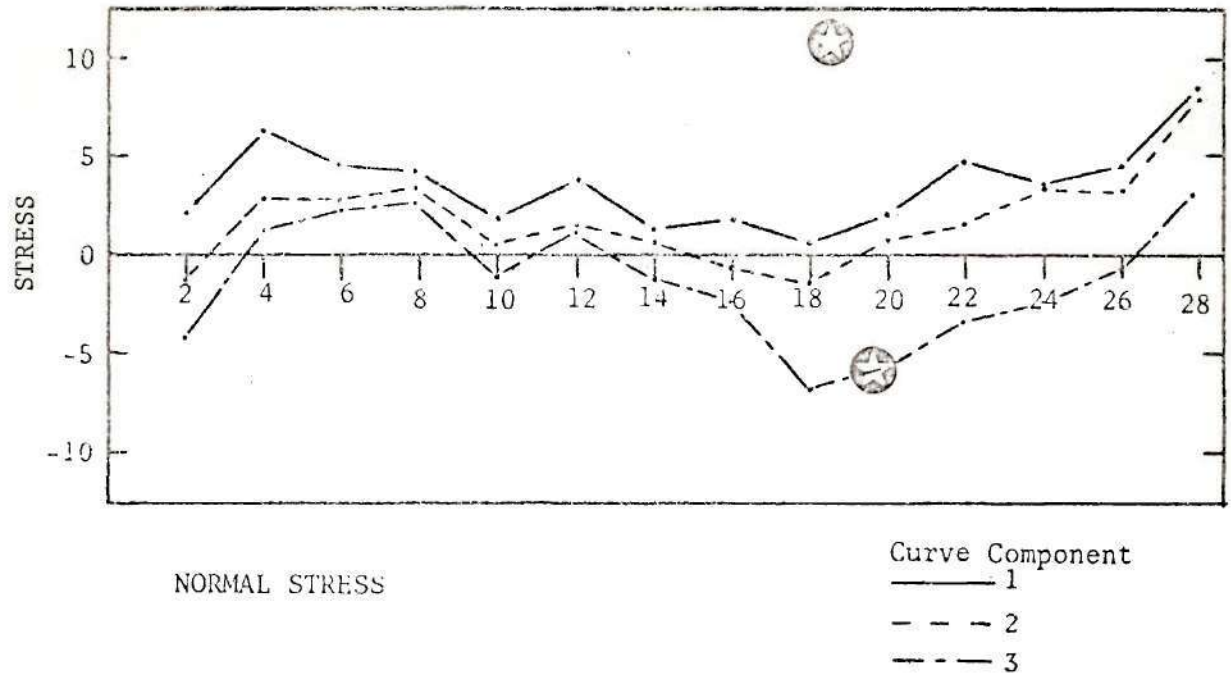

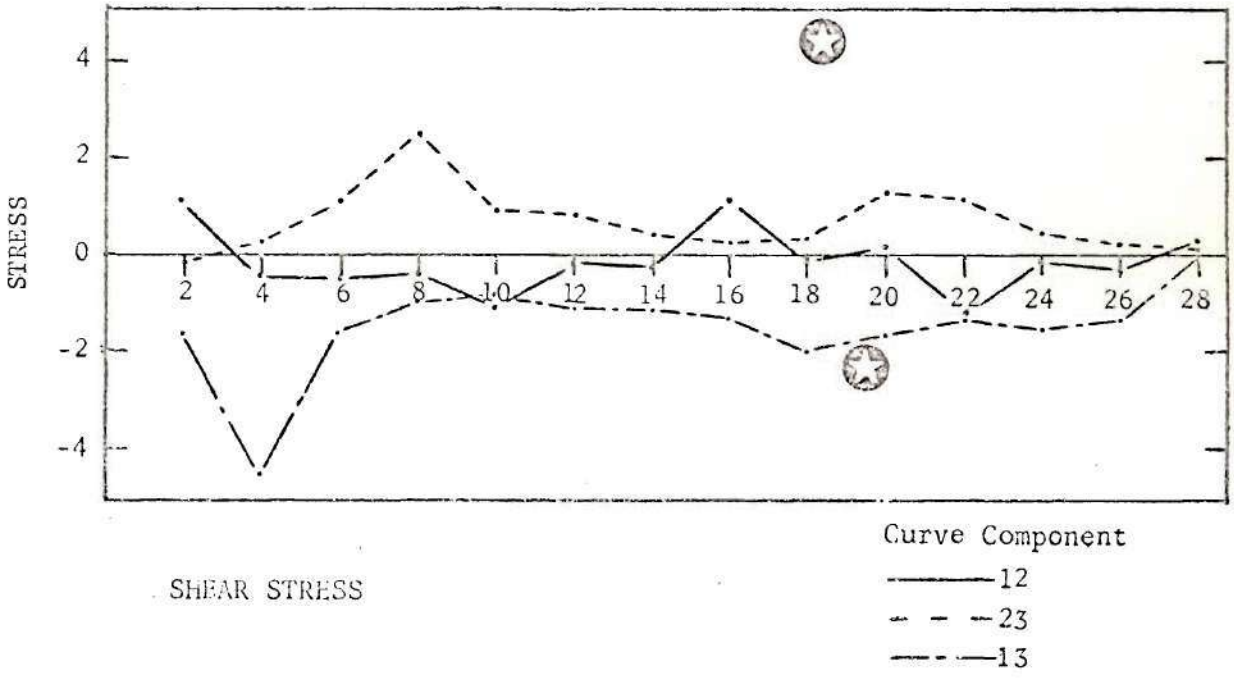

Figure 26. Normal and shear stress results for two-layer model for solution station (I') in 2 direction for J' (1 direction) = 8, K = 1.

Refer to explanation preceding Fig. 14 and to Figs. 2 and 13.

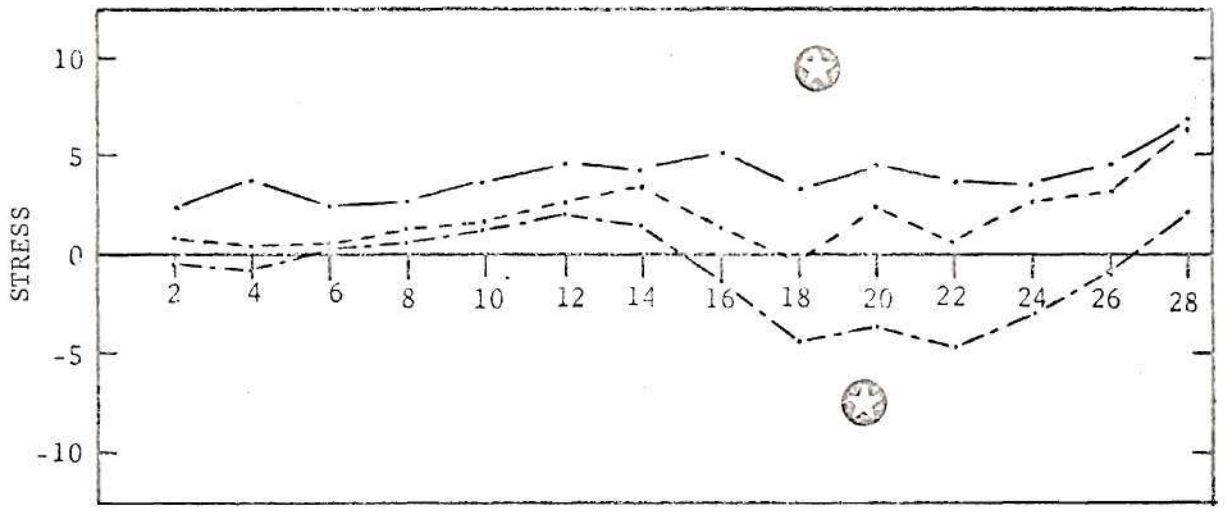

NORMAL STRESS

Curve Component
1
2
3

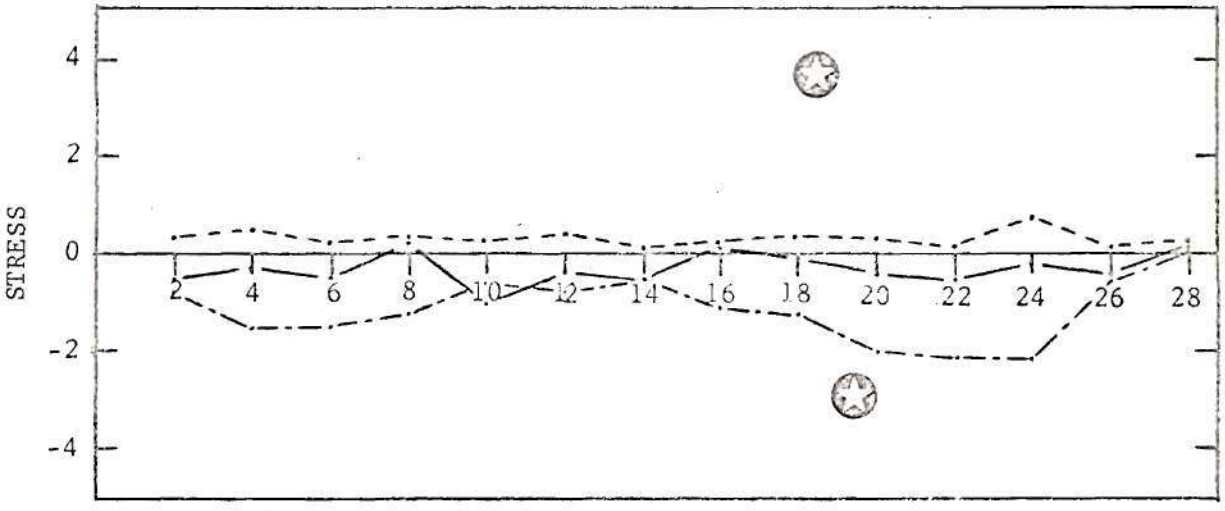

SHEAR STRESS

Curve Component
12
23
13

Figure 27. Normal and shear stress results for two-layer model for solution station (I') in 2 direction for J' (1 direction) = 8, K = 2.

Refer to explanation preceding Fig. 14 and to Figs. 2 and 13.

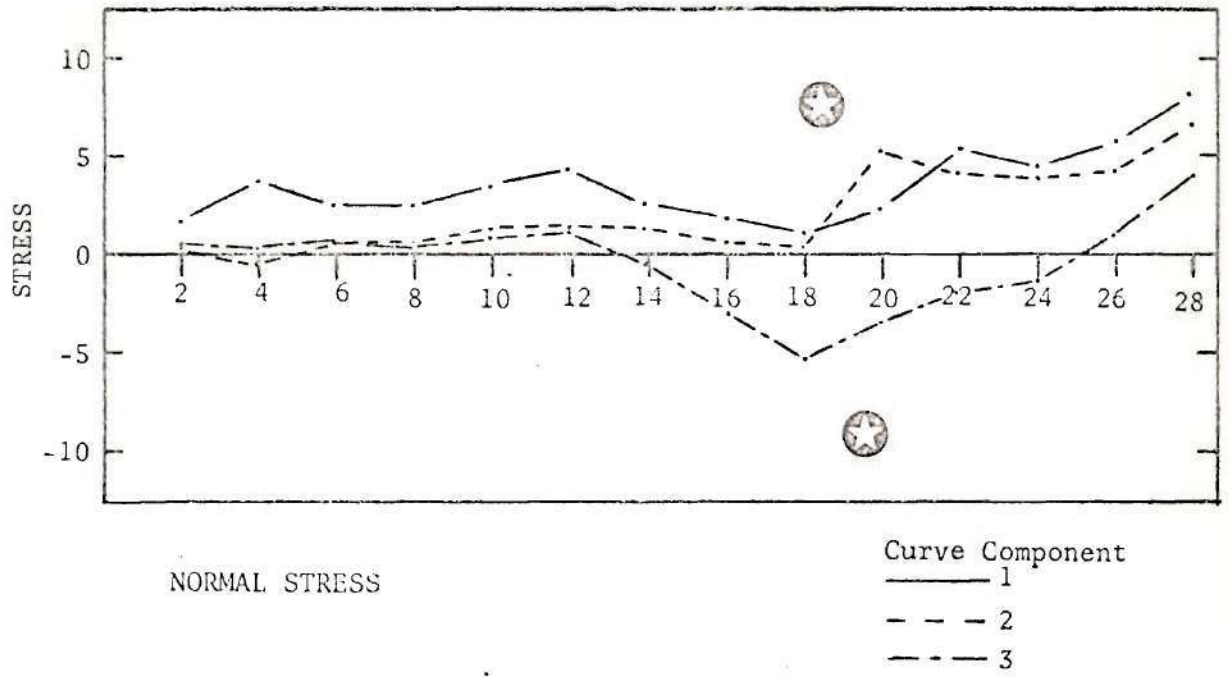

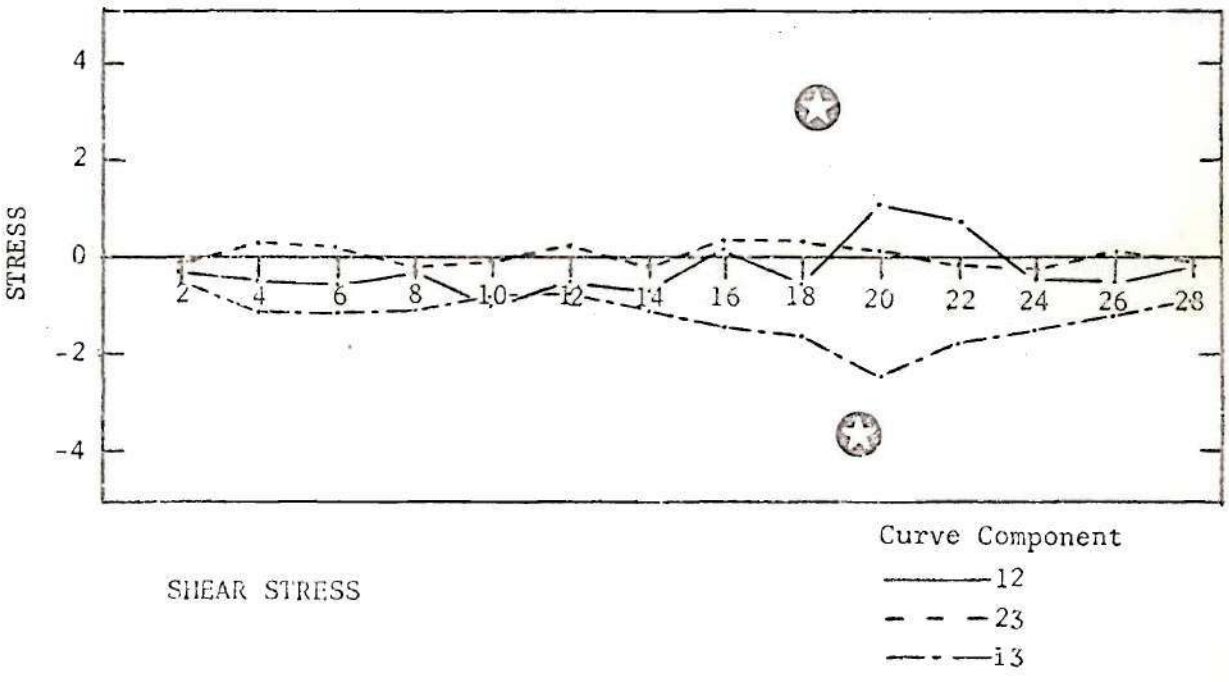

Figure 28. Normal and shear stress results for two-layer model for solution station (I') in 2 direction for J' (1 direction) = 8, K = 3.

Refer to explanation preceding Fig. 14 and to Figs. 2 and 13.

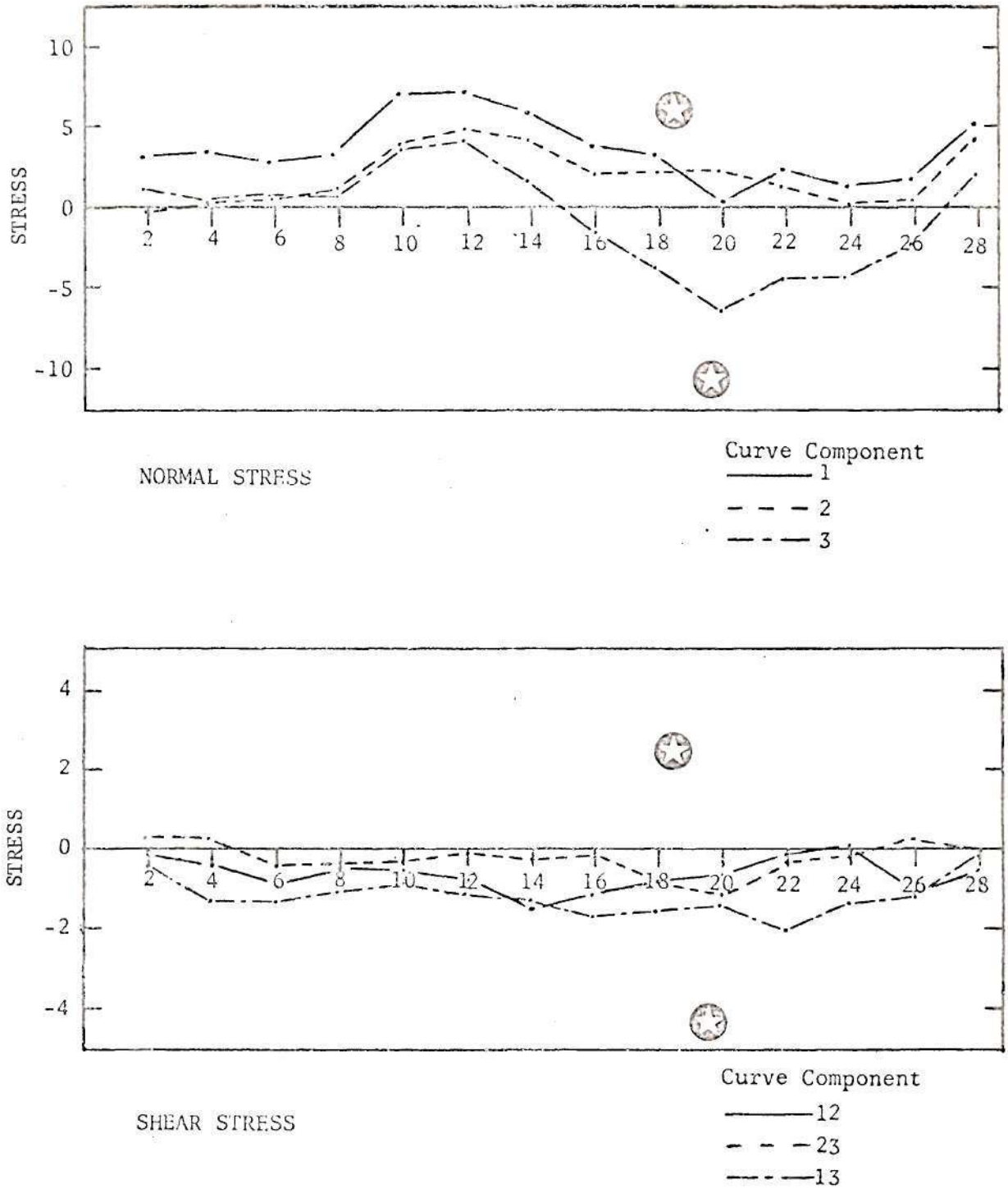

Figure 29. Normal and shear stress results for two-layer model for solution station (I') in 2 direction for J' (1 direction) = 8, K = 4.

Refer to explanation preceding Fig. 14 and to Figs. 2 and 13.

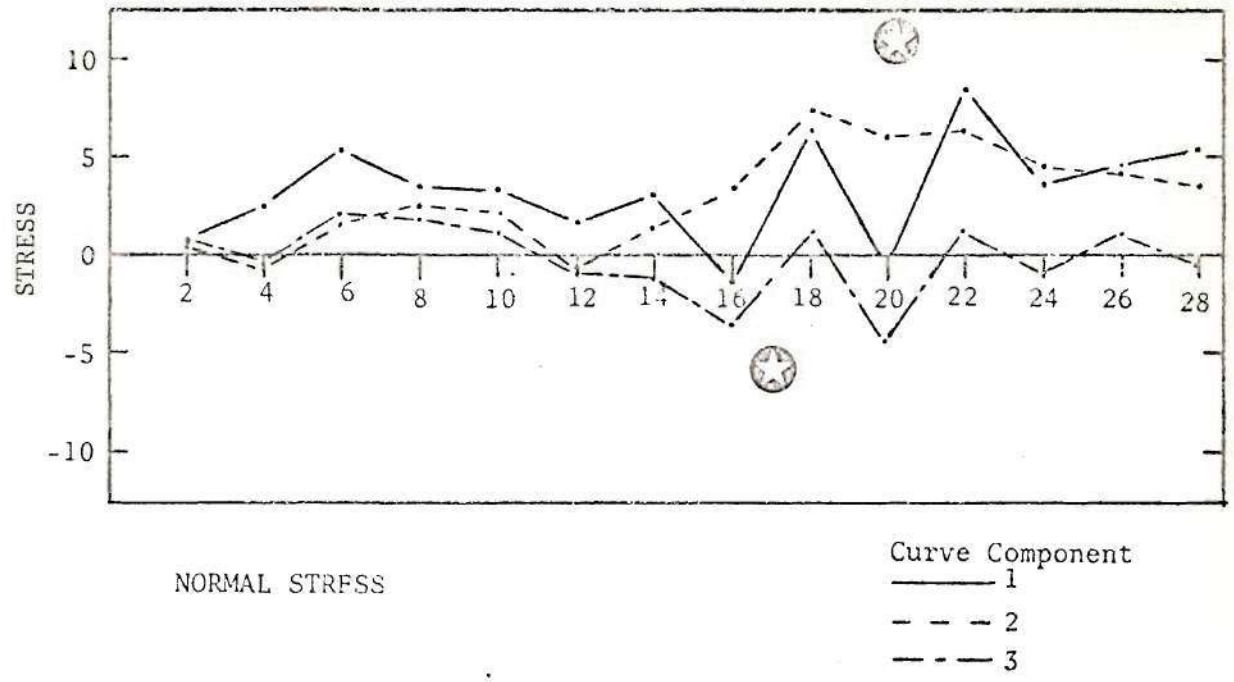

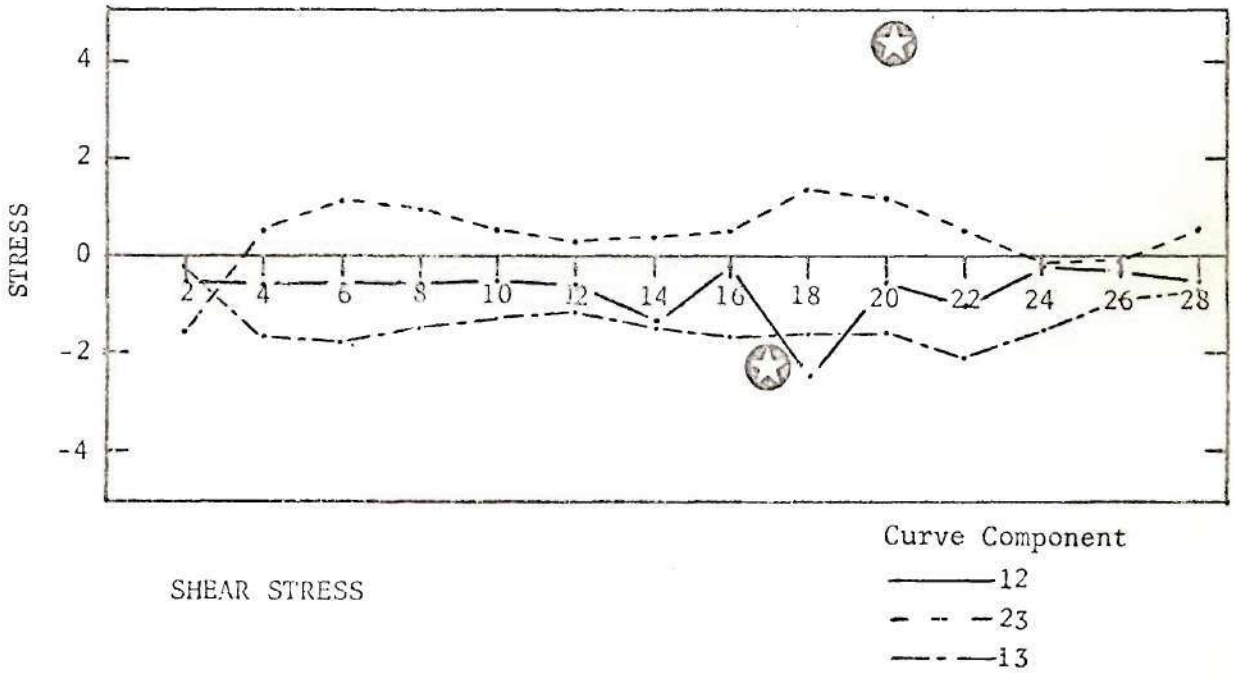

Figure 30. Normal and shear stress results for two-layer model for solution station (I') in 2 direction for J' (1 direction) = 10, K = 1.

Refer to explanation preceding Fig. 14 and to Figs. 2 and 13.

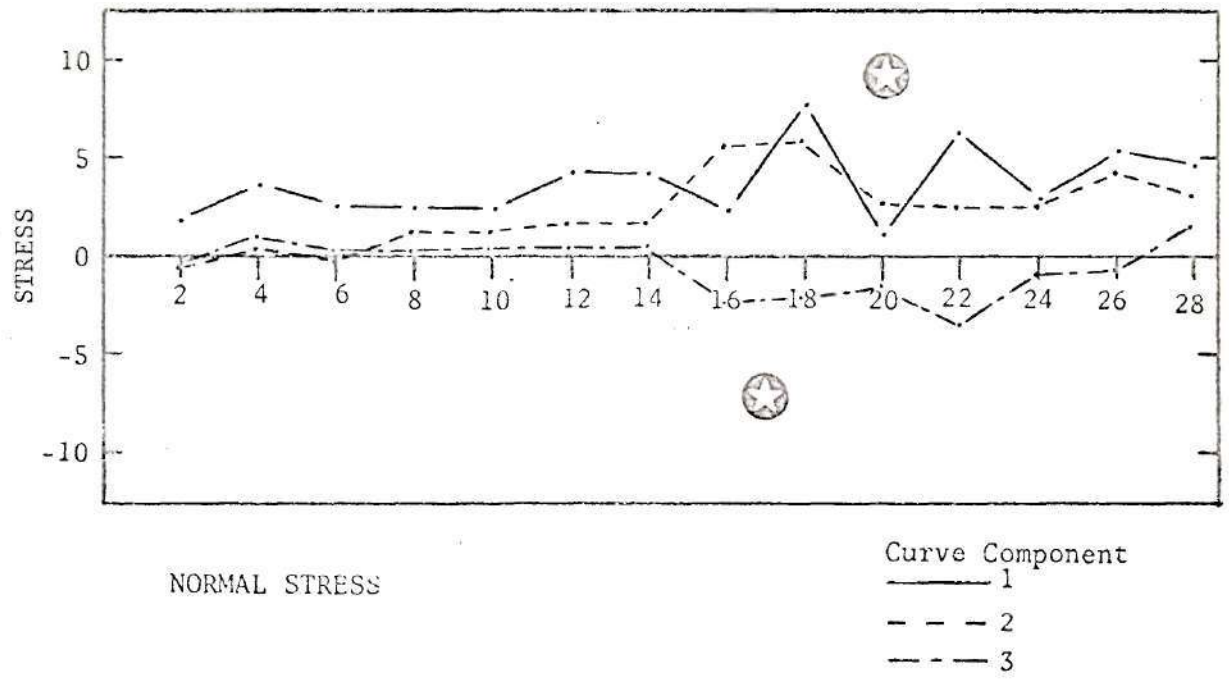

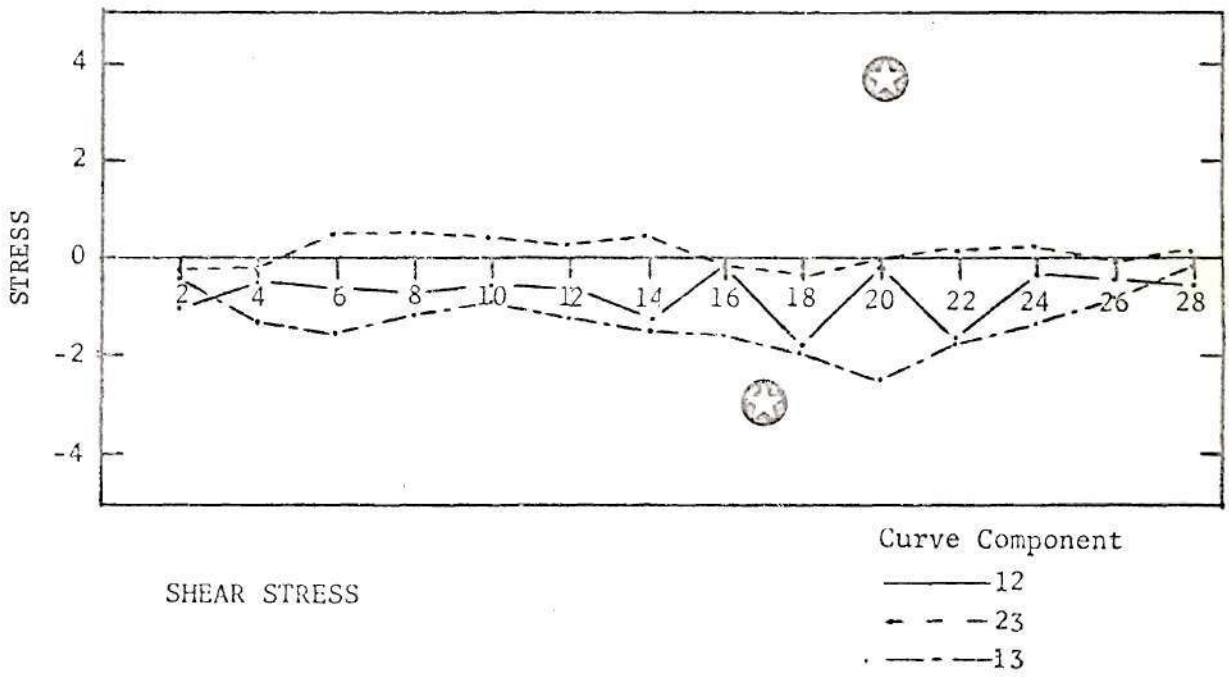

Figure 31. Normal and shear stress results for two-layer model for solution station (I') in 2 direction for J' (1 direction) = 10, K = 2.

Refer to explanation preceding Fig. 14 and to Figs. 2 and 13.

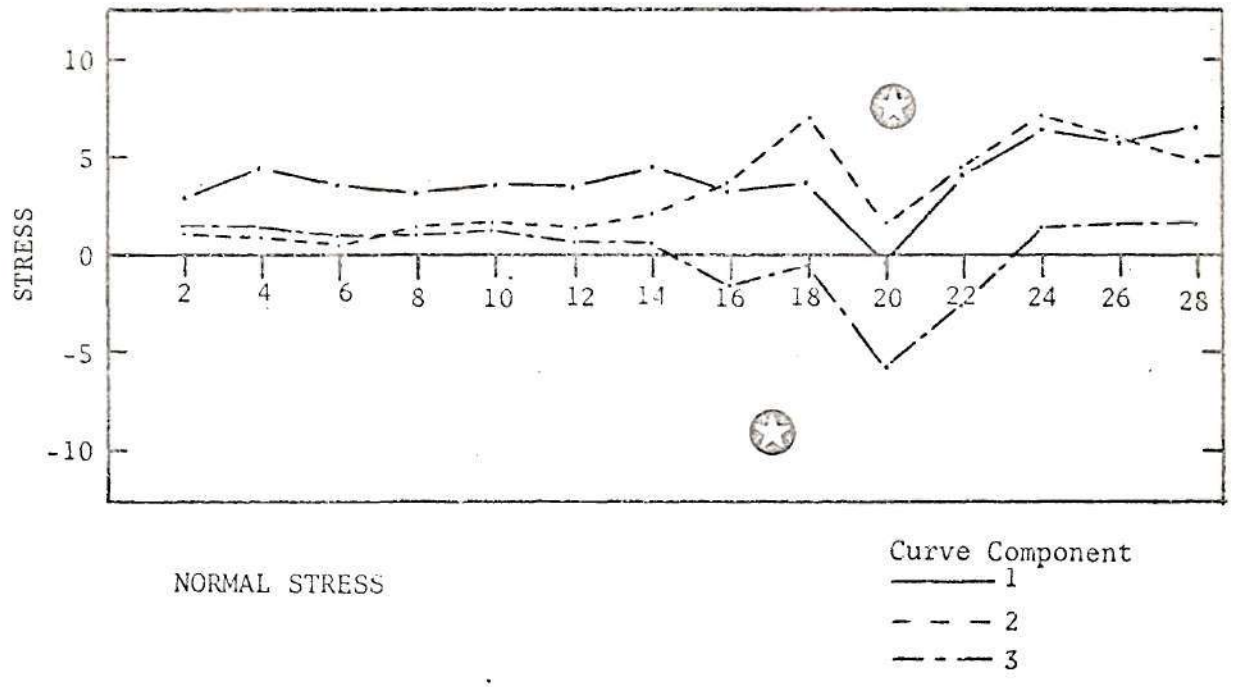

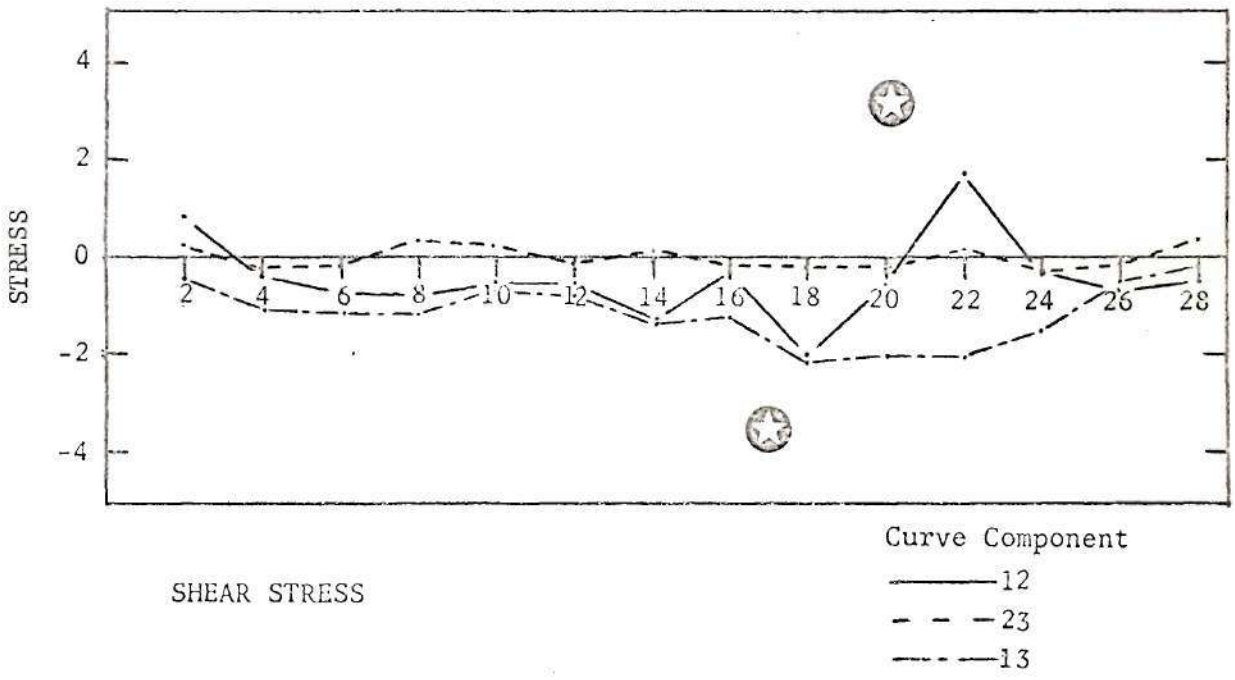

Figure 32. Normal and shear stress results for two-layer model for solution station (I') in 2 direction for J' (1 direction) = 10, K = 3.

Refer to explanation preceding Fig. 14 and to Figs. 2 and 13.

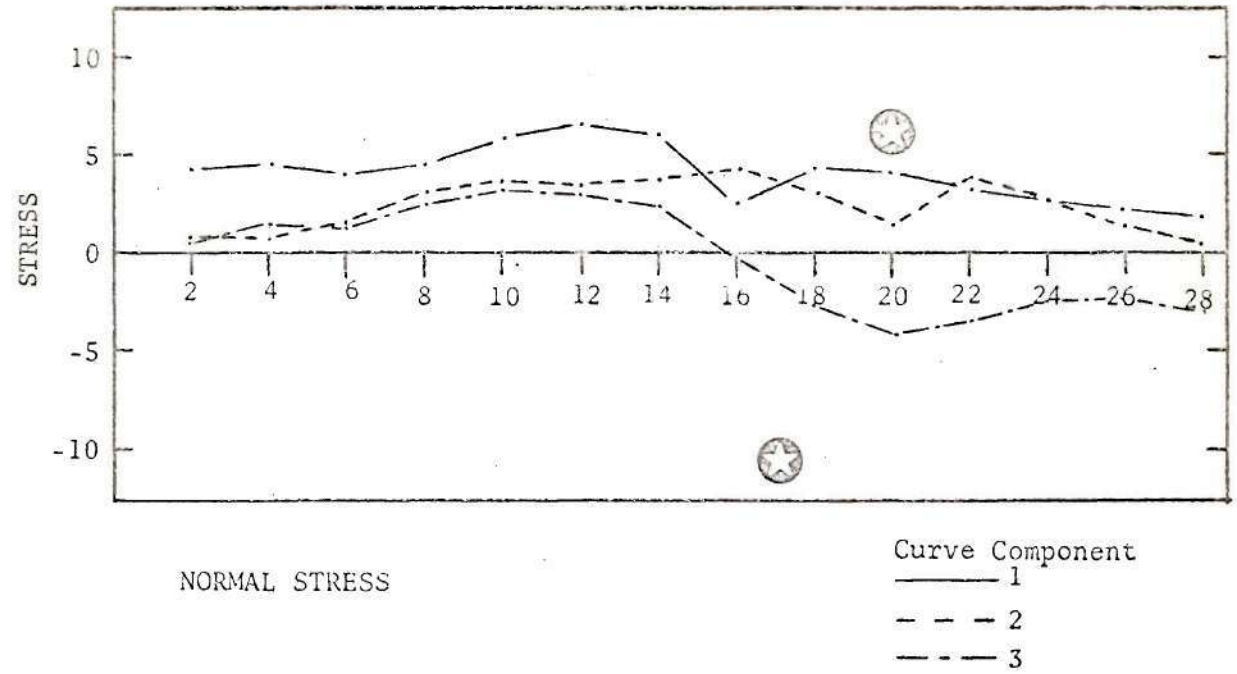

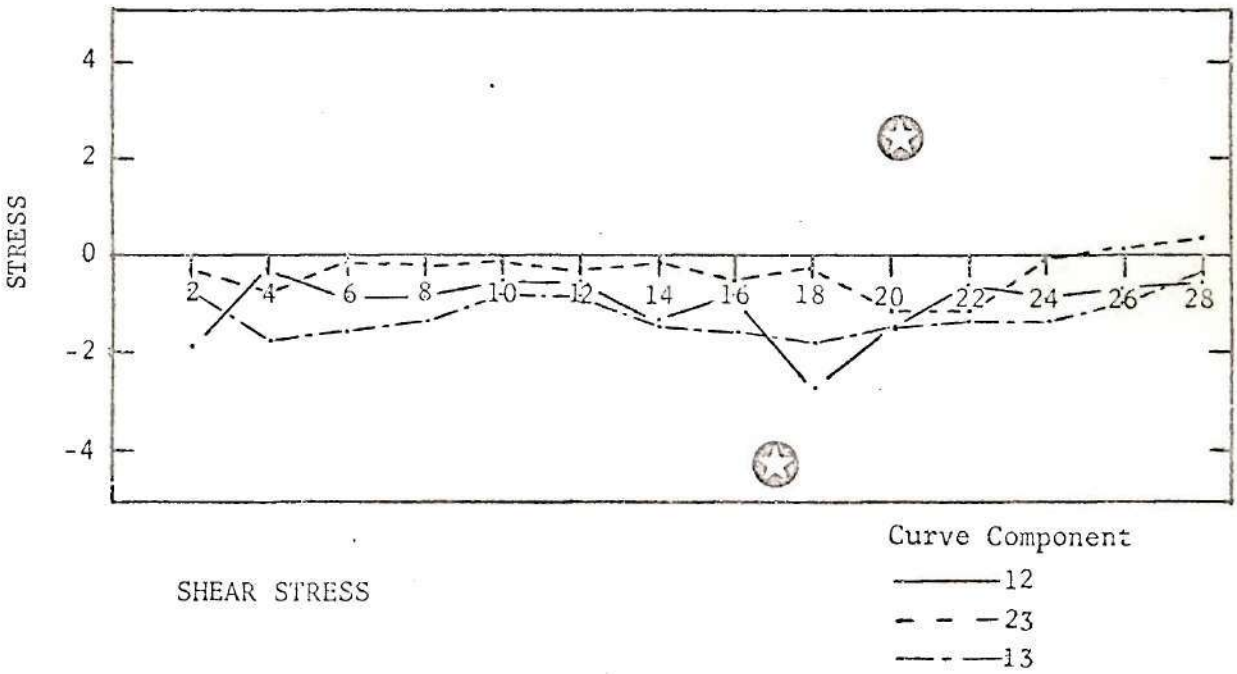

Figure 33. Normal and shear stress results for two-layer model for solution station (I') in 2 direction for J' (1 direction) = 10, K = 4.

Refer to explanation preceding Fig. 14 and to Figs. 2 and 13.

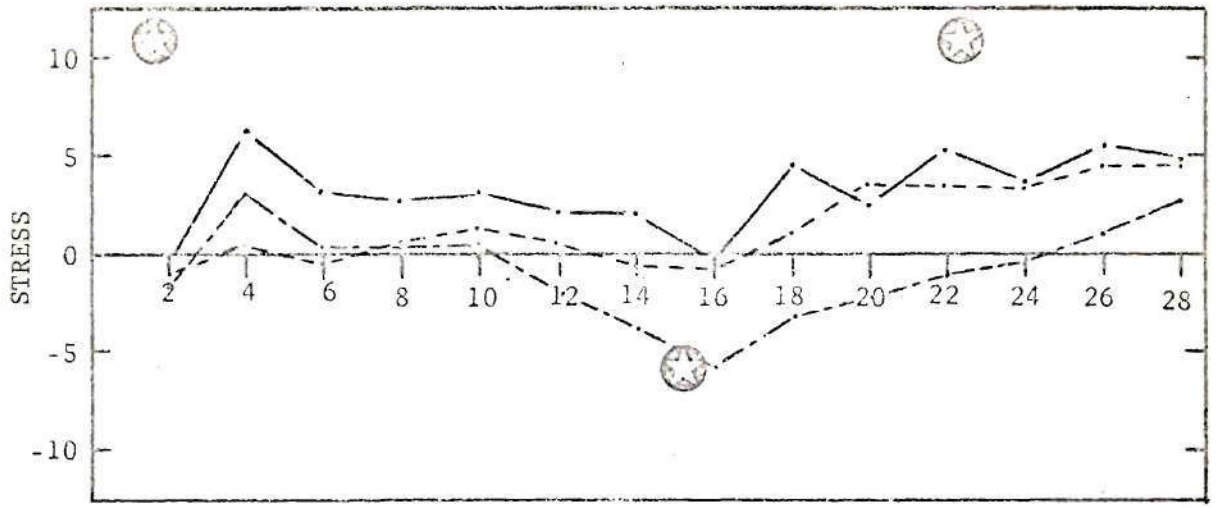

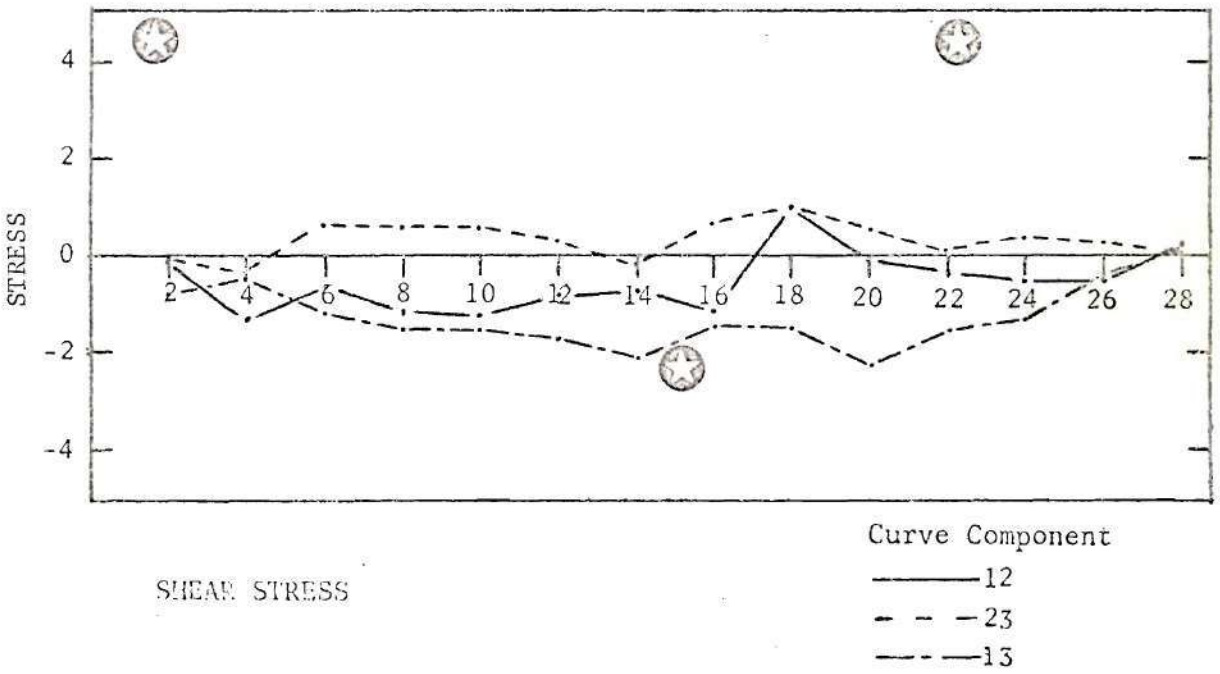

Figure 34. Normal and shear stress results for two-layer model for solution station (I') in 2 direction for J' (1 direction) = 12, K = 1.

Refer to explanation preceding Fig. 14 and to Figs. 2 and 13.

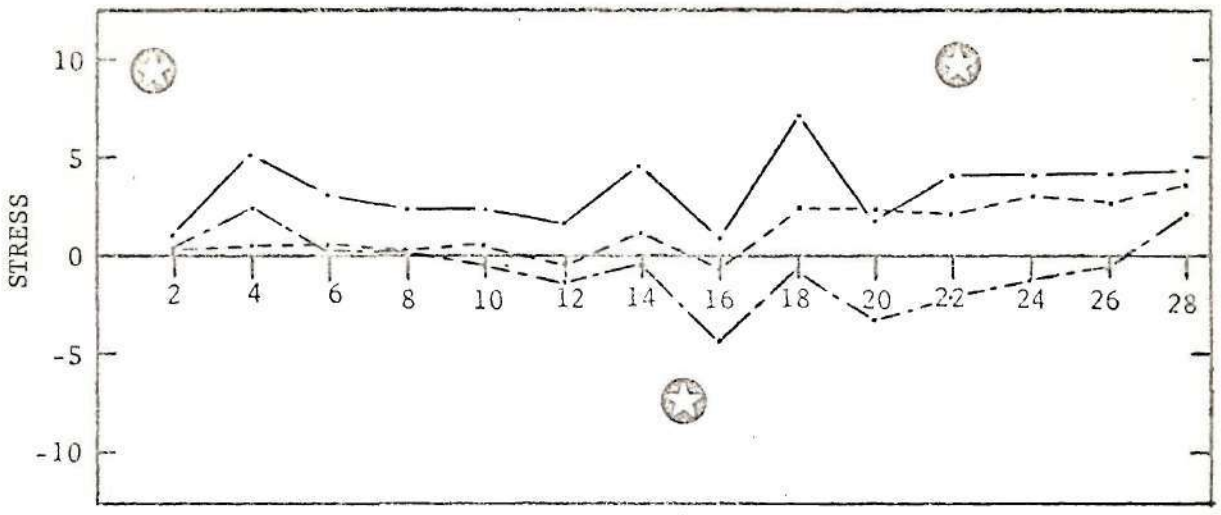

NORMAL STRESS

Curve Component
1
2
3

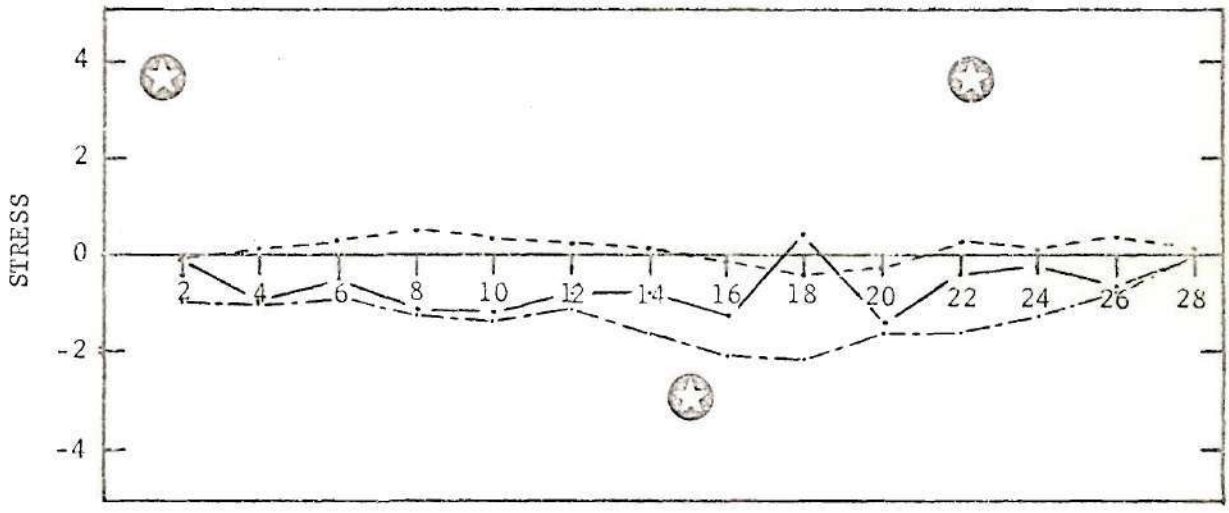

SHEAR STRESS

Curve Component
12
23
13

Figure 35. Normal and shear stress results for two-layer model for solution station (I') in 2 direction for J' (1 direction) = 12, K = 2.

Refer to explanation preceding Fig. 14 and to Figs. 2 and 13.

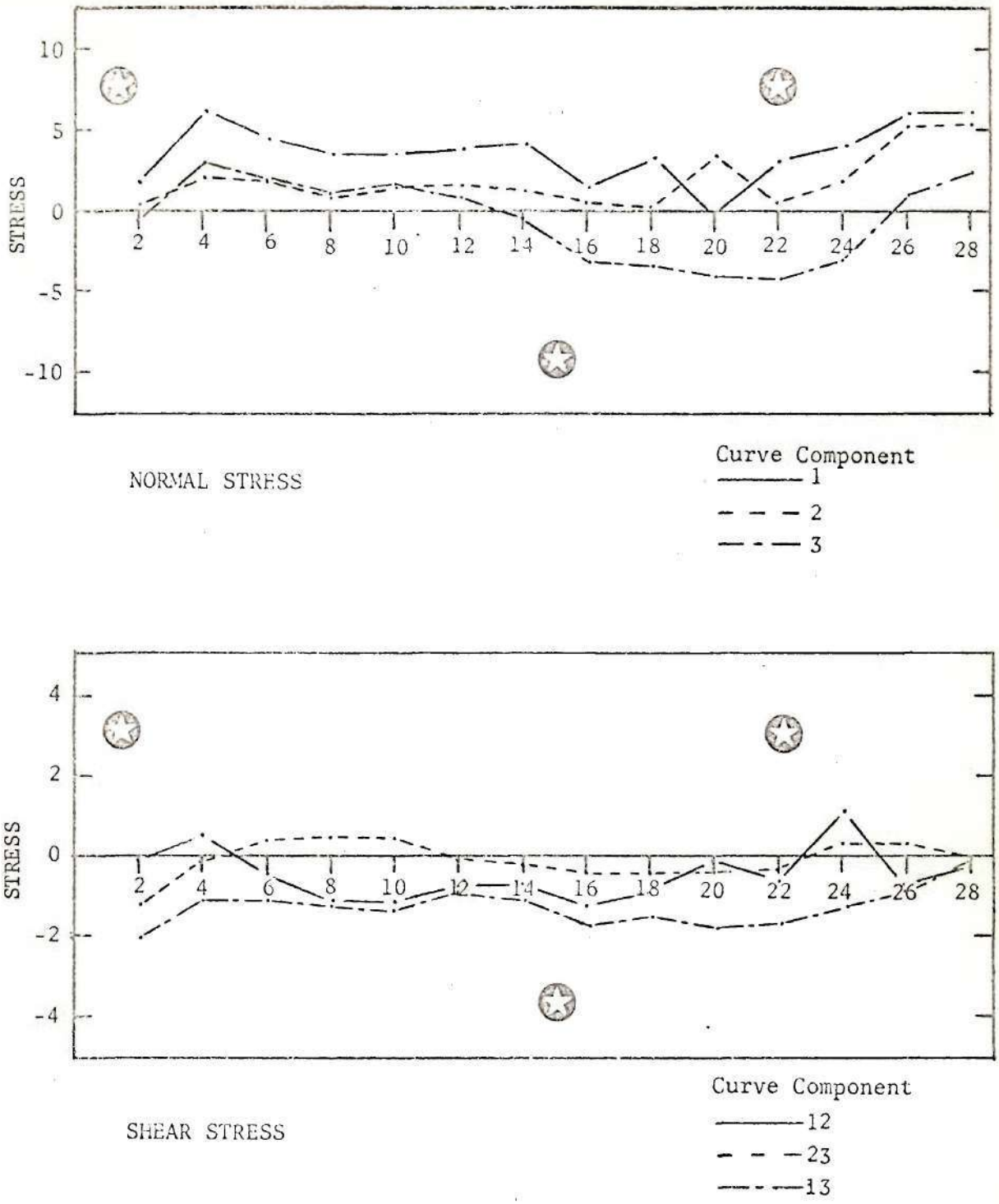

Figure 36. Normal and shear stress results for two-layer model for solution station (I') in 2 direction for J' (1 direction) = 12, K = 3.

Refer to explanation preceding Fig. 14 and to Figs. 2 and 13.

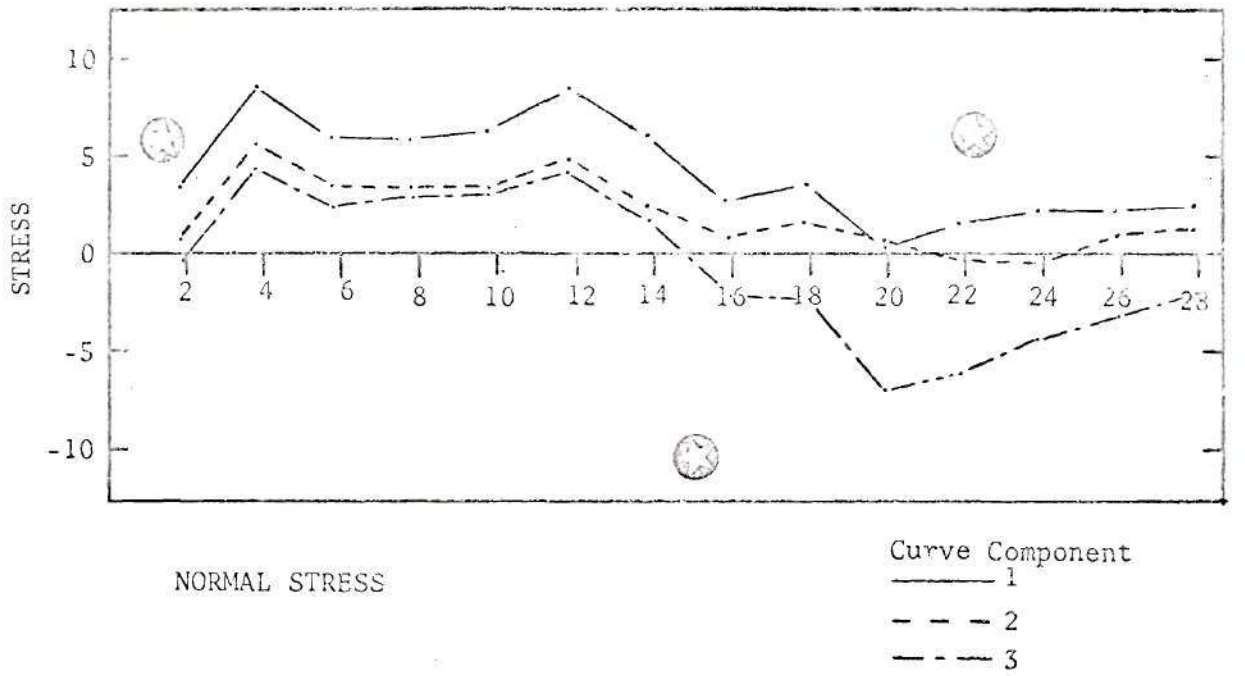

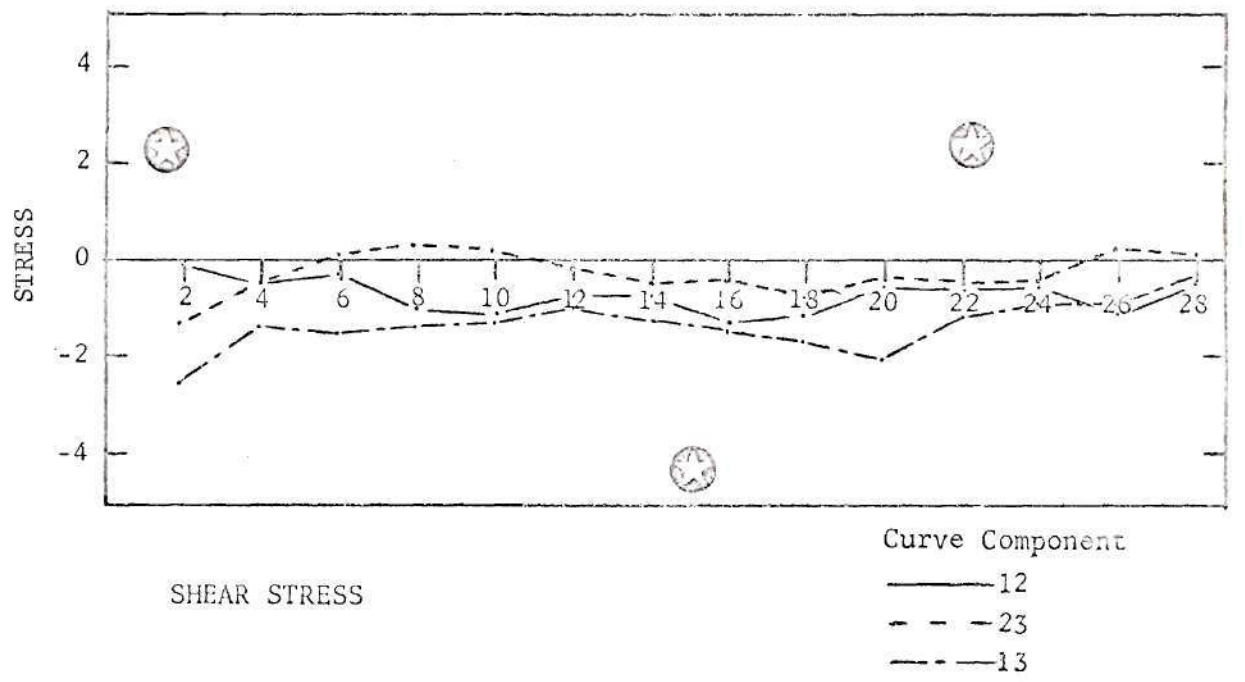

Figure 37. Normal and shear stress results for two-layer model for solution station (I') in 2 direction for J' (1 direction) = 12, K = 4.

Refer to explanation preceding Fig. 14 and to Figs. 2 and 13.

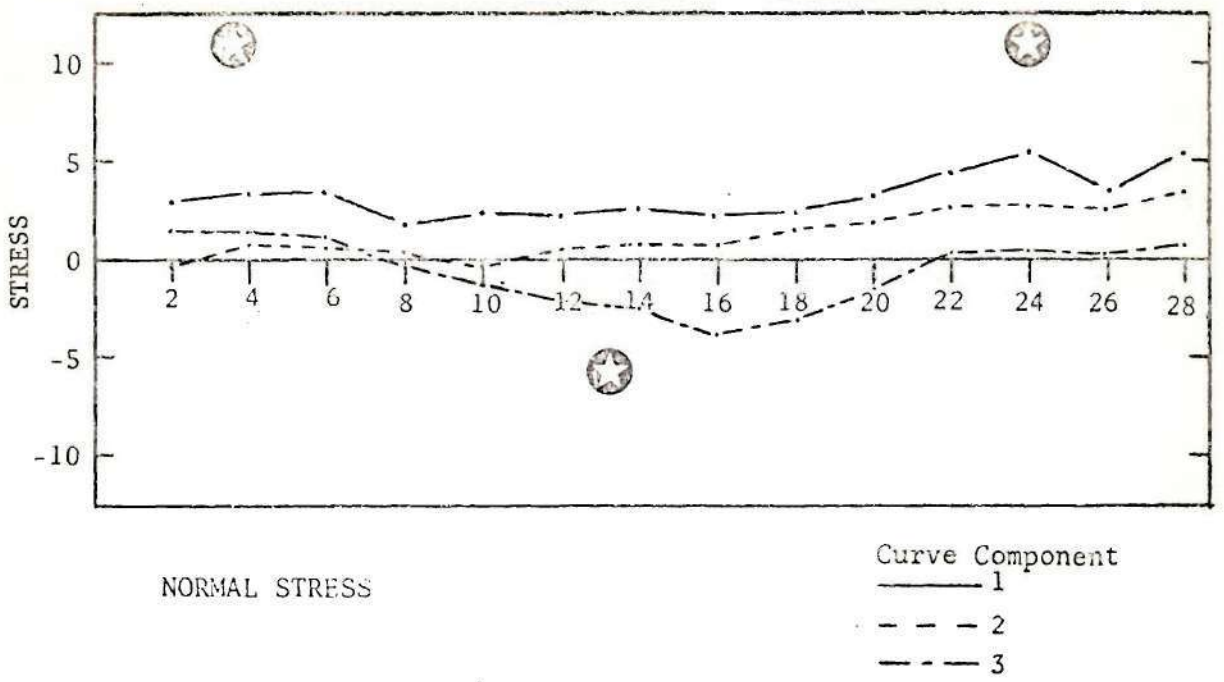

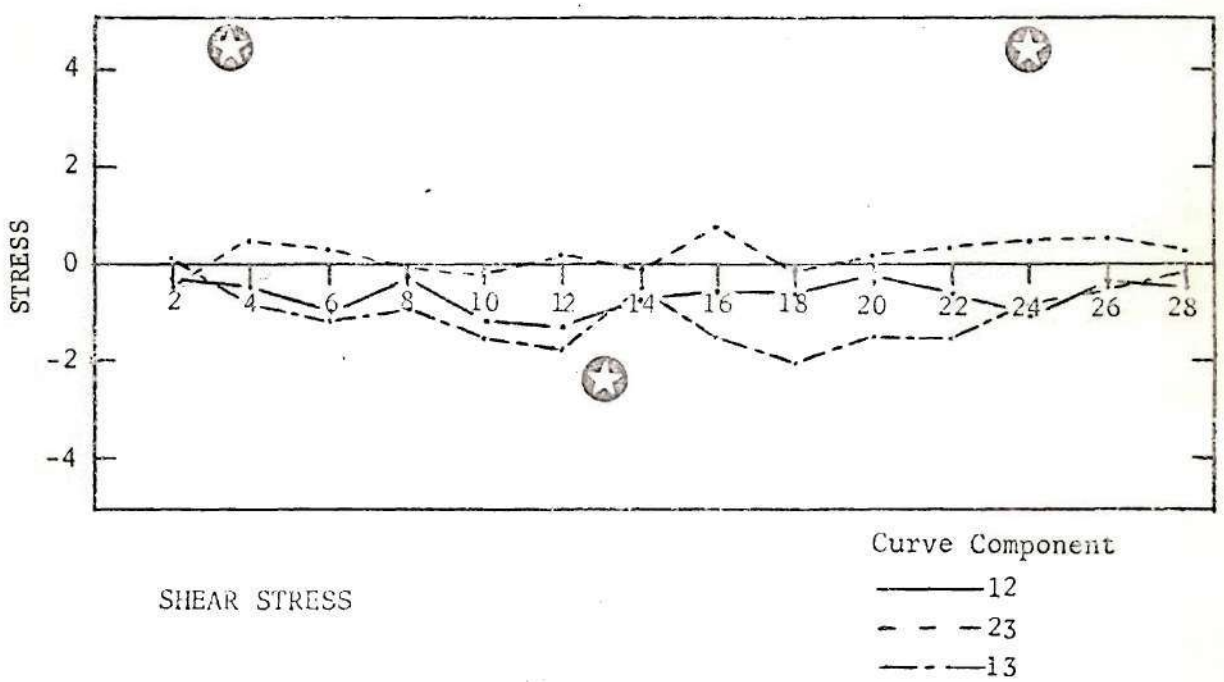

Figure 38. Normal and shear stress results for two-layer model for solution station (I') in 2 direction for J' (1 direction) = 14, K = 1.

Refer to explanation preceding Fig. 14 and to Figs. 2 and 13.

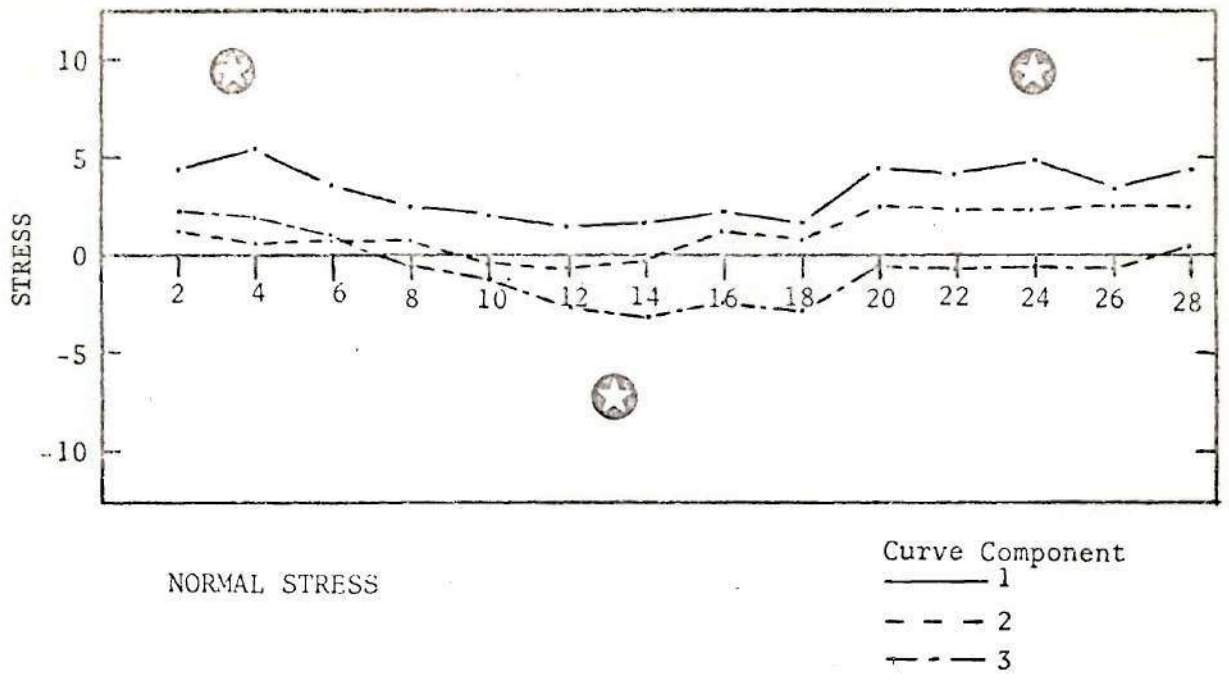

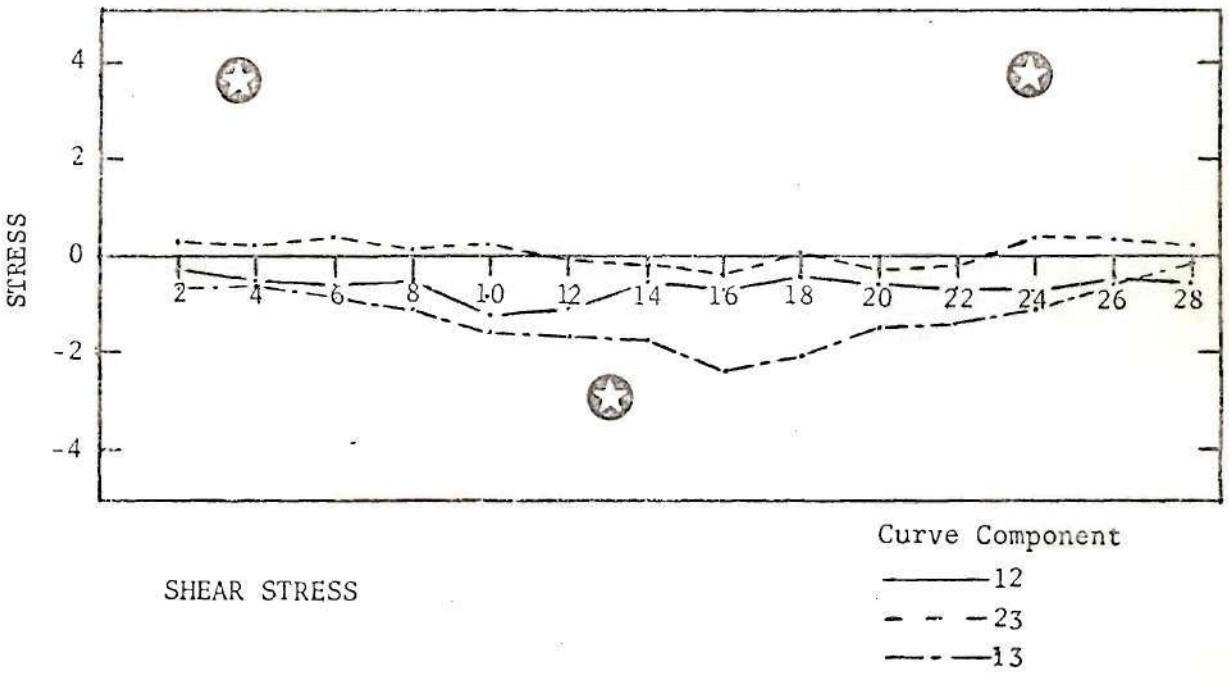

Figure 39. Normal and shear stress results for two-layer model for solution station (I') in 2 direction for J' (1 direction) = 14, K = 2.

Refer to explanation preceding Fig. 14 and to Figs. 2 and 13.

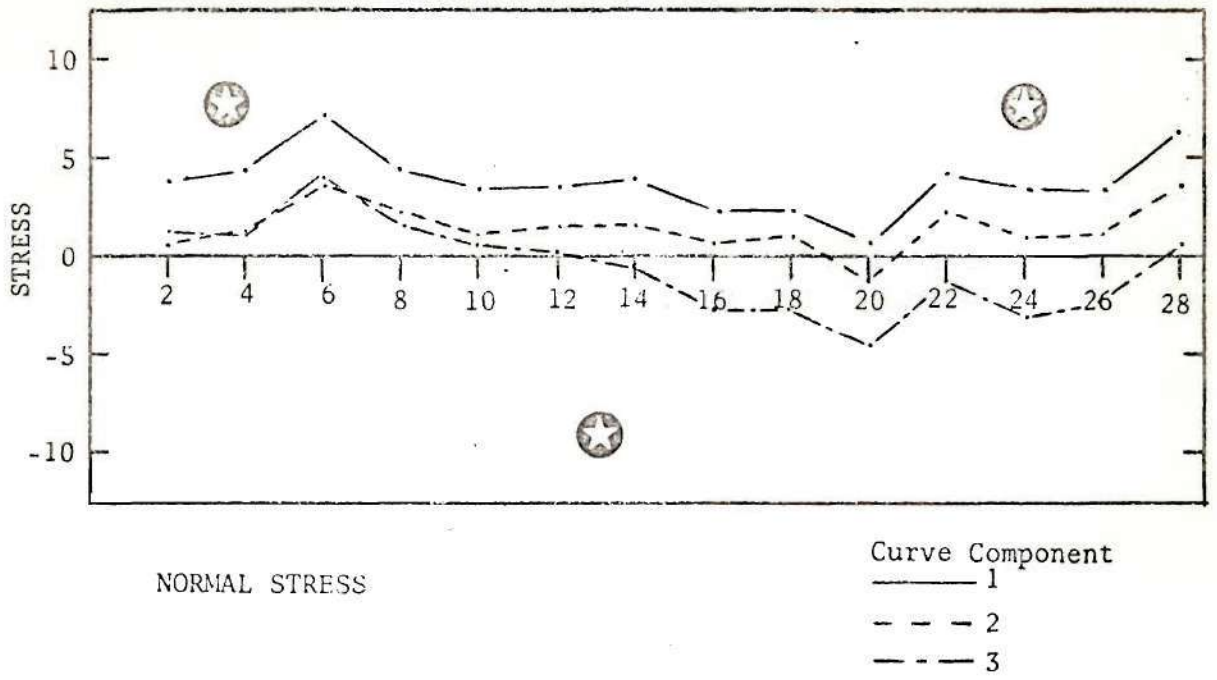

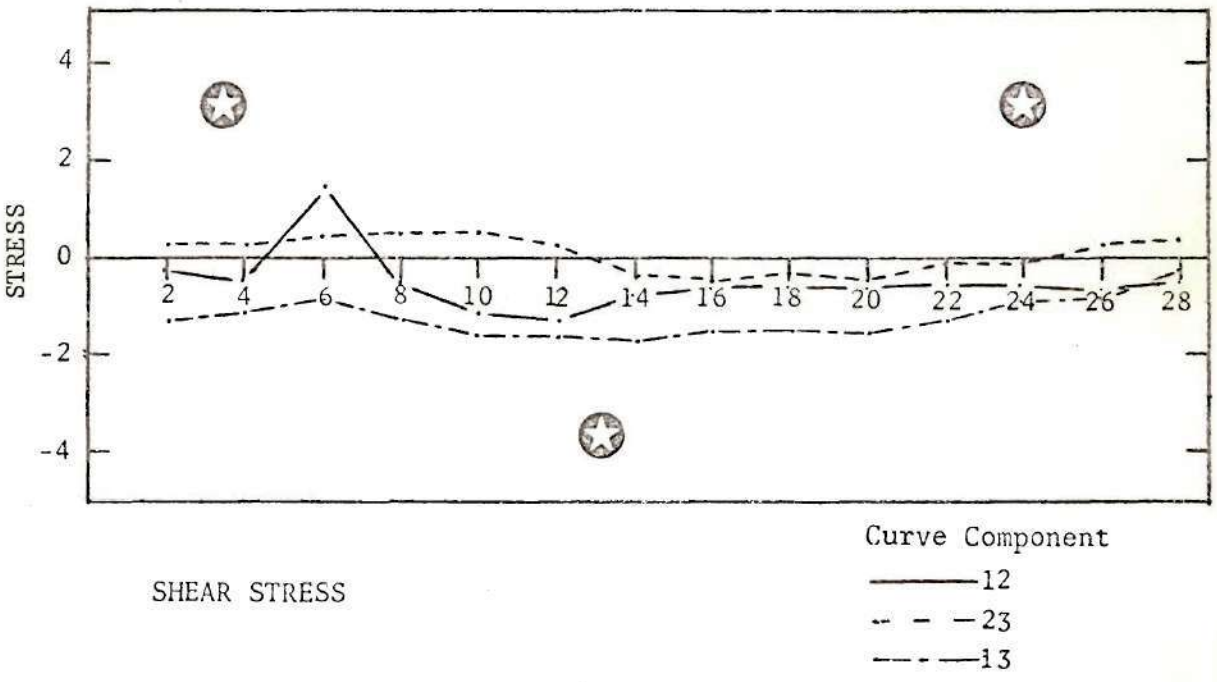

Figure 40. Normal and shear stress results for two-layer model for solution station (I') in 2 direction for J' (1 direction) = 14, K = 3.

Refer to explanation preceding Fig. 14 and to Figs. 2 and 13.

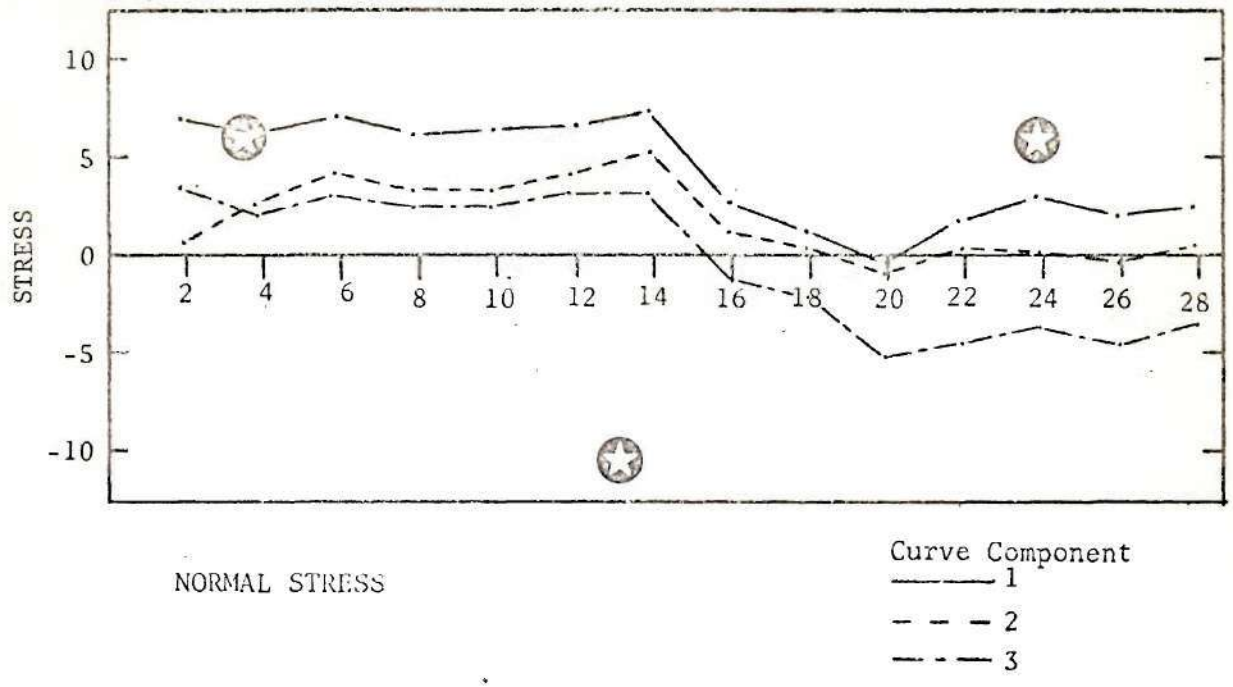

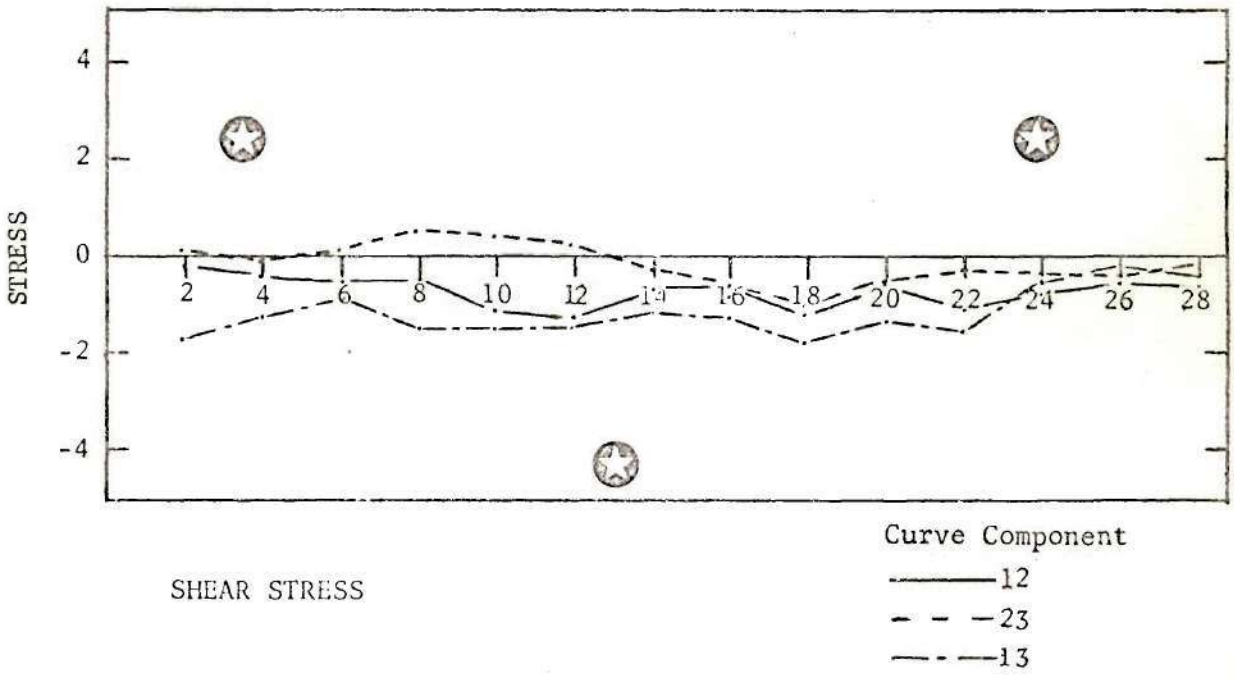

Figure 41. Normal and shear stress results for two-layer model for solution station (I') in 2 direction for J' (1 direction) = 14, K = 4.

Refer to explanation preceding Fig. 14 and to Figs. 2 and 13.

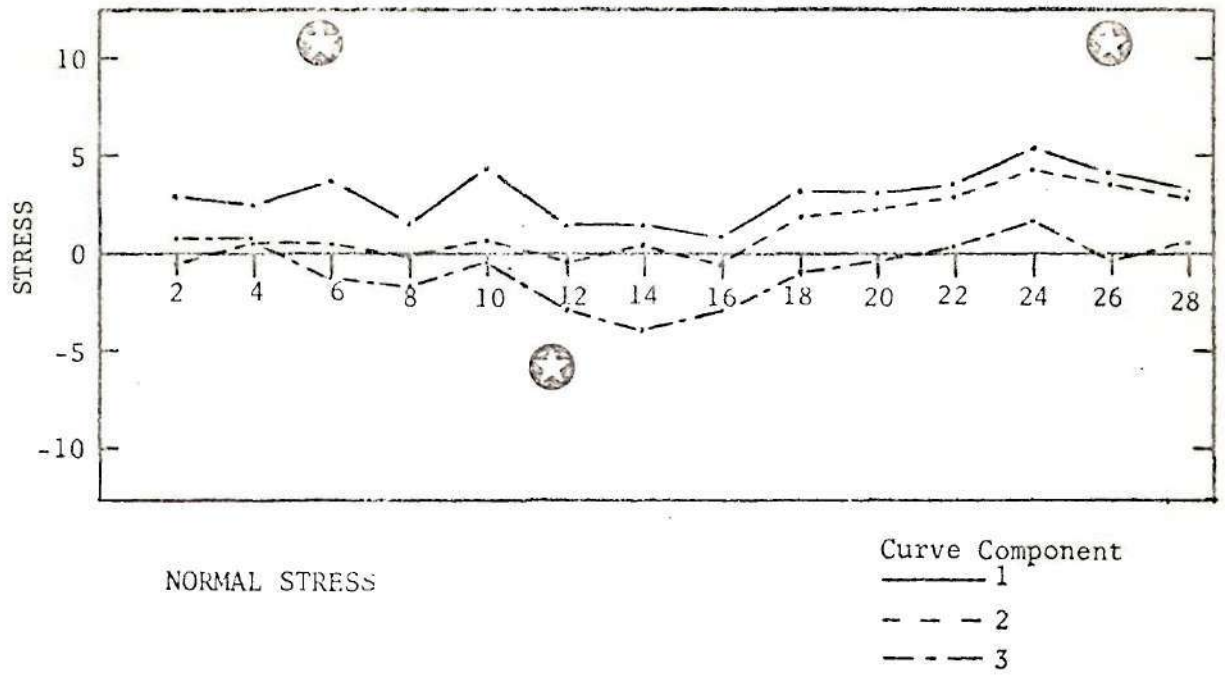

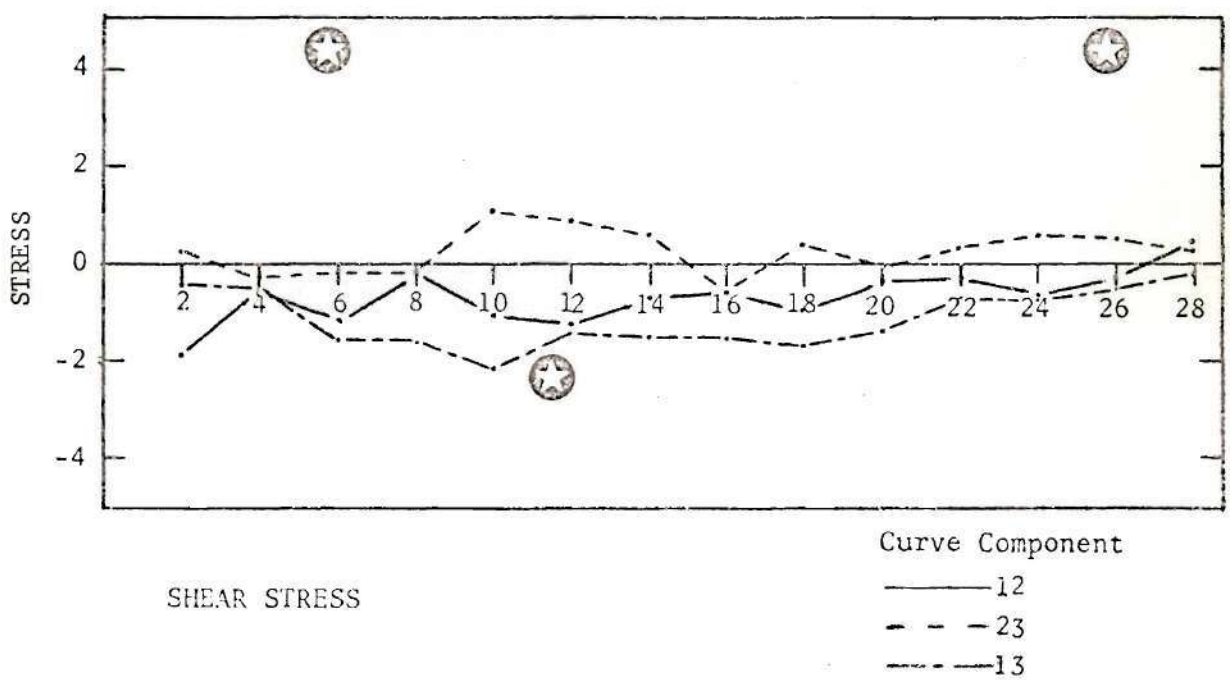

Figure 42. Normal and shear stress results for two-layer model for solution station (I') in 2 direction for J' (1 direction) = 16, K = 1.

Refer to explanation preceding Fig. 14 and to Figs. 2 and 13.

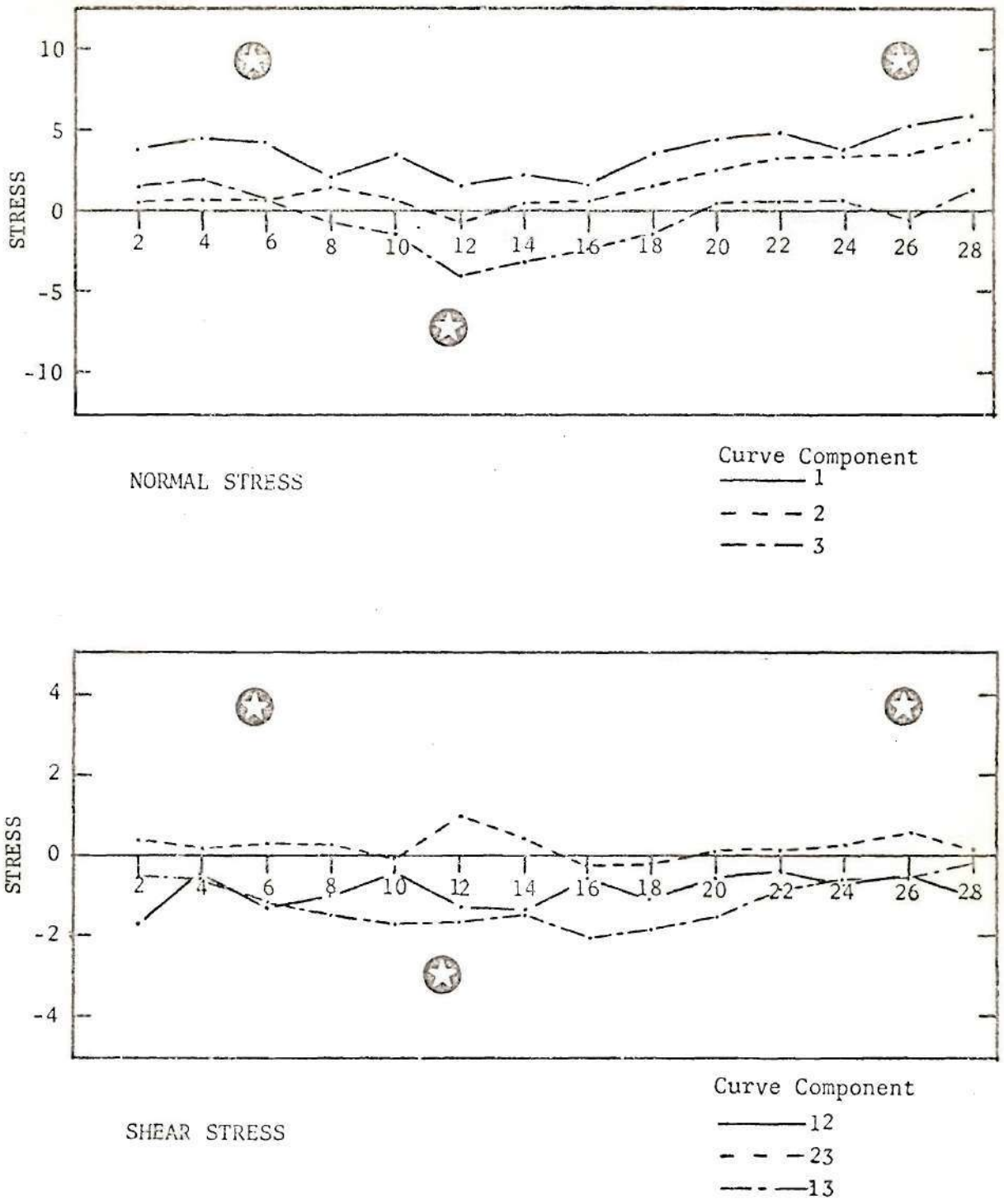

Figure 43. Normal and shear stress results for two-layer model for solution station (I') in 2 direction for J' (1 direction) = 16, K = 2.

Refer to explanation preceding Fig. 14 and to Figs. 2 and 13.

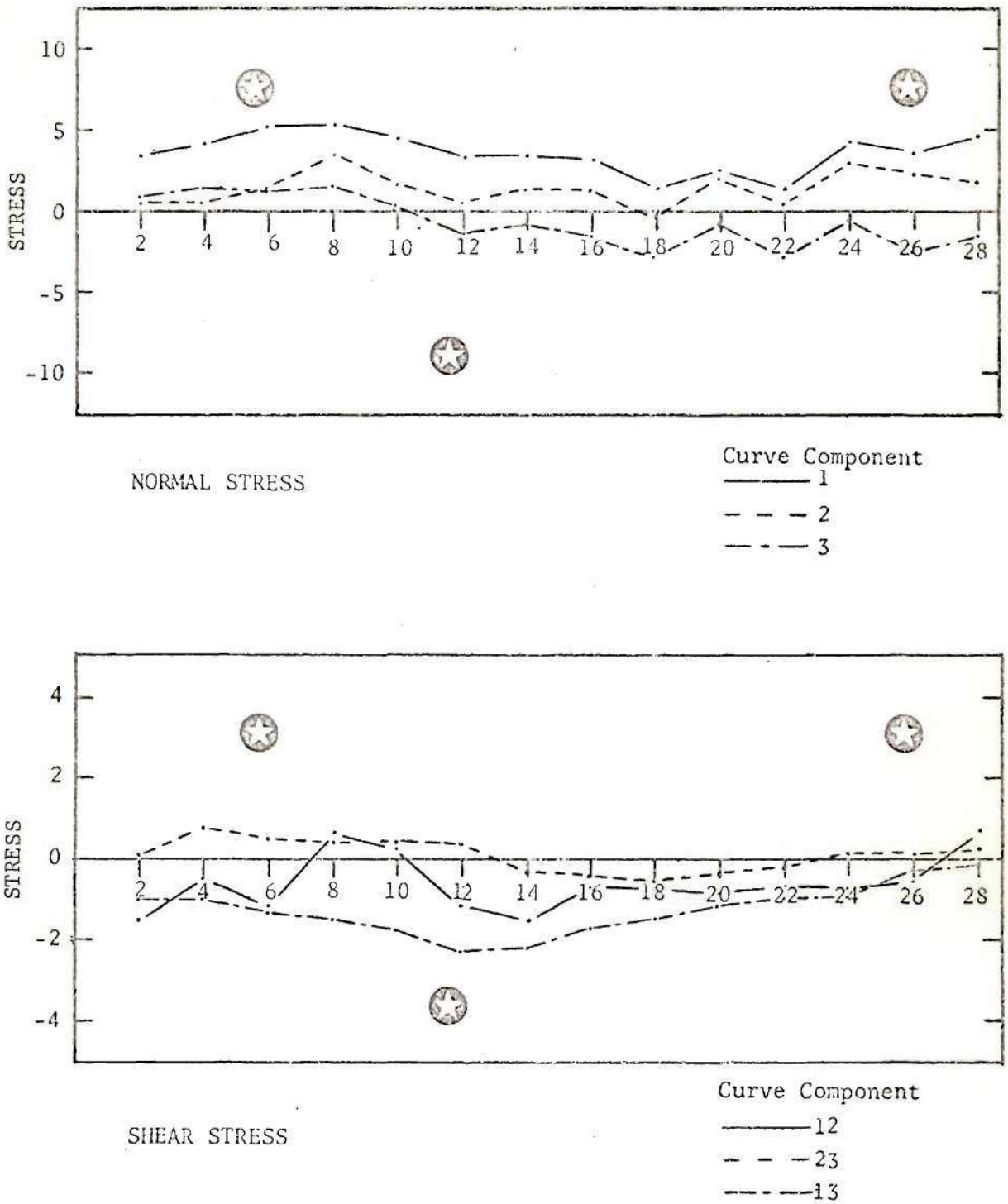

Figure 44. Normal and shear stress results for two-layer model for solution station (I') in 2 direction for J' (1 direction) = 16, K = 3.

Refer to explanation preceding Fig. 14 and to Figs. 2 and 13.

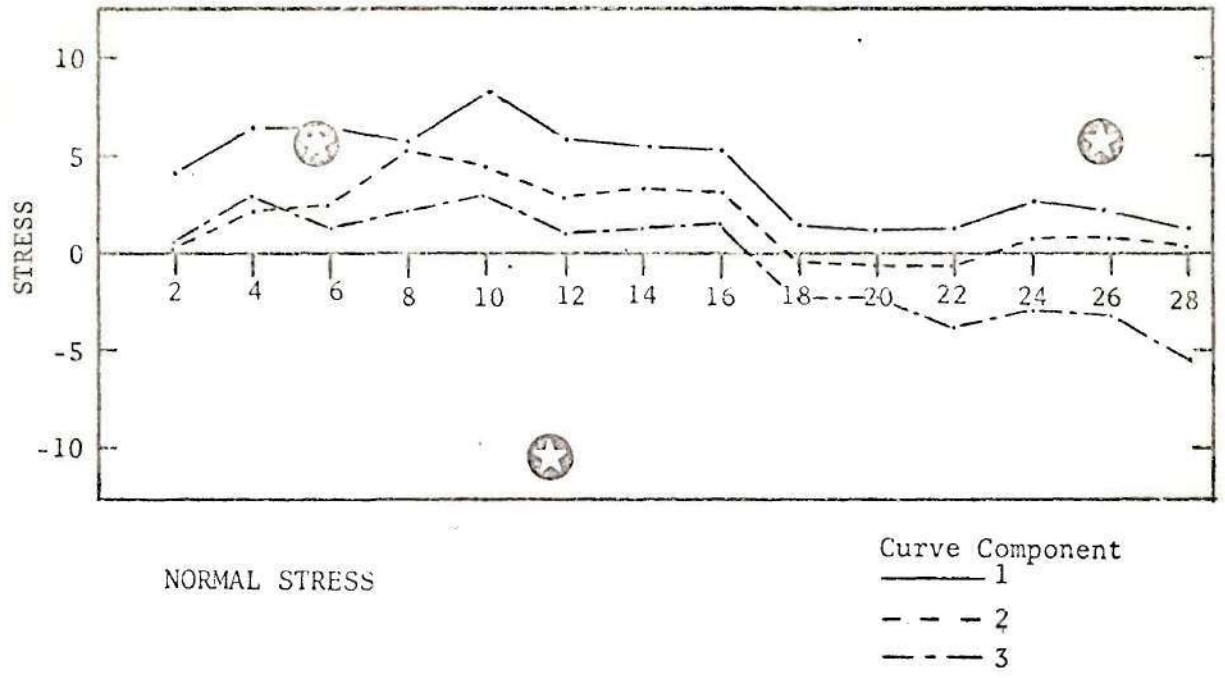

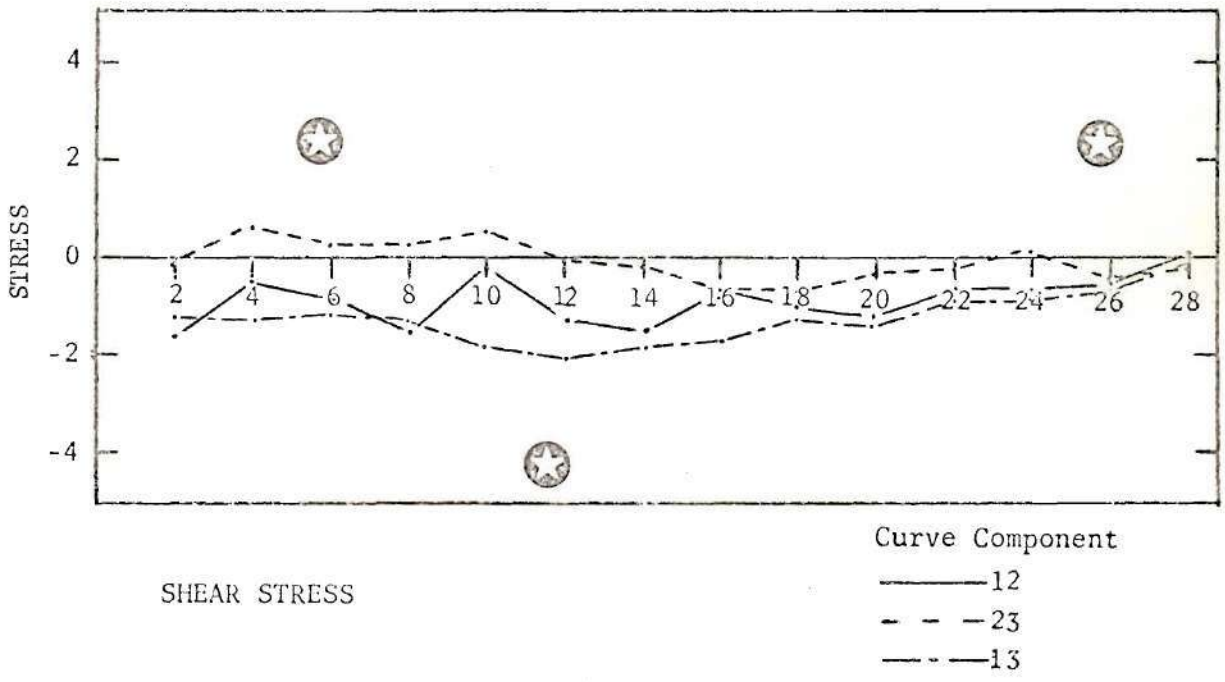

Figure 45. Normal and shear stress results for two-layer model for solution station (I') in 2 direction for J' (1 direction) = 16, K = 4.

Refer to explanation preceding Fig. 14 and to Figs. 2 and 13.

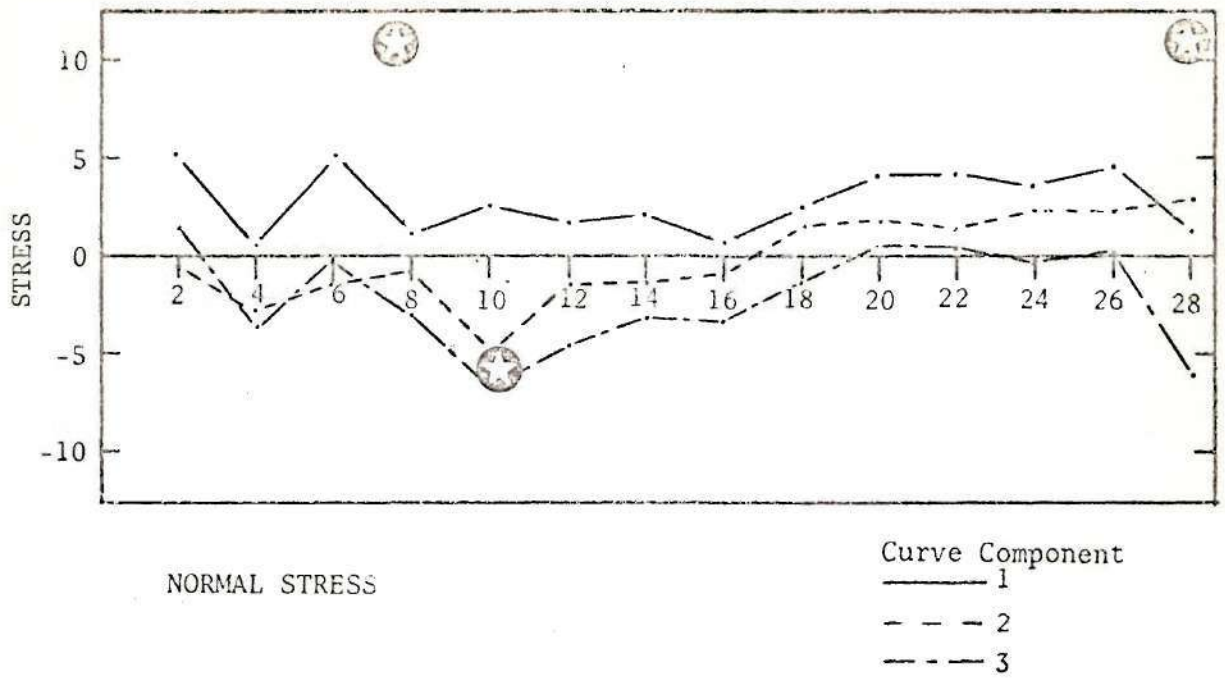

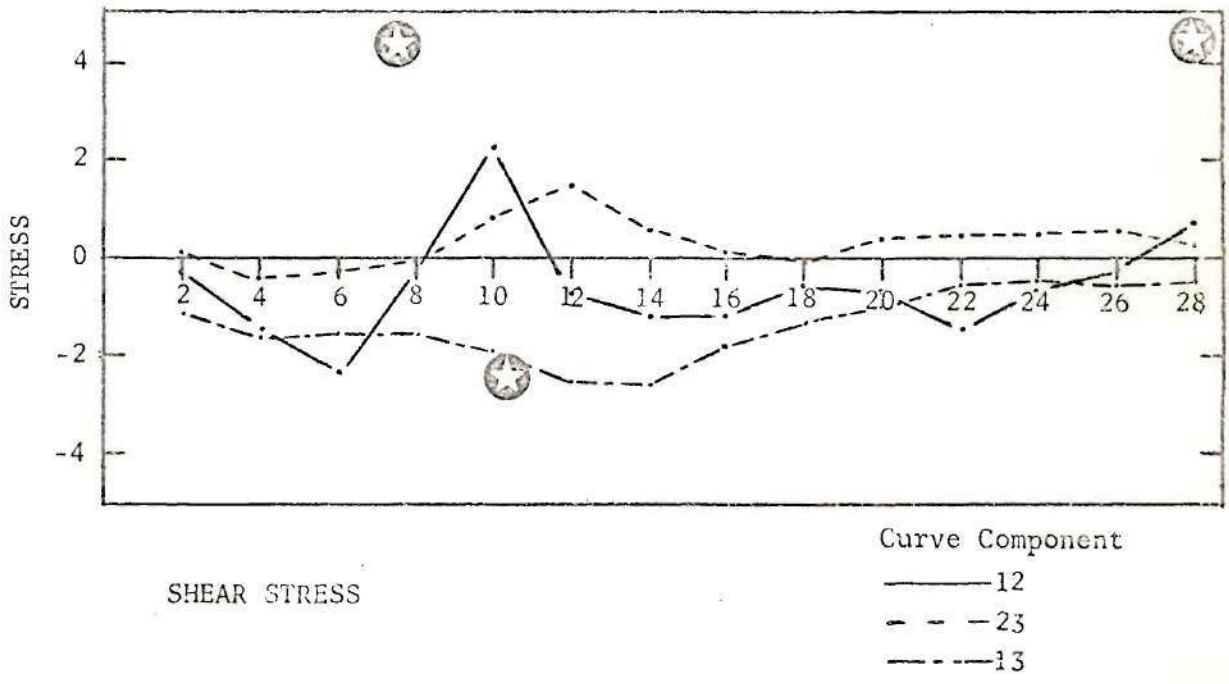

Figure 46. Normal and shear stress results for two-layer model for solution station (I') in 2 direction for J' (1 direction) = 18, K = 1.

Refer to explanation preceding Fig. 14 and to Figs. 2 and 13.

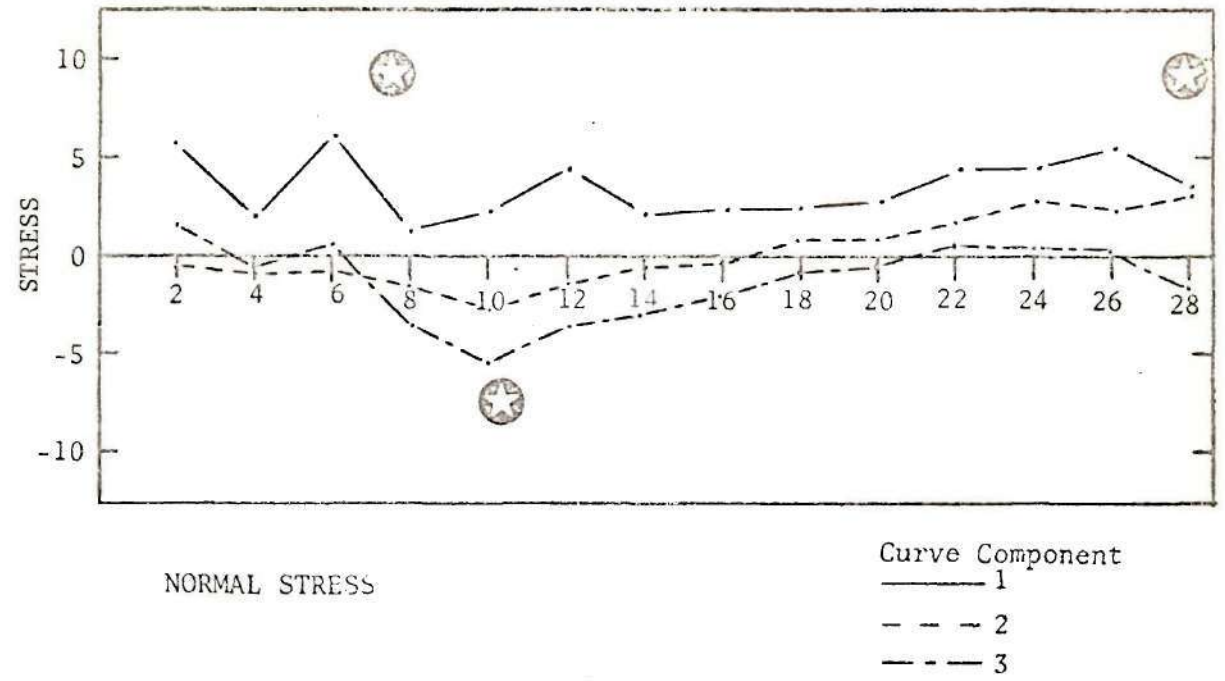

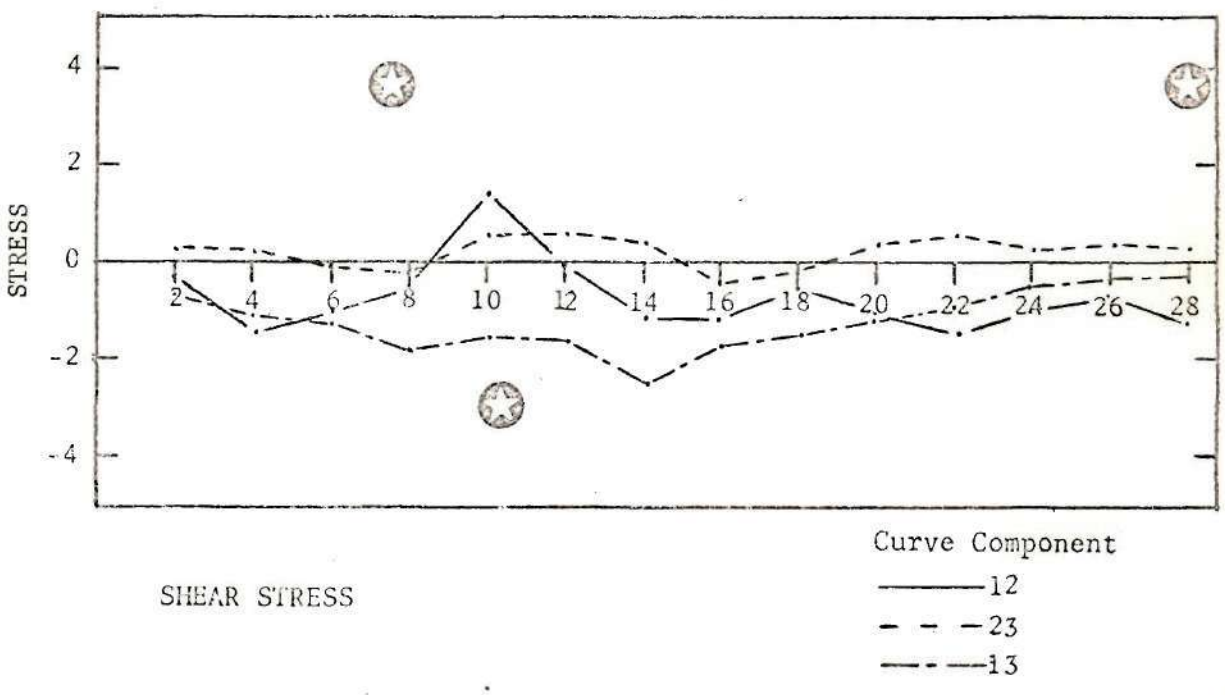

Figure 47. Normal and shear stress results for two-layer model for solution station (I') in 2 direction for J' (1 direction) = 18, K = 2.

Refer to explanation preceding Fig. 14 and to Figs. 2 and 13.

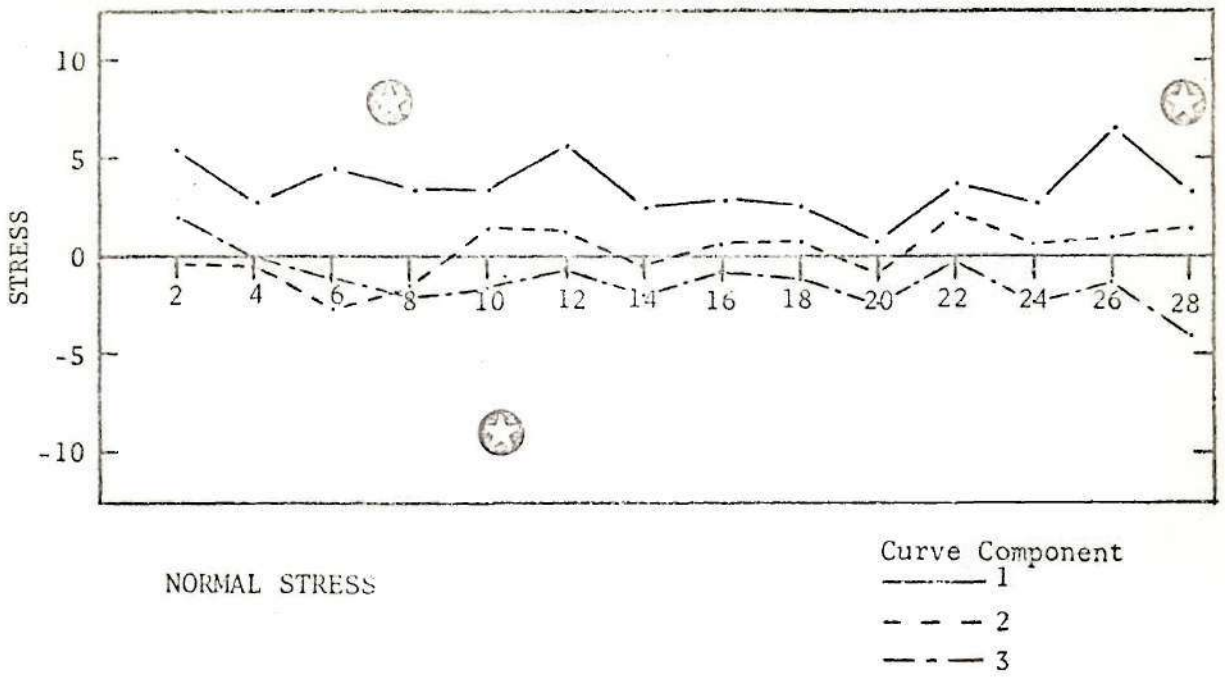

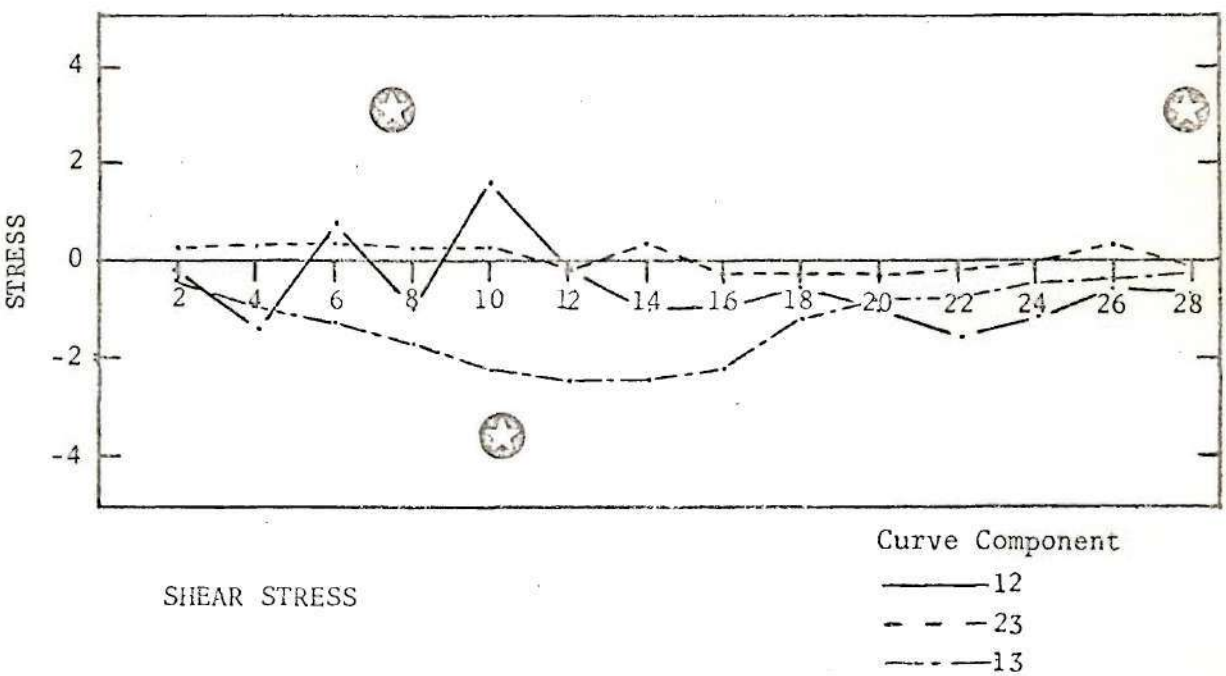

Figure 48. Normal and shear stress results for two-layer model for solution station (I') in 2 direction for J' (1 direction) = 18, K = 3.

Refer to explanation preceding Fig. 14 and to Figs. 2 and 13.

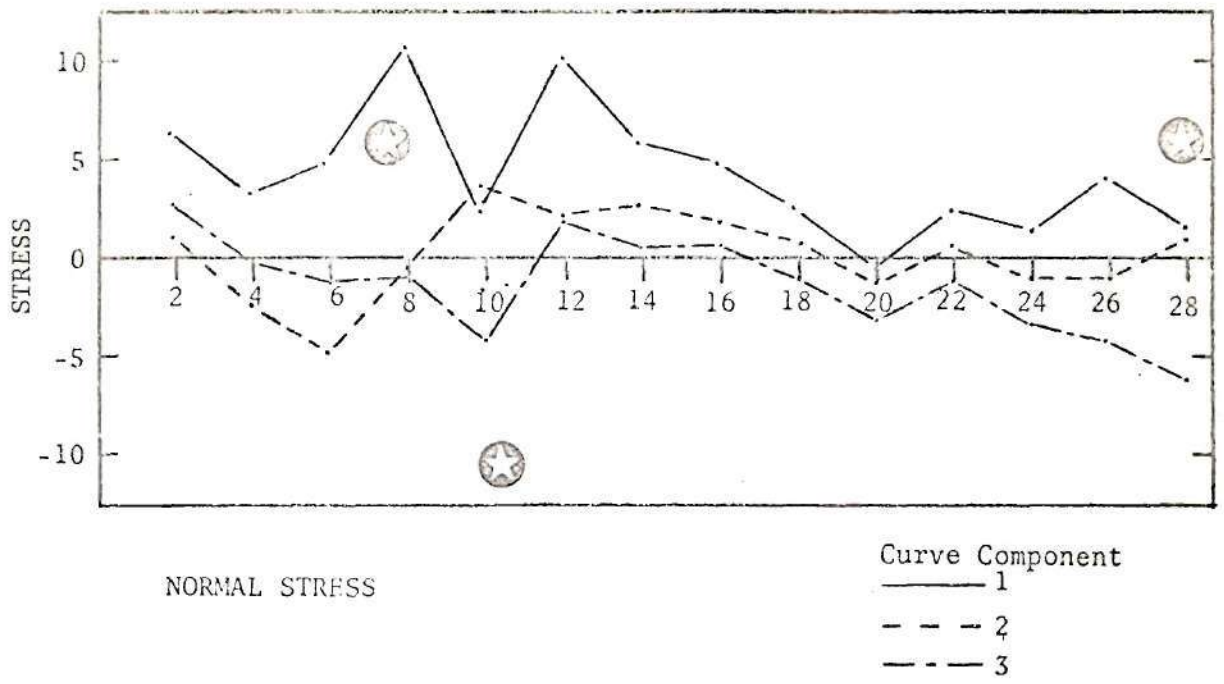

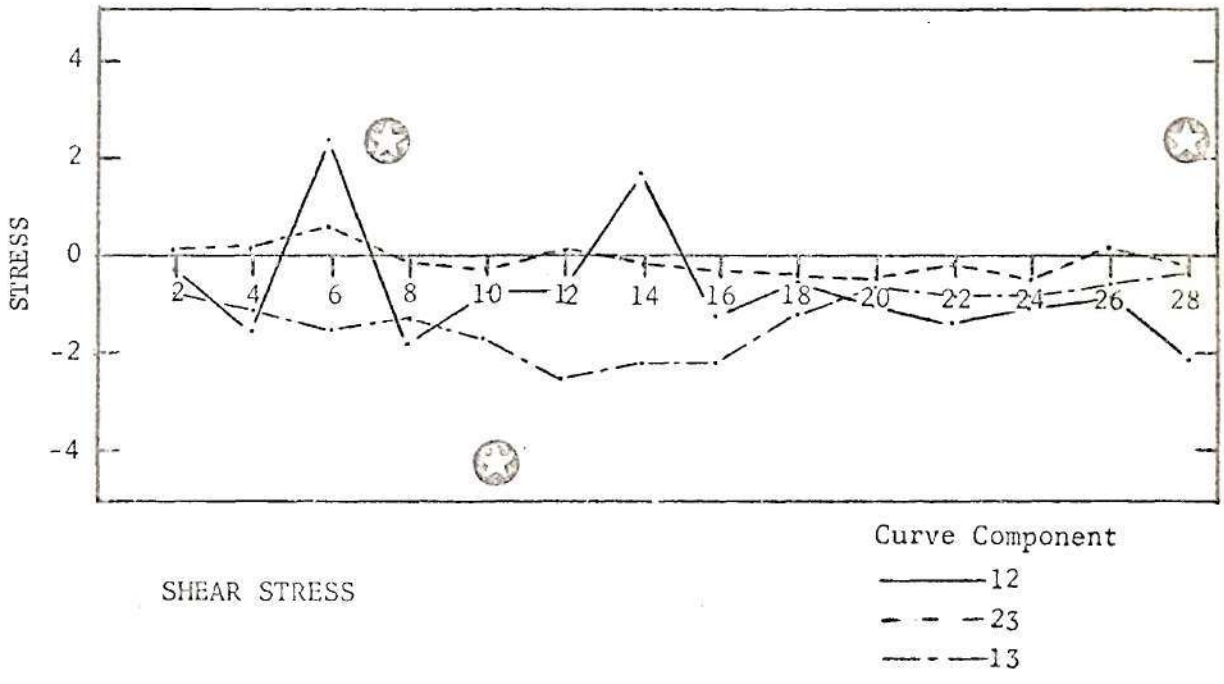

Figure 49. Normal and shear stress results for two-layer model for solution station (I') in 2 direction for J' (1 direction) = 18, K = 4.

Refer to explanation preceding Fig. 14 and to Figs. 2 and 13.

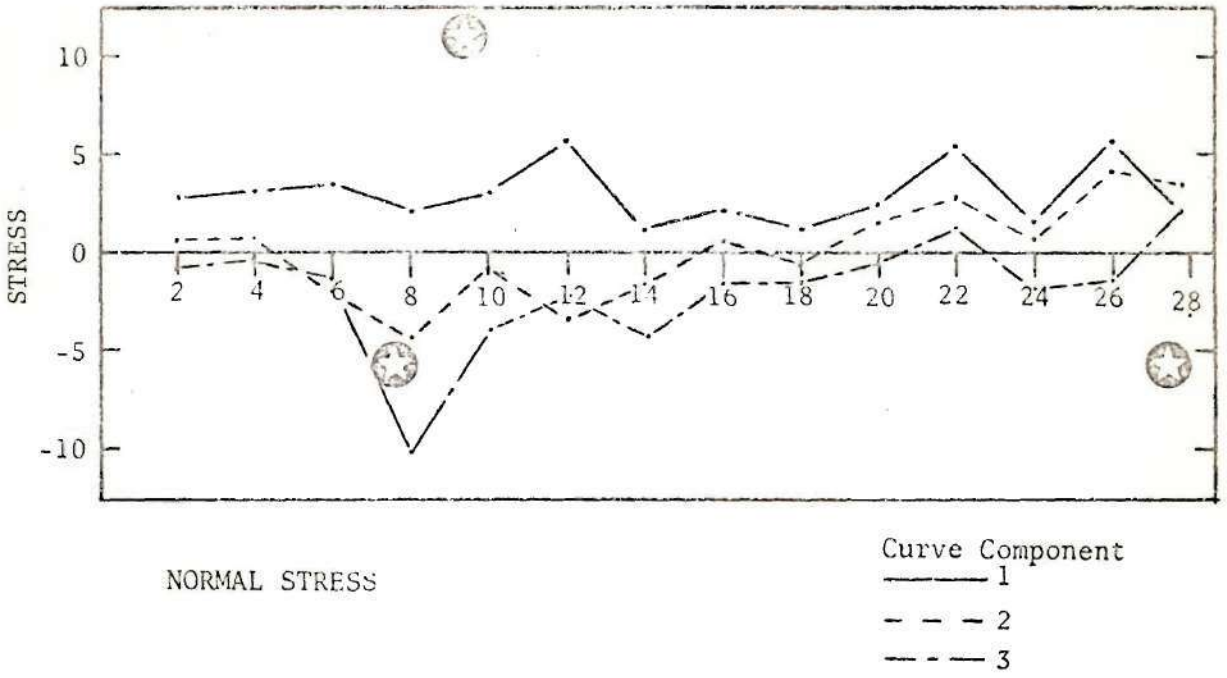

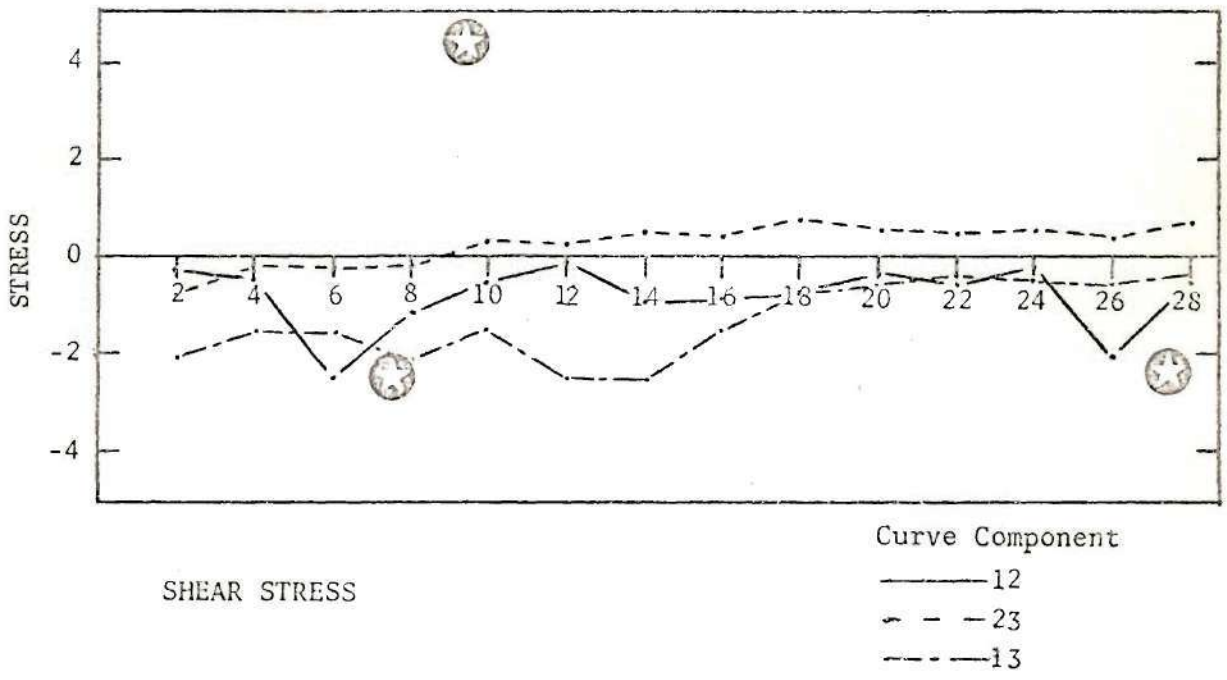

Figure 50. Normal and shear stress results for two-layer model for solution station (I') in 2 direction for J' (1 direction) = 20, K = 1.

Refer to explanation preceding Fig. 14 and to Figs. 2 and 13.

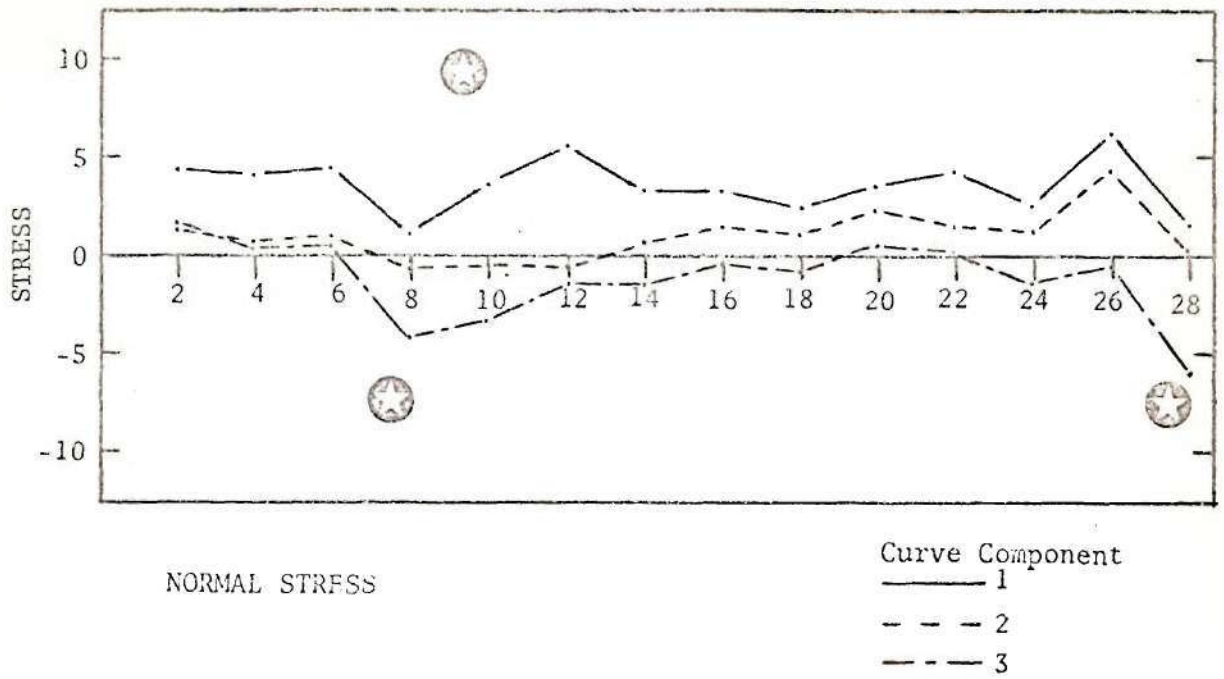

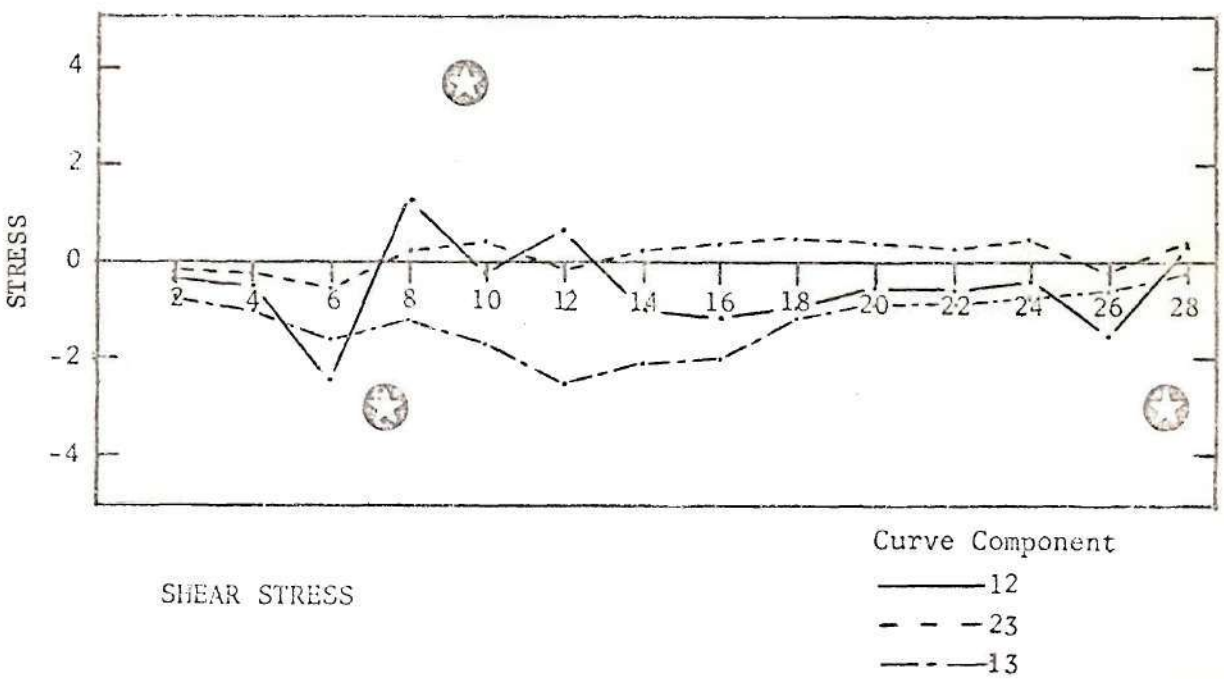

Figure 51. Normal and shear stress results for two-layer model for solution station (I') in 2 direction for J' (1 direction) = 20, K = 2.

Refer to explanation preceding Fig. 14 and to Fgis. 2 and 13.

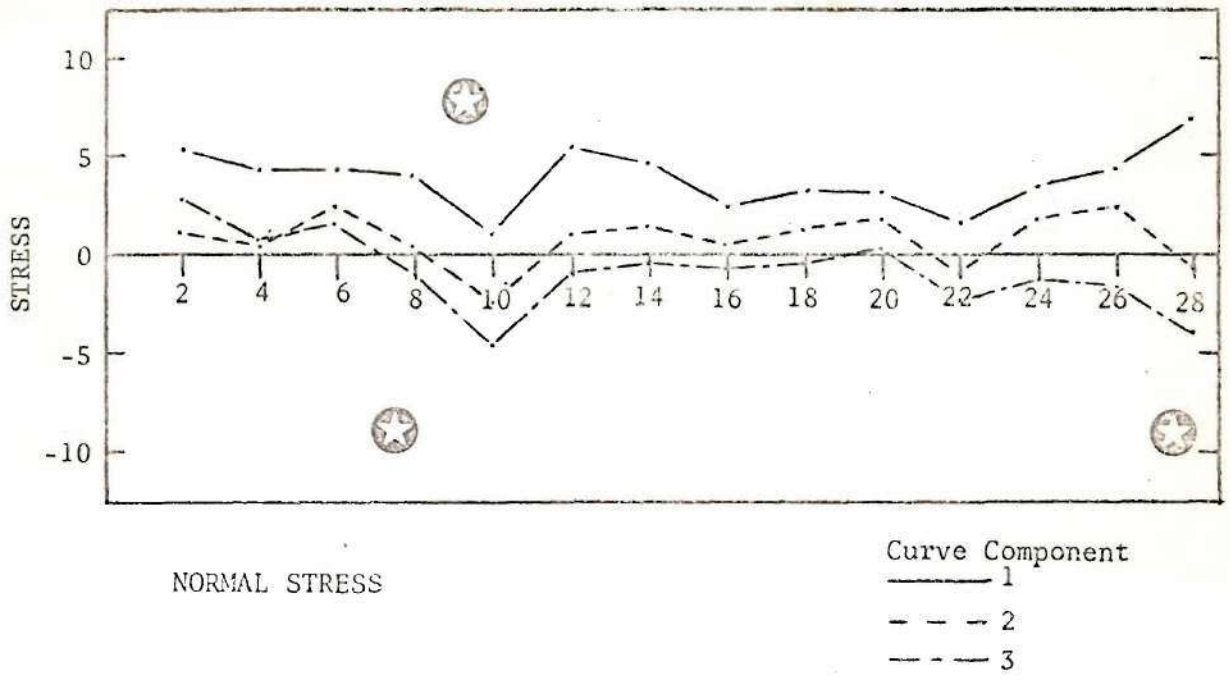

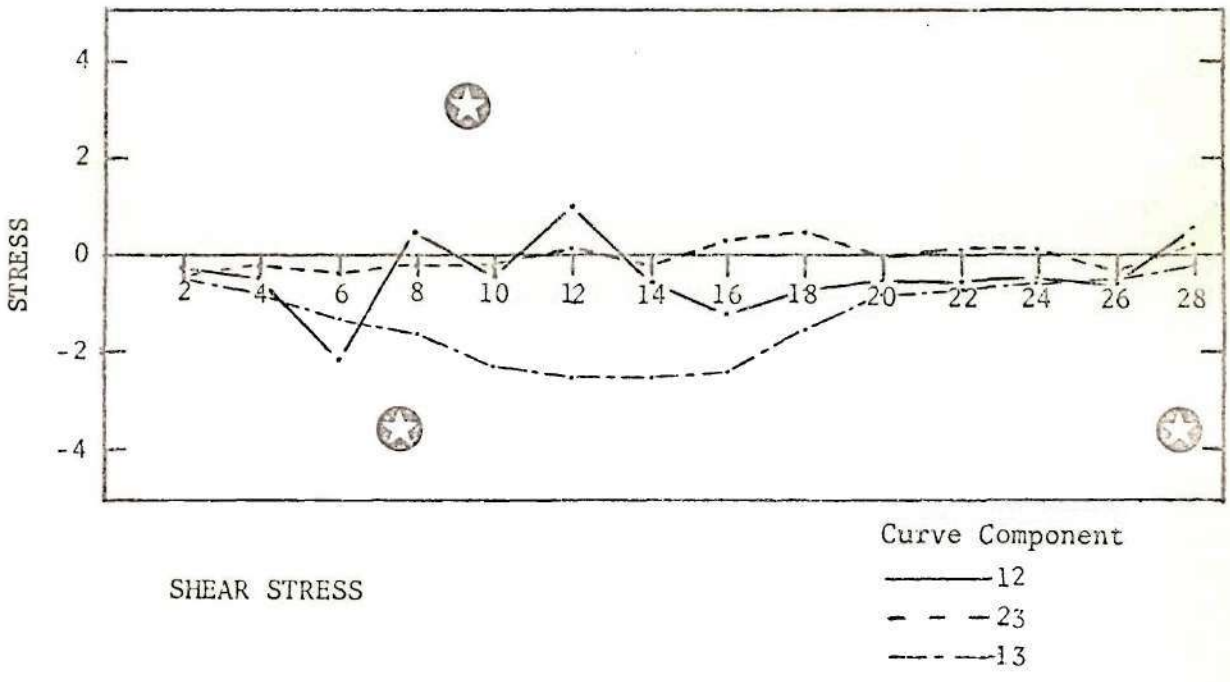

Figure 52. Normal and shear stress results for two-layer model for solution station (I') in 2 direction for J' (1 direction = 20, K = 3.

Refer to explanation preceding Fig. 14 and to Figs. 2 and 13.

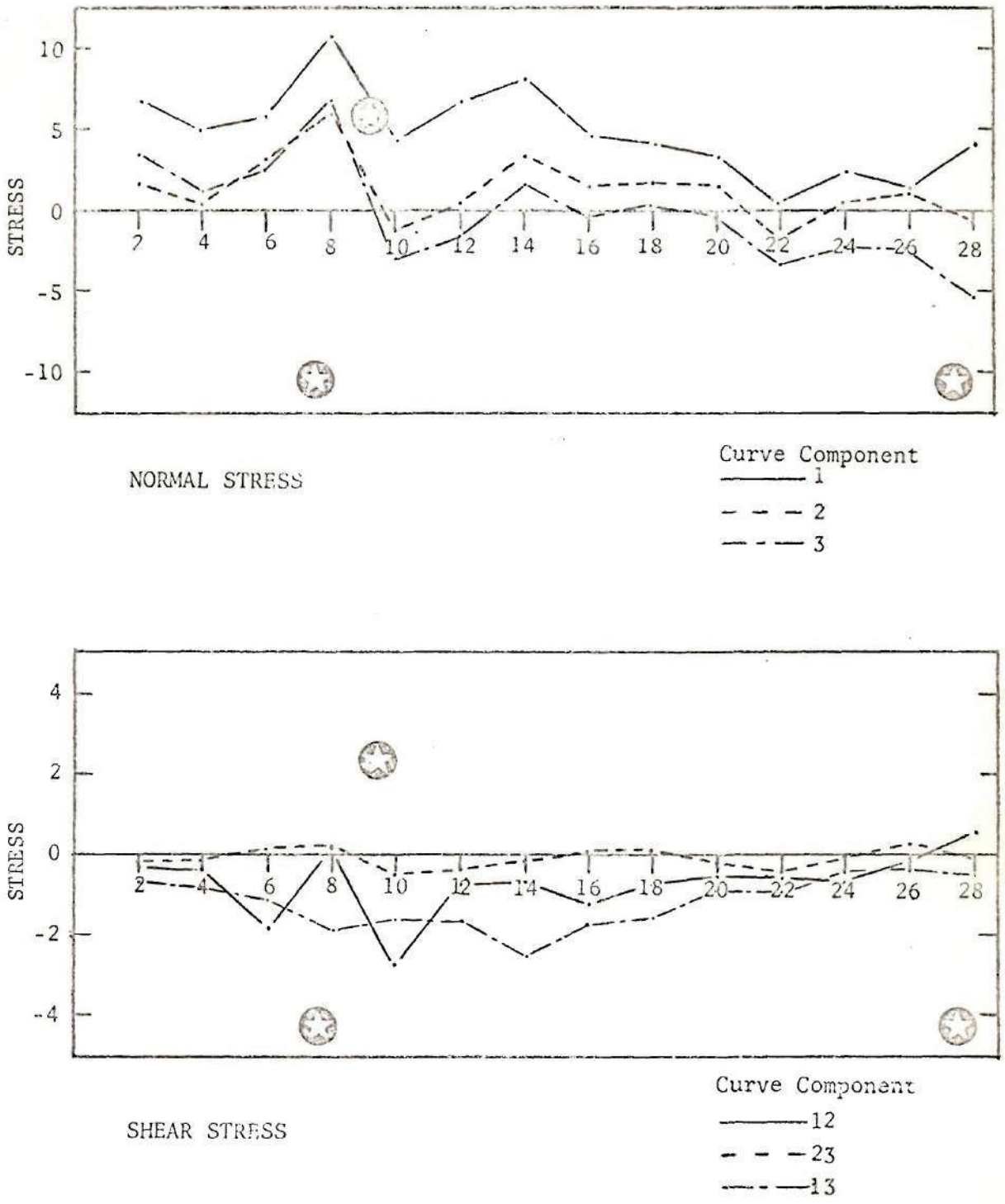

Figure 53. Normal and shear stress results for two-layer model for solution station (I') in 2 direction for J' (1 direction) = 20, K = 4.

Refer to explanation preceding Fig. 14 and to Figs. 2 and 13.

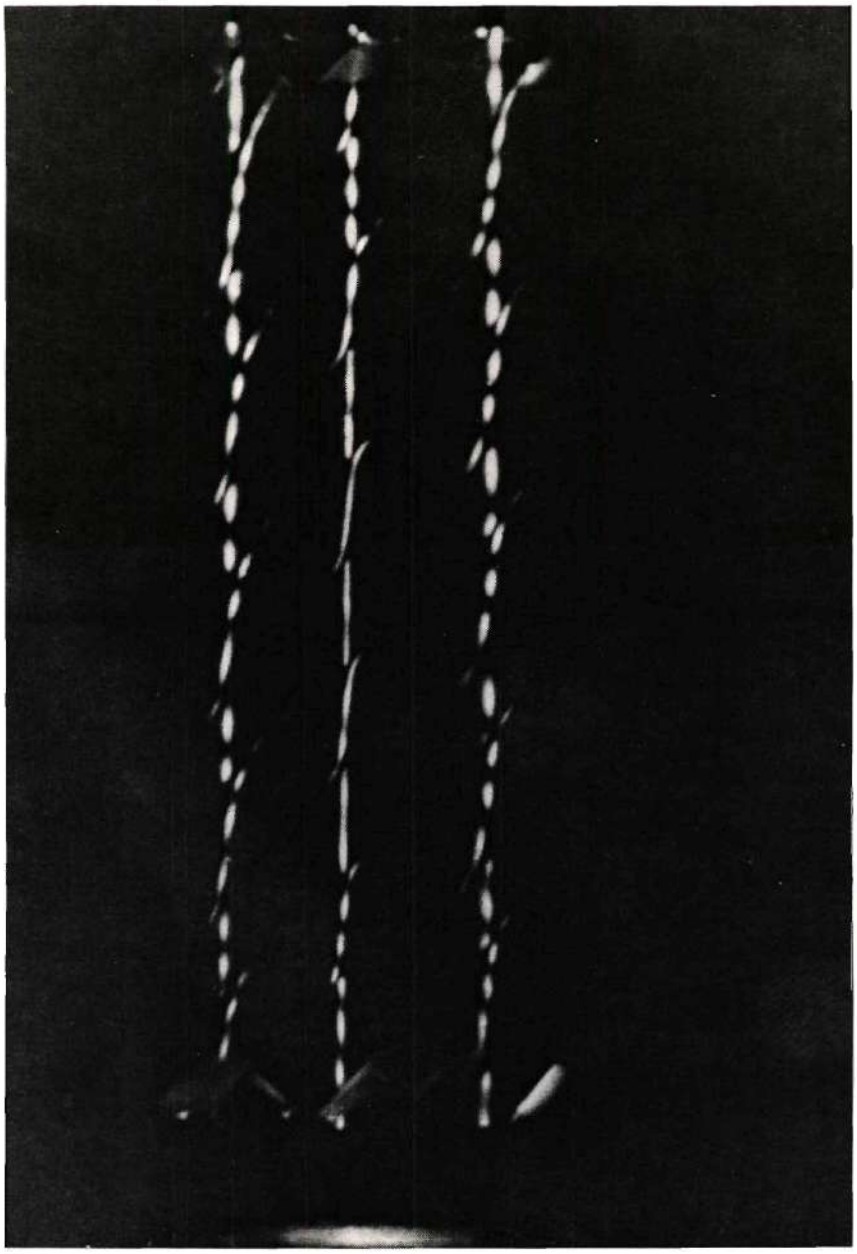

Figure 54. Fringe Traces for z = -0.30, Plane 1, four-layer model. Light beam enters at top. Traces are 3.63 in. long. Observation directions are 45° apart (cw, viewed from bottom and left to right)

Graphs of Stresses in Four-Layer Model

The following graphs (Figures 55-69) give values of the inter-laminar shear stress τ_{yz} where τ_{yz} again has been normalized (divided by the average axial stress). The three curves are for stresses along the three line segments in the appropriate xy plane. The value of y for this xy plane and plane identifying position between fiber layers is given with each curve.

Below the stress curves, the ellipses shown are approximate scale representations of the fiber intersections at their appropriate locations in the particular xy plane. The three lines between the rows of ellipses indicate the location of the planes of examination 1,2,3, proceeding from plane 1 (lowest) to plane 3 with spacings 0.05 in. Plane 2 is midway between the fiber layers (Figure 4).

The distance x is in inches proceeding from the free boundary at $x = 0$. The model was 3.63 inches wide.

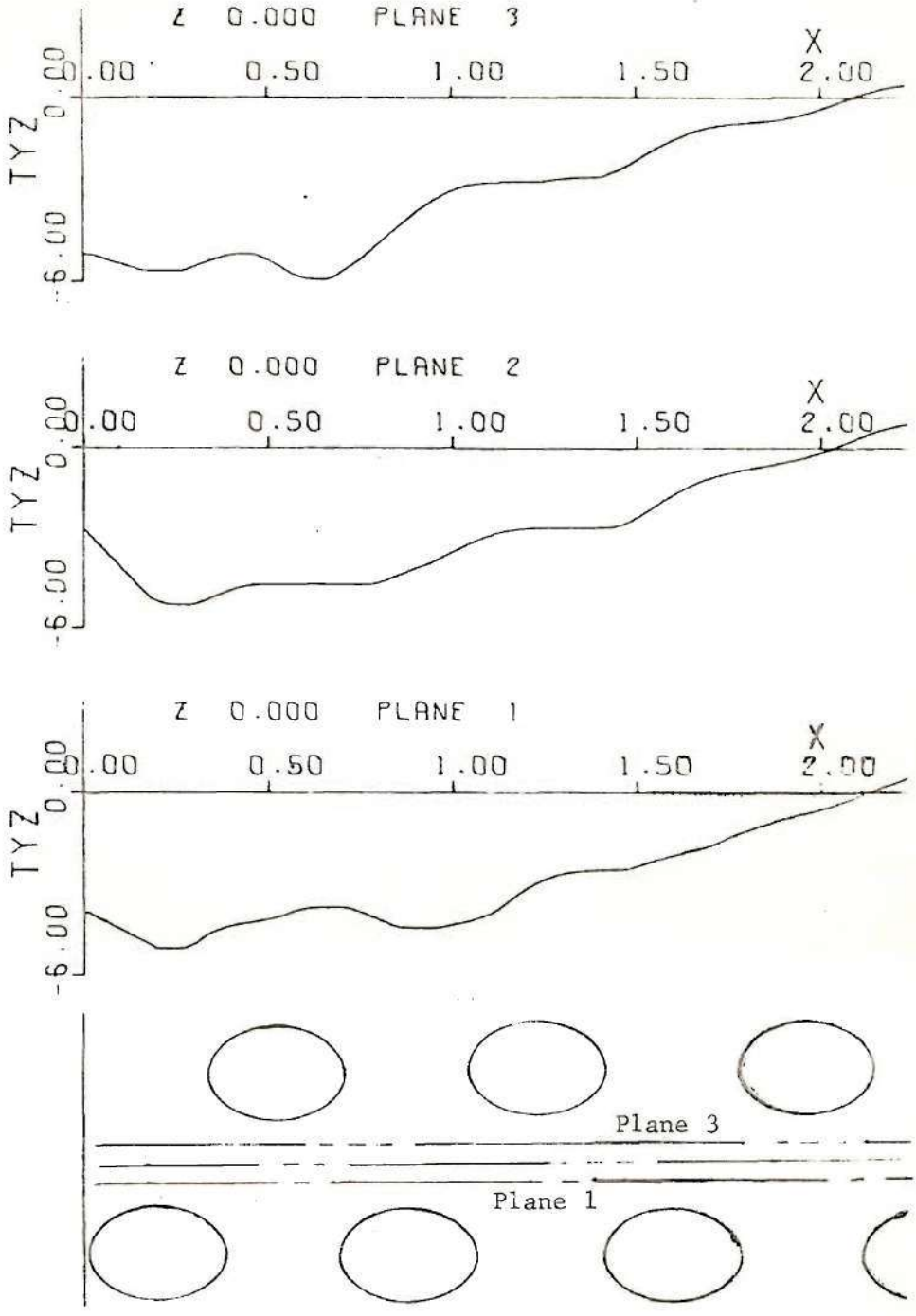

55. Interlaminar shear stress τ_{yz} for four-layer model for planes and z location given. Plane locations and fiber intersections for z locations are given also. Refer to explanation preceding Fig. 55 and to Fig. 5.

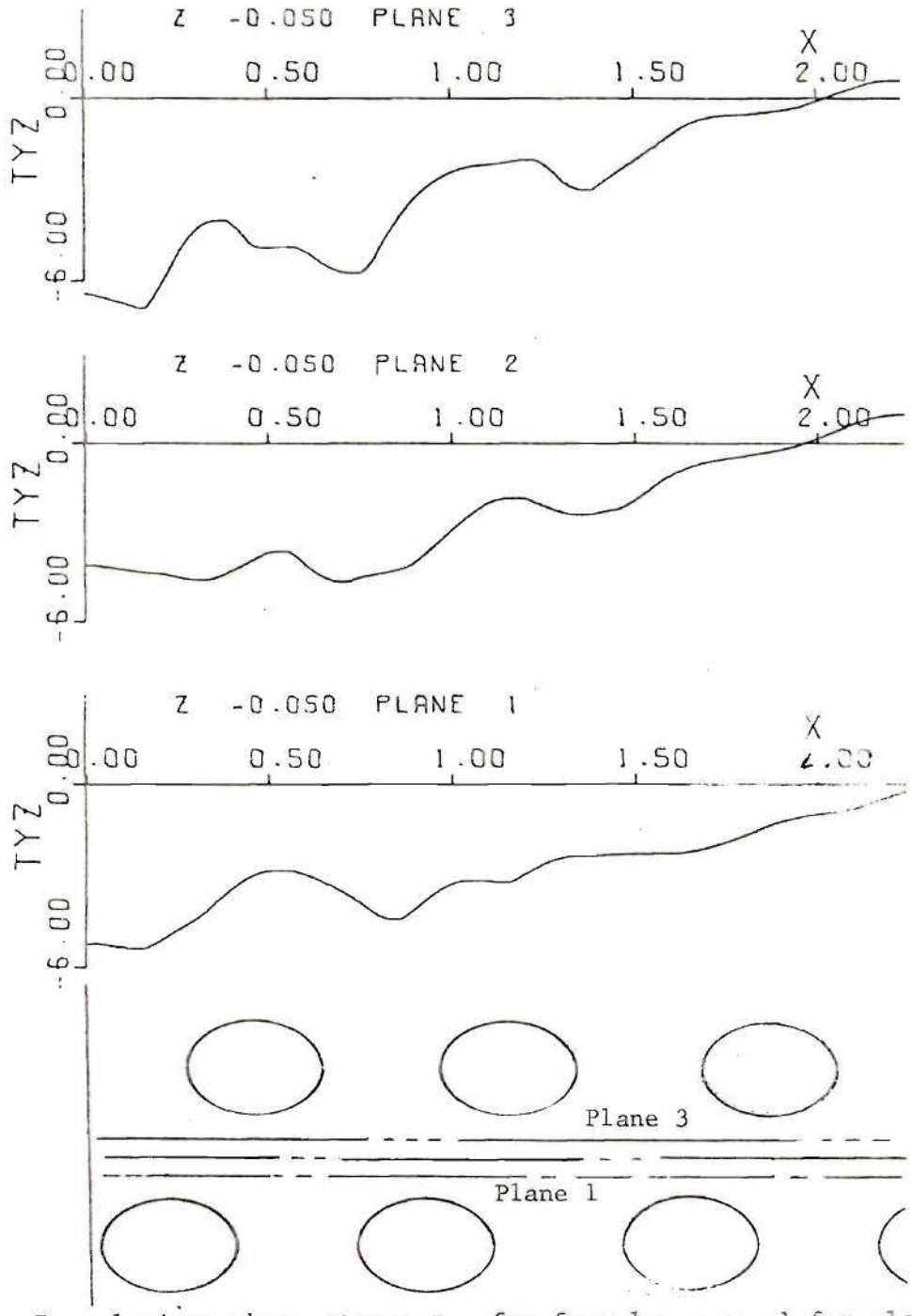

56. Interlaminar shear stress τ_{yz} for four-layer model for planes and z location given. Plane locations and fiber intersections for z locations are given also. Refer to explanation preceding Fig. 55 and to Fig. 5.

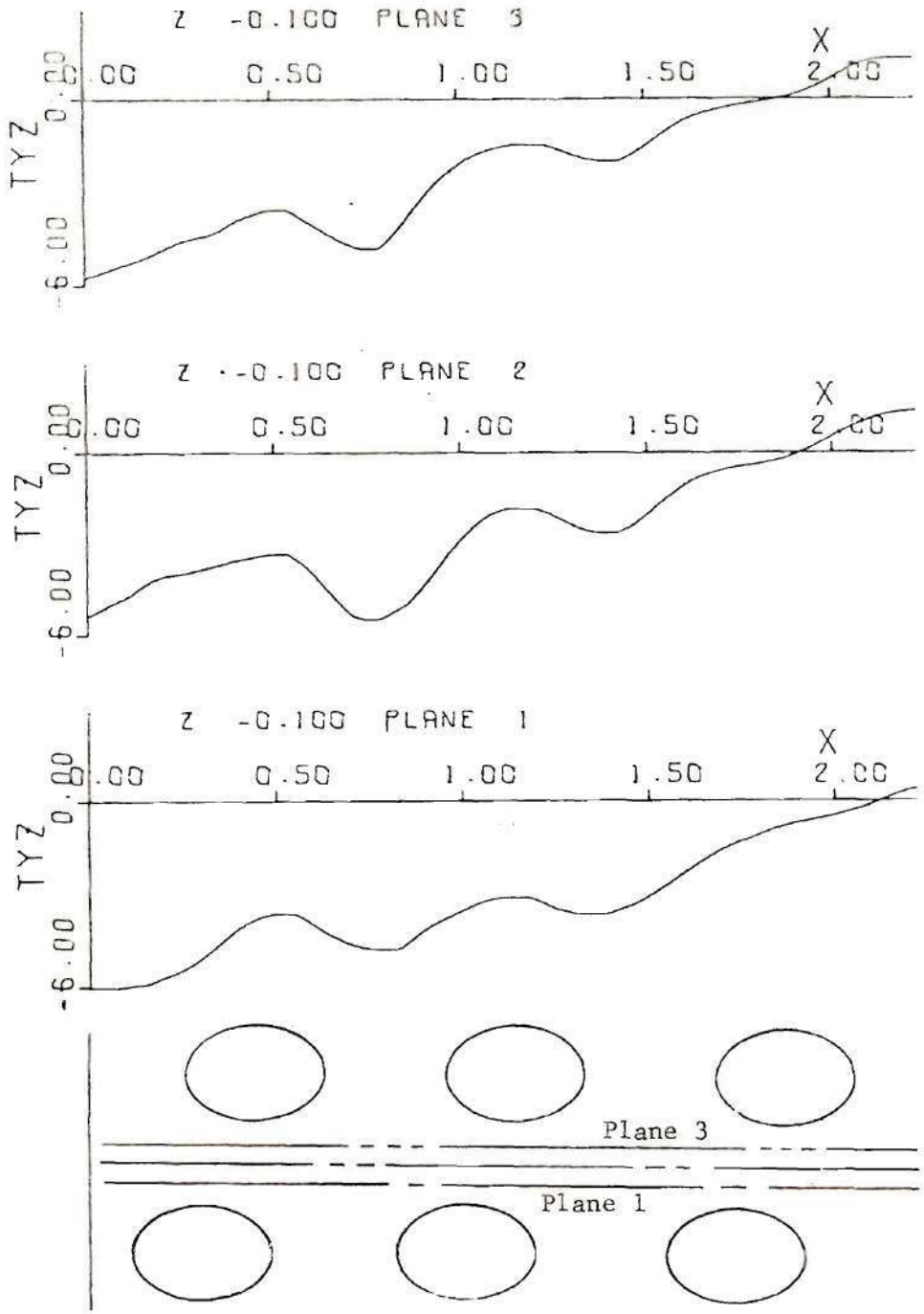

57. Interlaminar shear stress τ_{yz} for four-layer model for planes and z location given. Plane locations and fiber intersections for z locations are given also. Refer to explanation preceding Fig. 55 and to Fig. 5.

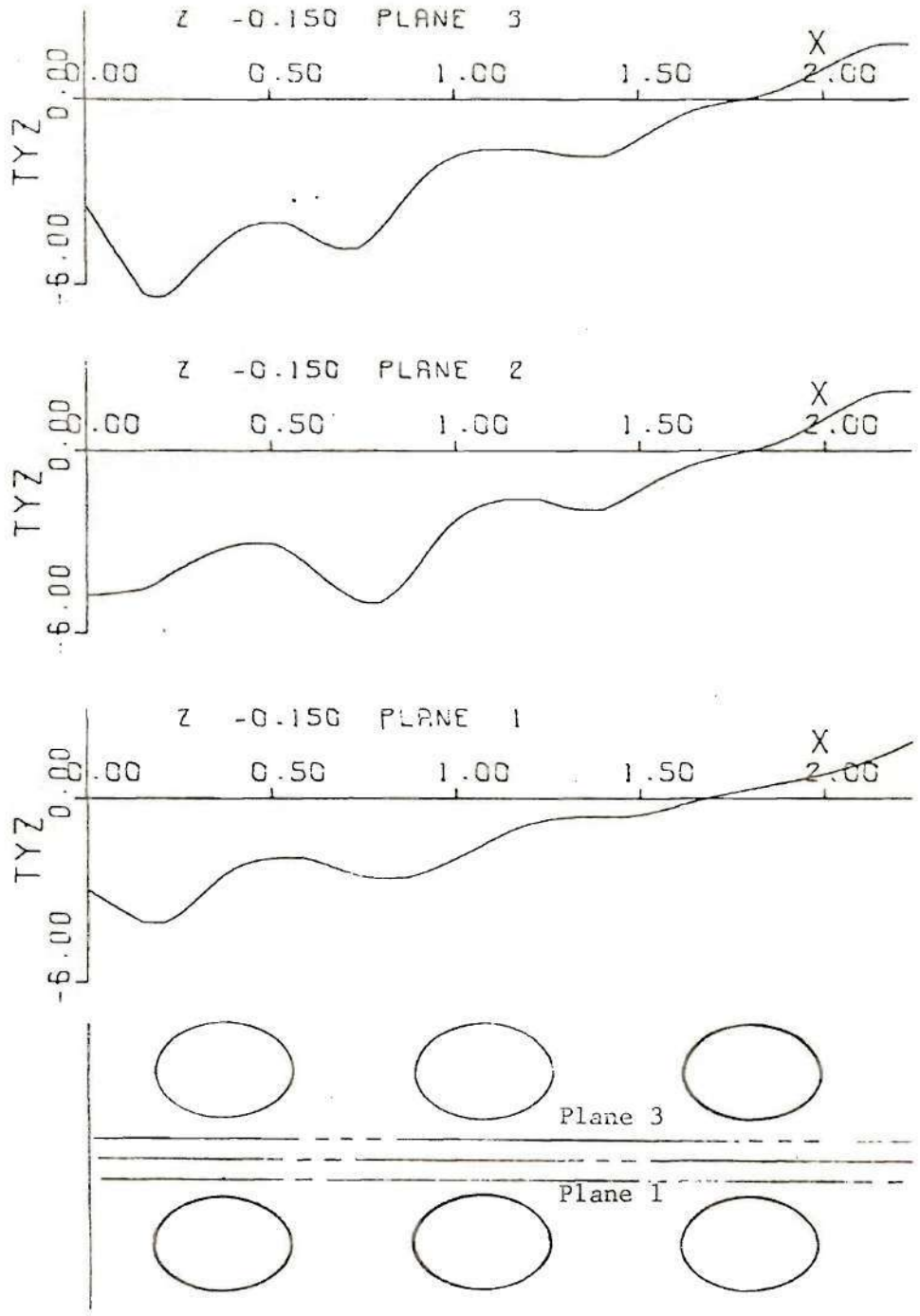

58. Interlaminar shear stress τ_{yz} for four-layer model for planes and z location given. Plane locations and fiber intersections for z locations are given also. Refer to explanation preceding Fig. 55 and to Fig. 5.

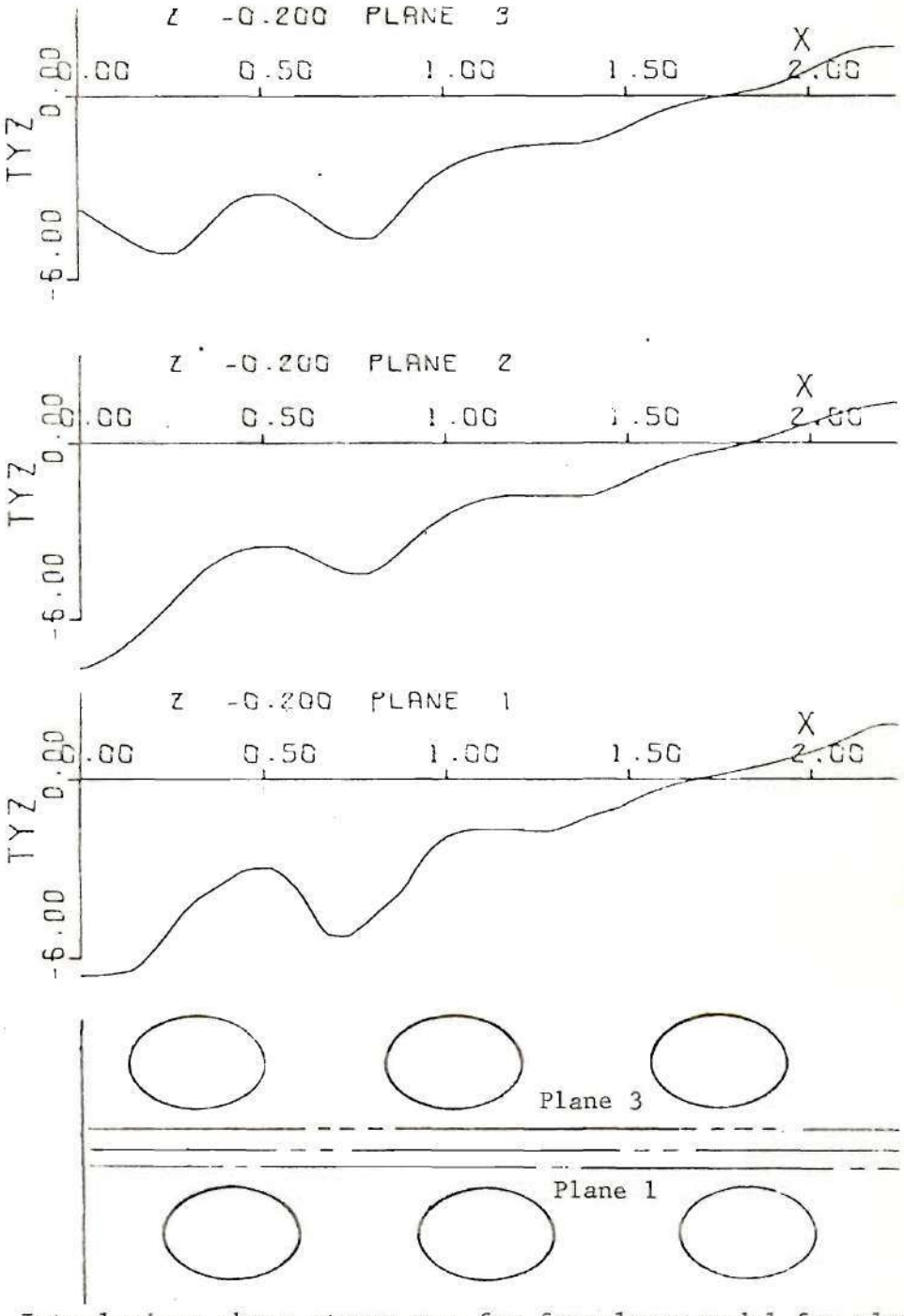

59. Interlaminar shear stress τ_{yz} for four-layer model for planes and z location given. Plane locations and fiber intersections for z locations are given also. Refer to explanation preceding Fig. 55 and to Fig. 5.

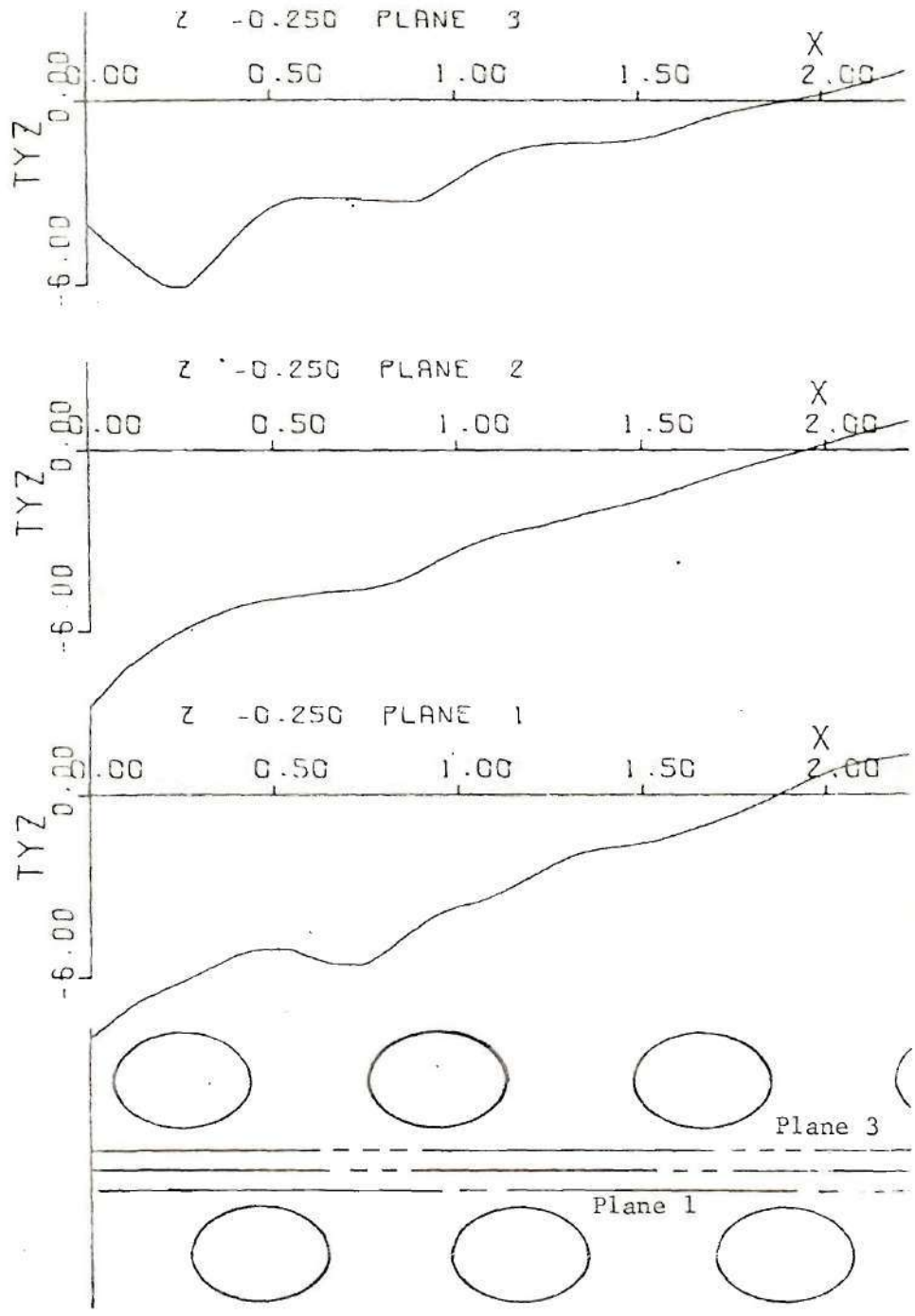

60. Interlaminar shear stress τ_{yz} for four-layer model for planes and z location given. Plane locations and fiber intersections for z locations are given also. Refer to explanation preceding Fig. 55 and to Fig. 5.

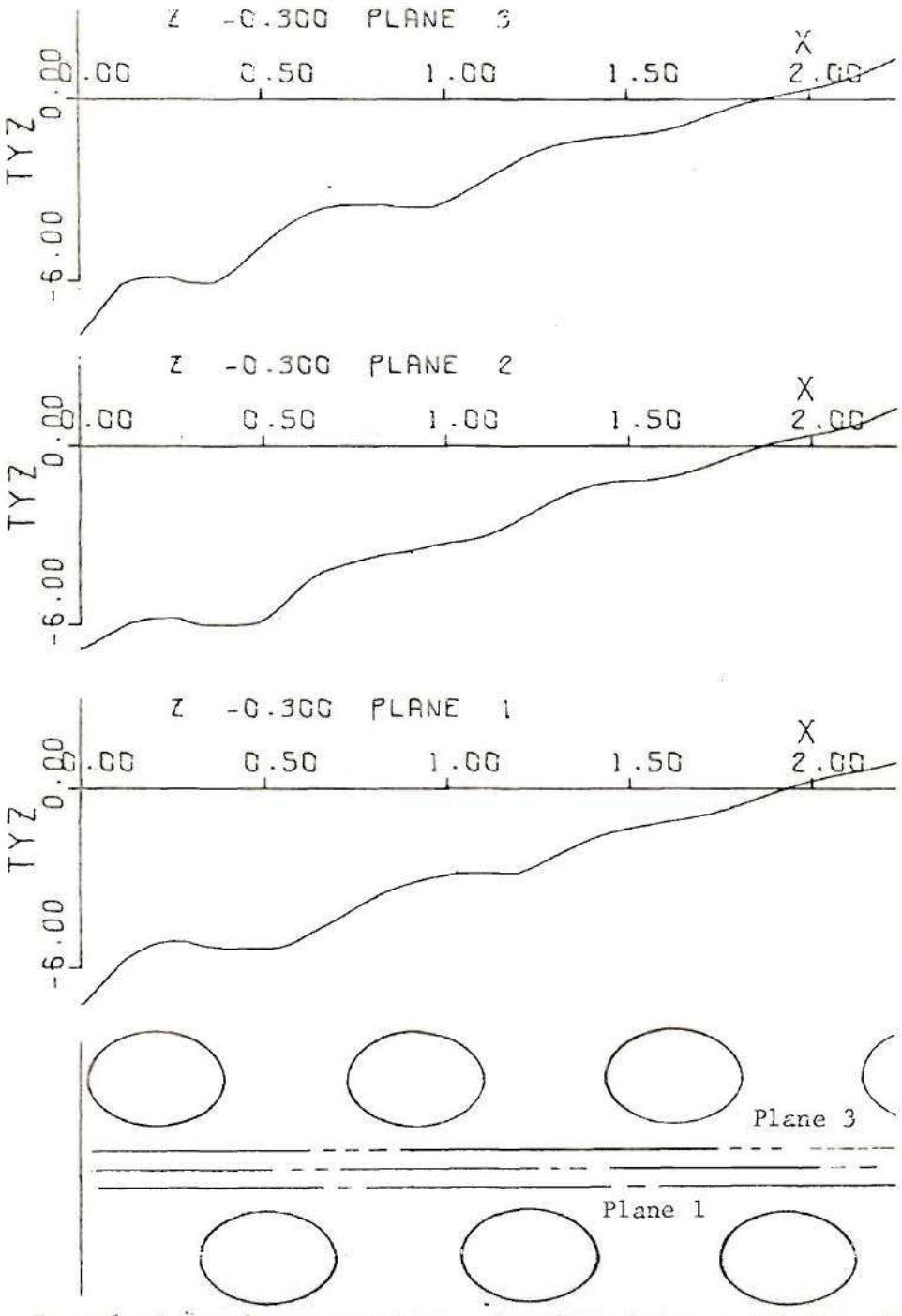

61. Interlaminar shear stress τ_{yz} for four-layer model for planes and z location given. Plane locations and fiber intersections for z locations are given also. Refer to explanation preceding Fig. 55 and to Fig. 5.

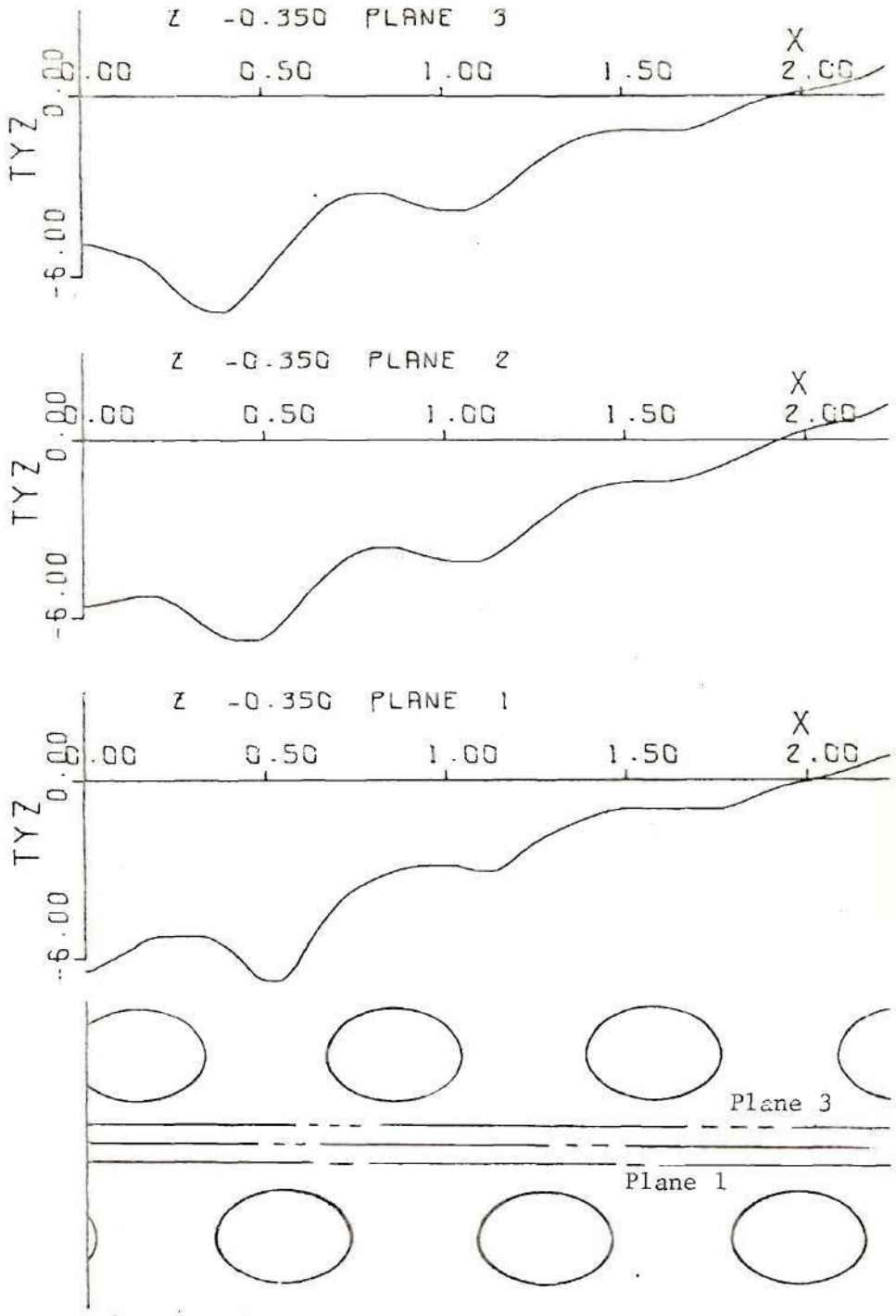

62. Interlaminar shear stress τ_{yz} for four-layer model for planes and z location given. Plane locations and fiber intersections for z locations are given also. Refer to explanation preceding Fig. 55 and to Fig. 5.

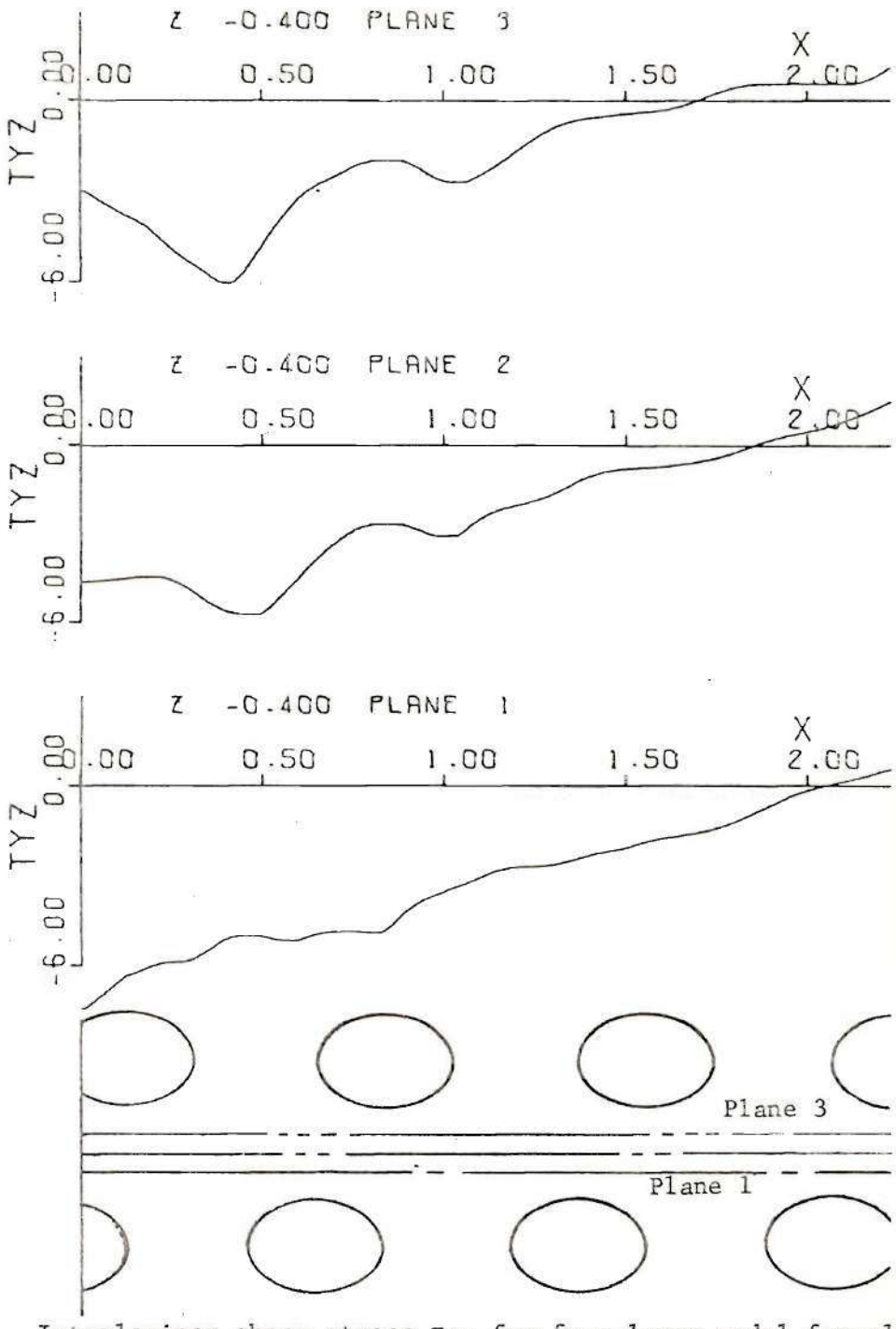

63. Interlaminar shear stress τ_{yz} for four-layer model for planes and z location given. Plane locations and fiber intersections for z locations are given also. Refer to explanation preceding Fig. 55 and to Fig. 5.

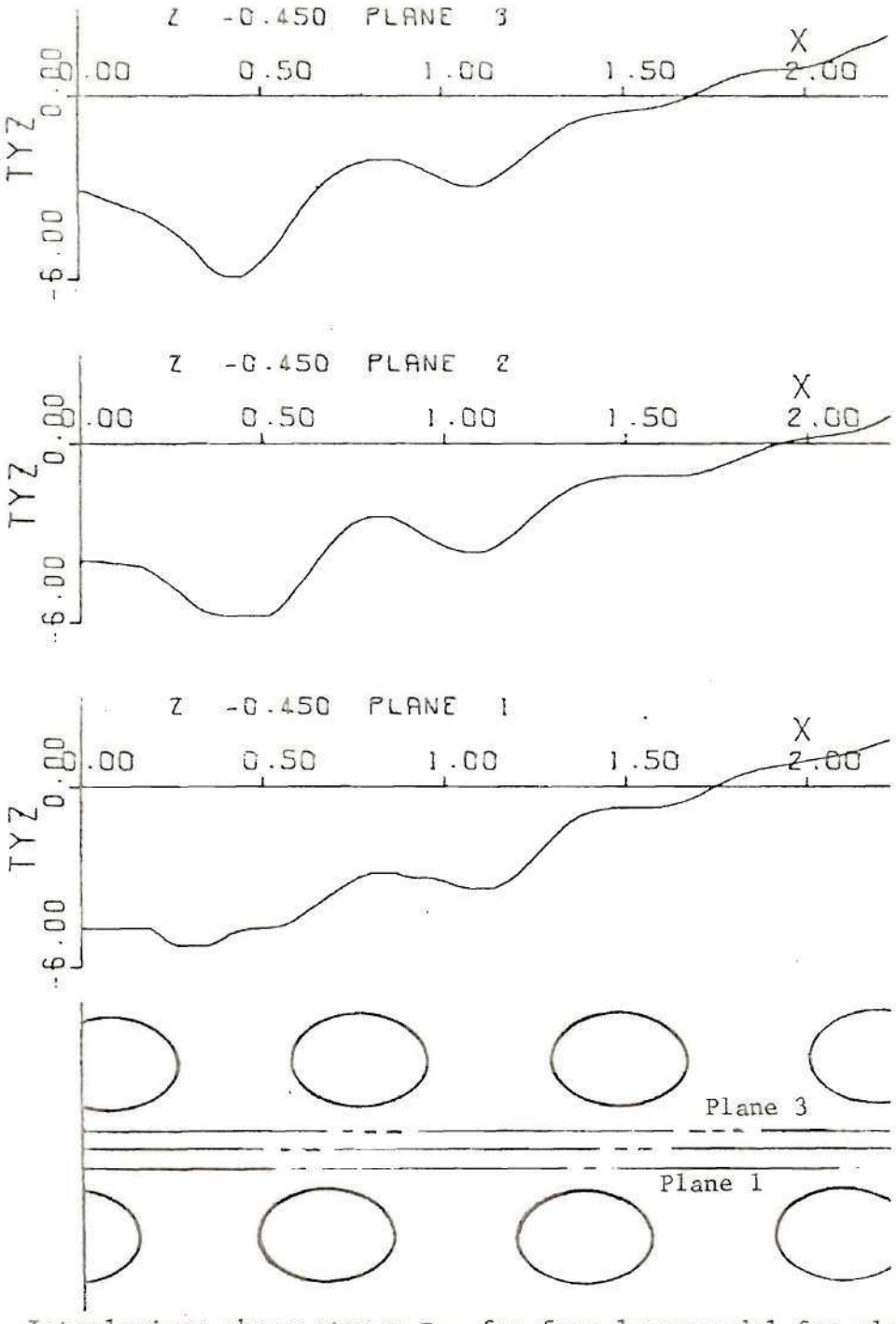

64. Interlaminar shear stress τ_{yz} for four-layer model for planes and z location given. Plane locations and fiber intersections for z locations are given also. Refer to explanation preceding Fig. 55 and to Fig. 5.

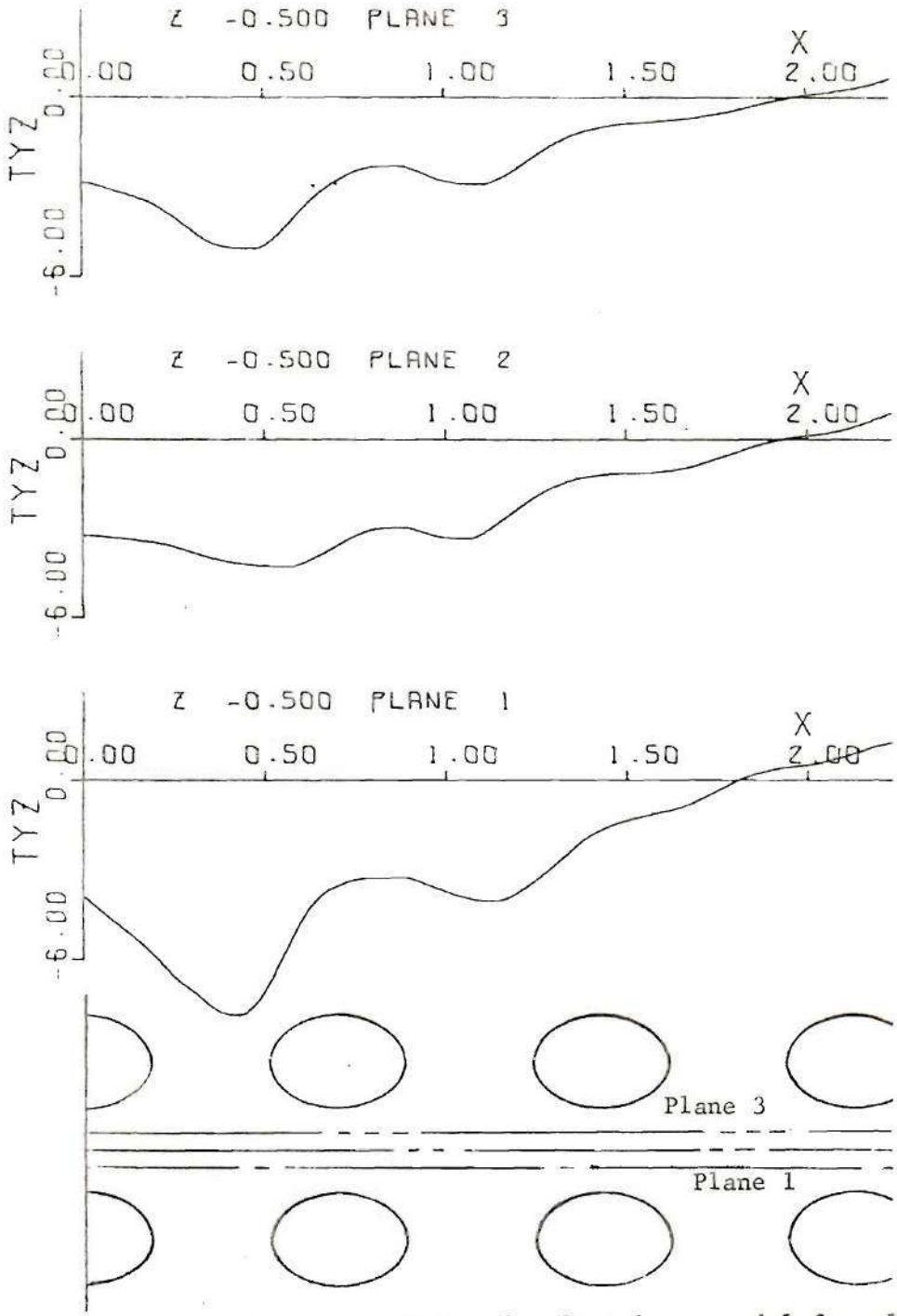

65. Interlaminar shear stress τ_{yz} for four-layer model for planes and z location given. Plane locations and fiber intersections for z locations are given also. Refer to explanation preceding Fig. 55 and to Fig. 5.

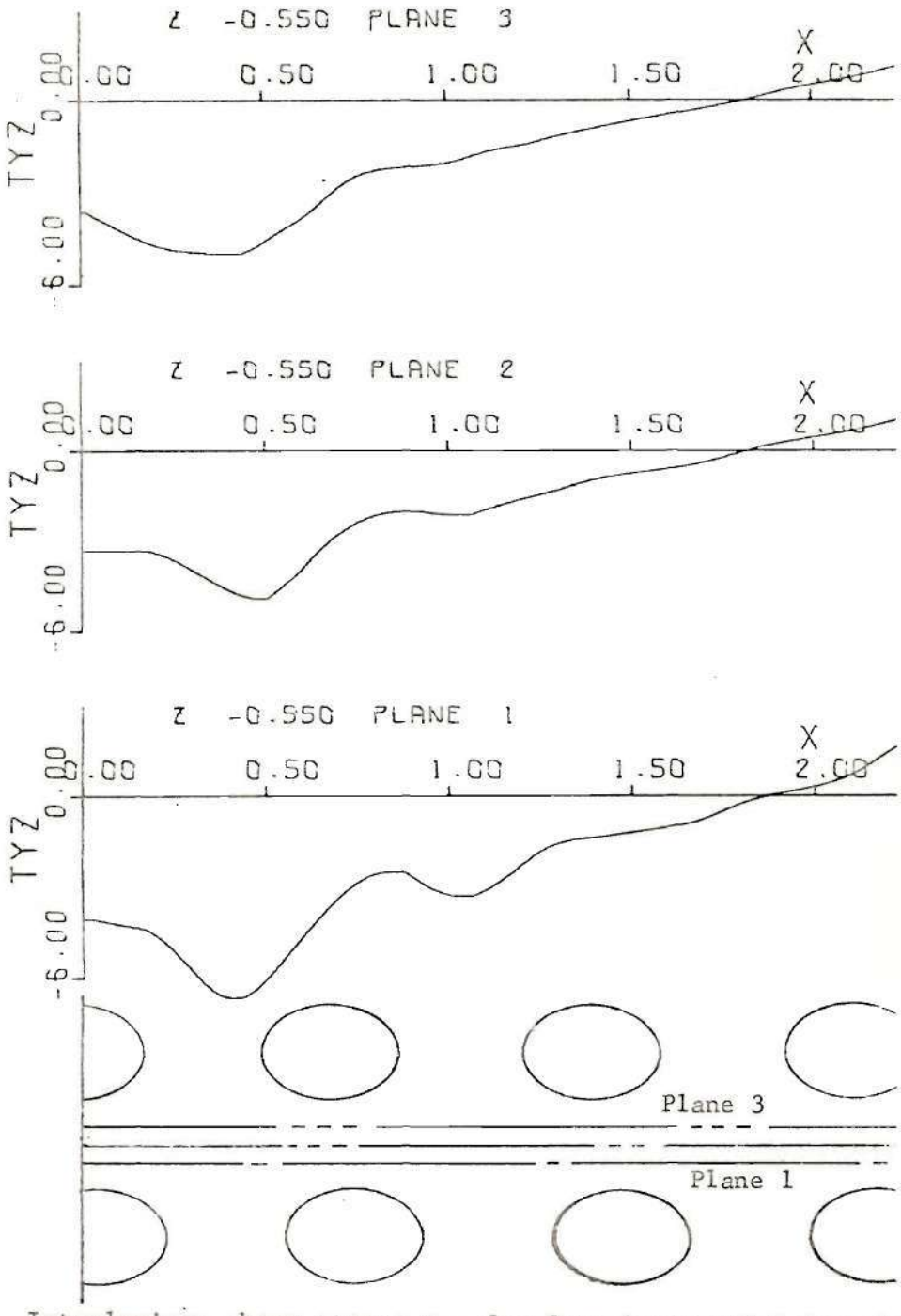

66. Interlaminar shear stress τ_{yz} for four-layer model for planes and z location given. Plane locations and fiber intersections for z locations are given also. Refer to explanation preceding Fig. 55 and to Fig. 5.

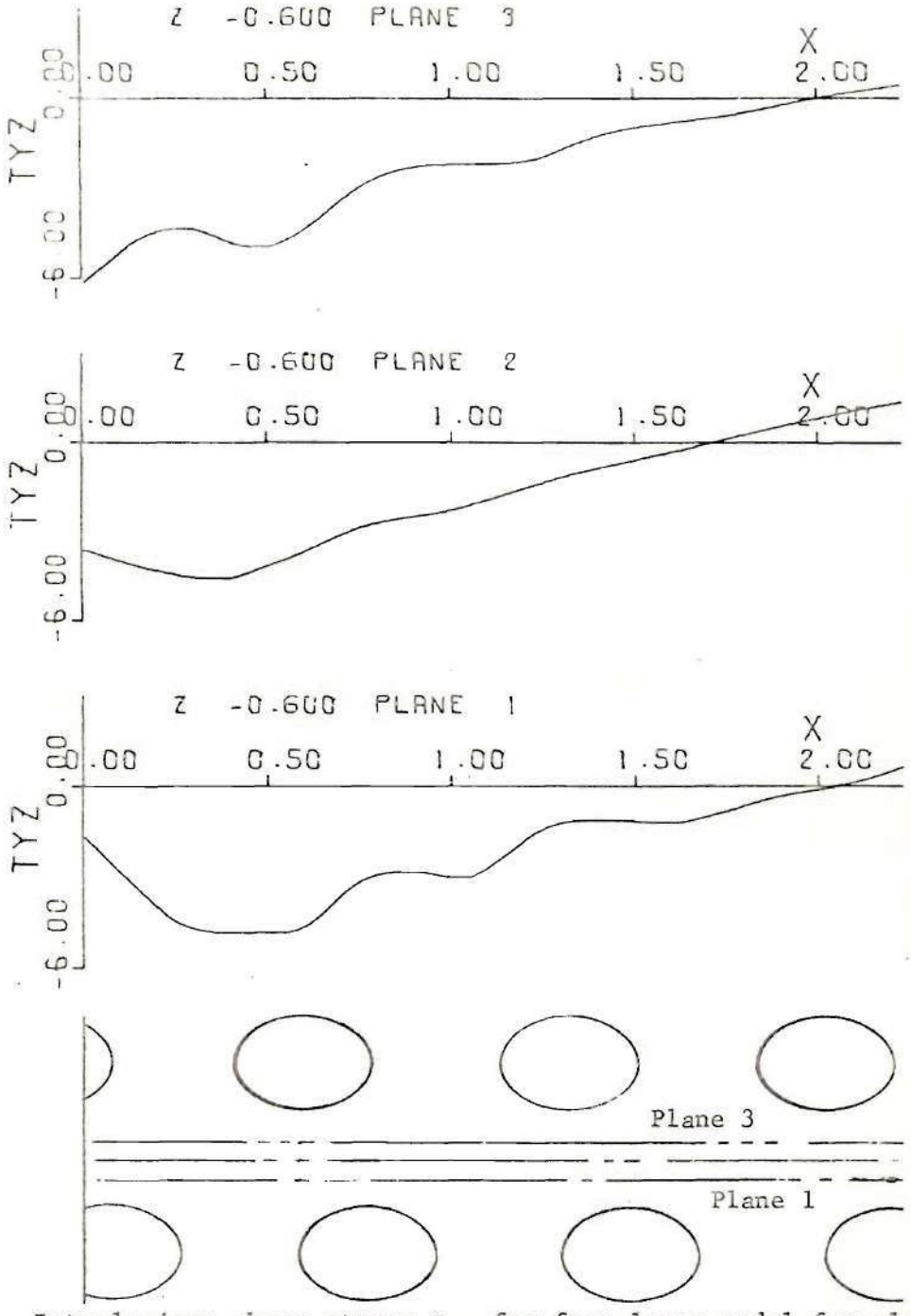

67. Interlaminar shear stress τ_{yz} for four-layer model for planes and z location given. Plane locations and fiber intersections for z locations are given also. Refer to explanation preceding Fig. 55 and to Fig. 5.

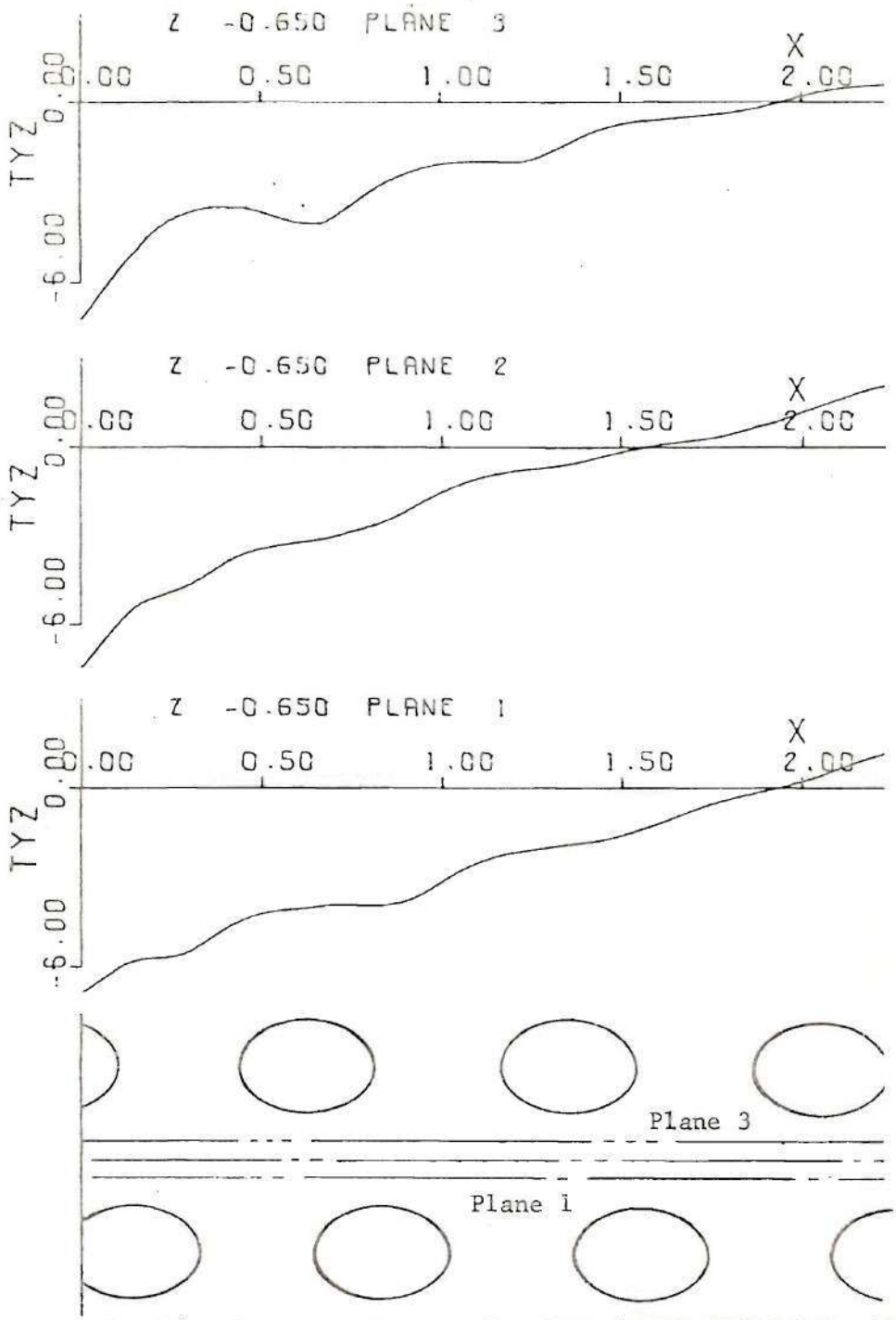

68. Interlaminar shear stress τ_{yz} for four-layer model for planes and z location given. Plane locations and fiber intersections for z locations are given also. Refer to explanation preceding Fig. 55 and to Fig. 5.

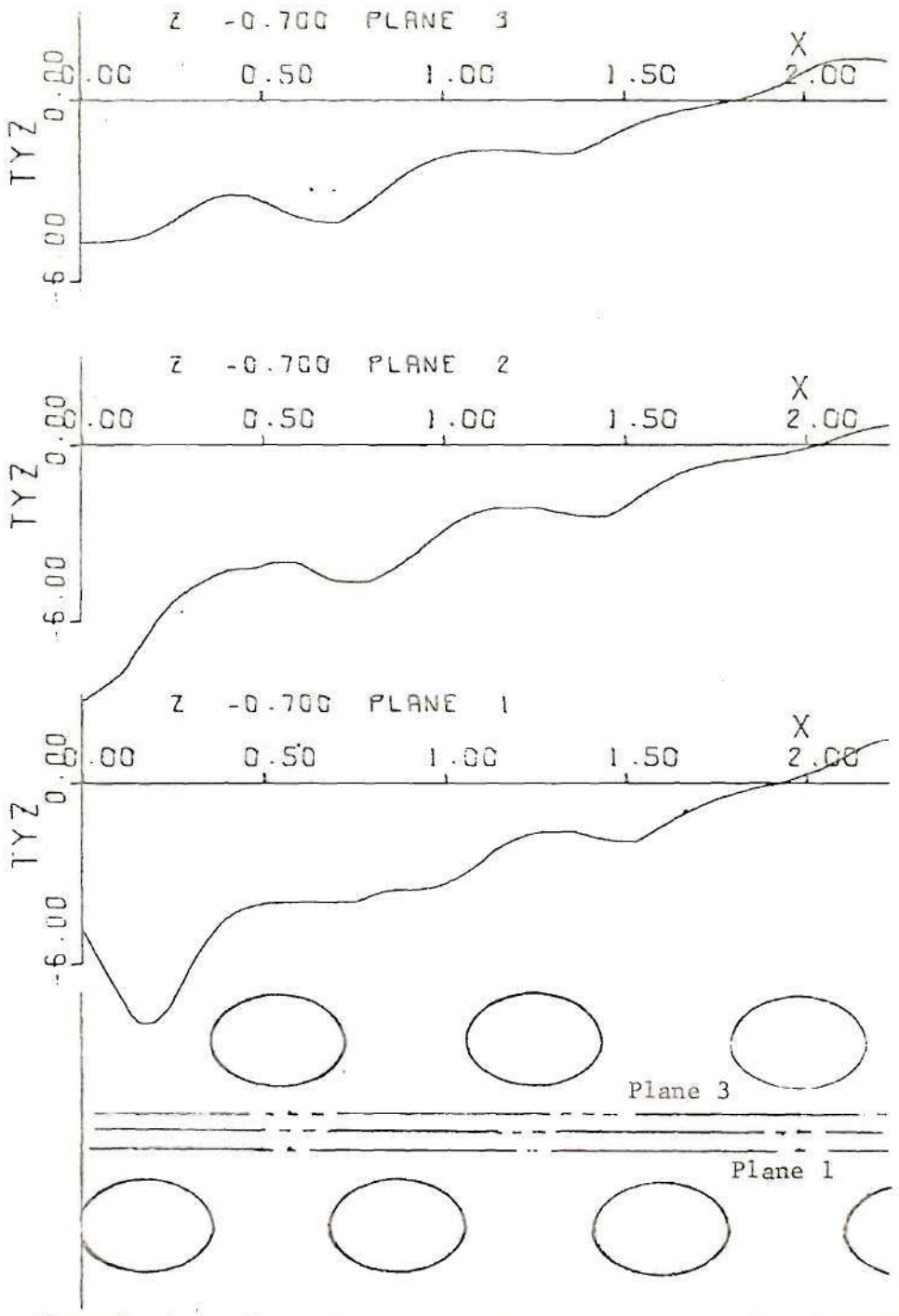

69. Interlaminar shear stress τ_{yz} for four-layer model for planes and z location given. Plane locations and fiber intersections for z locations are given also. Refer to explanation preceding Fig. 55 and to Fig. 5.

APPENDIX A

LEAST SQUARES

An over-determined system of equations may be represented in matrix notation as:

$$[a]\{u\} = \{b\} \tag{1A}$$

where $[a]$ is ℓxm ($\ell > m$) coefficient matrix, u is an mx1 column matrix consisting of the m unknowns and $\{b\}$ is an ℓx1 column matrix containing the right-hand sides of the ℓ equations. A solution to (1A) employing the least squares method is that solution $\{u\}$ which minimizes the sum of the squares of all the residues. The residues are defined by:

$$r_i = \sum_{j=1}^{m} a_{ij} u_j - b_i \tag{2A}$$

Thus, $\{u\}$ is sought such that

$$R = \sum_{i=1}^{\ell} (r_i)^2 = \sum_{i=1}^{\ell} \left(\sum_{j=1}^{m} a_{ij} u_j - b_i \right)^2 \tag{3A}$$

is a minimum. By setting

$$\frac{\partial R}{\partial u_j} = 0 \qquad j = 1, m \tag{4A}$$

the u_j may be found which minimize R and are, therefore, the "best" solution in a least squares sense. Equations (4A) yield a system of m equations in m unknowns. If this new system of equations (4A) has a non-

singular coefficient matrix, a unique solution may be obtained.

Weighting, to express confidence levels in various equations, may be accomplished by modifying (3A) to include a weighting factor (w_i). The expression for R then becomes:

$$R = \sum_{i=1}^{\ell} w_i \sum_{j=1}^{m} (a_{ij} u_j - b_i)^2 \qquad (5A)$$

"The factor w_i has the effect of decreasing or increasing the relative importance of a particular equation. That part of the total residue, R, due to a given equation may be made arbitrarily small or large by adjusting the value of w_i. A small value of w_i (a fraction for example) indicates a relatively low confidence level in the $i^{\underline{th}}$ equation. Confidence levels depend on such factors as experimental accuracy and the validity of the assumptions made in formulating the equations. The effect that the $i^{\underline{th}}$ equation would have on R, and consequently, the values of u_j, depends on the choice of w_i."

APPENDIX B

SMOOTHED CUBIC SPLINES

Reinsch (70) showed that a cubic spline is the solution to the problem of finding a function f (x) which minimizes

$$\int_{x_i}^{x_k} [f''(x)]^2 dx \tag{1B}$$

subject to the constraint condition

$$\sum_{i=1}^{k} [f(x_i) - y_i]^2 < S \sum_{i=1}^{k} (\delta y)^2 \tag{2B}$$

f(x) is the function sought, y_i are the known values of a function dependent on x_i (where $X_{i+1} > X_i$). S represents a smoothing parameter and δy_i is an estimate of the standard deviation expected in y_i. Therefore, the right-hand side of (2B) represents the amount of accumulated variation allowed between $f(x_i)$ and y_i.

A cubic spline satisfies conditions (1B) and (2B). In each interval (X_i, X_{i+1}) the function f(x) is defined by:

$$f(x) = a_i + b_i (x - x_i) + c_i (x - x_i)^2 + d_i (x - x_i)^3 \tag{3B}$$

The coefficients a, b, c and d are calculated according to the procedure outlined by Reinsch.

APPENDIX C

MATRIX LOAD

The portion of the applied load supported by the interlaminar matrix was calculated by finding an average value of σ_1 and applying this over the matrix area. The average value of σ_1 is:

$$\sigma_{1\ avg} = 3.45 \tag{1C}$$

where S = P/A, P is the applied load and A is the cross-sectional area of the model (8 in^2). Thus the load supported by the interlaminar matrix is given by:

$$Pm = \sigma_{1\ avg}\ Am \tag{2C}$$

where Am is the area of the interlaminar matrix subjected to $\sigma_{1\ avg}$. Am is defined by the two lines K = 1 and 4 and the model edges. Thus

$$Am = (.3\ in)\ (4\ in) = 1.2\ in^2 \tag{3C}$$

Substitution of (1C) and (3C) into (2C) yields

$$Pm = (3.4)\left(\frac{P}{8\ in^2}\right)(1.2\ in^2) \tag{4C}$$

or

$$Pm = .51\ P$$

REFERENCES

1. Dietz, A. G. H., Composite Materials, American Society for Testing and Materials, Philadelphia, Penna., 1965.

2. Mullin, J., Berry, J. M., and Gatti, A., "Some Fundamental Fracture Mechanisms Applicable to Advanced Filament Reinforced Composites," Journal of Composite Materials, 2, 1968, pp. 82-103.

3. Hussain, M. A., Pu, S. L., Sadowsky, M. A., "On the Detachments of the Ends of Microfibers from the Matrix Dus to Tension in the Composite," Journal of Composite Materials, 2, 1968, pp. 414-427.

4. Greszczuk, L. B., "Theoretical and Experimental Studies on Properties and Behavior of Filmentary Composites," Proceedings 21st Annual Tech. Conf. SPI Reinforced Plastics Div. Society of the Plastics Ind., Inc. Sec. 8-A, Feb. 1966.

5. Pipes, R. B., Reed, D. L. and Ashton, J. E., "Experimental Determination of Interlaminar Shear Properties of Composite Materials," SESA Paper 1985A, presented at SESA Spring Meeting, Cleveland, Ohio, May 23-26, 1972.

6. Puppo, A. H., and Evenson, H. A., "Interlaminar Shear in Laminated Composites Under Generalized Plane Stress," Journal of Composite Materials, 4, 1970, pp. 204-220.

7. Pipes, B. R., and Pagano, N. J., "Interlaminar Stresses in Composite Laminates Under Uniform Tension," Journal of Composite Materials, 4, 1970, pp. 538-548.

8. Rybiki, E. F., "Approximate Three-Dimensional Solutions for Symmetric Laminates Under Inplane Loading," Journal of Composite Materials, 5, 1971, pp. 354-360.

9. Isakson, G., and Levy, A., "Finite Element Analysis of Shear in Fibrous Composites," Journal of Composite Materials, 5, 1971, pp. 273-276.

10. Whitney, J. M., "Stress Analysis of Thick Laminated Composite and Sandwich Plates," Journal of Composite Materials, 6, 1972, pp. 426-440.

11. Reissner, E., and Stavsky, Y., "Bending and Stretching of Certain Types of Heterogeneous Aelotropic Elastic Plates," Journal of Applied Mechanics, Vol. 28, No. 3, pp. 402-408, 1961.

12. Lekhnitskii, S. G., "Anisotropic Plates," Translated from the second Russian edition by S. W. Tsai and T. Cheron, Gordon and Breach Science Publishers, New York, 1968.

13. Lehnitskii, S. G., "Theory of Elasticity of an Anisotropic Elastic Body," translated by P. Fern, Holden-Day, Inc., San Francisco, 1963.

14. Tyson, W. R. and Davies, G. J., "A Photoelastic Study of the Shear Stresses Associated with the Transfer of Stress During fibre Reinforcement," British Journal of Applied Physics, 16, 1965, pp. 199-205.

15. Schuster, D. M. and Scala, E., "The Mechanical Interaction of Sapphire Whiskers with a Birefringent Matrix," Trans. Metallurgical Soci. AIME, 230, 1964, pp. 1635-1645.

16. MacLaughlin, T. F., "Effect of Fiber Geometry on Stress in Fiber-reinforced Composite Materials," Experimental Mechanics, 6, 1966, pp. 481-492.

17. MacLaughlin, T. F., "A Photoelastic Analysis of Fiber Discontinuities in Composite Materials," Journal of Composite Materials, 2, 1968, pp. 44-55.

18. Schuster, D. M., and Scala, E., "Mechanical Interactions in Fiber Reinforced Photoelastic Composites," Proceedings of a Conference of Fundamental Aspects of Fiber Reinforced Plastic Composites, Dayton, Ohio, May 24-26, 1967.

19. Pih, H., and Sutliff, D. R., "Photoelastic Analyses of Reinforced Composites," AFML-TR-68-380, Air Force Materials Laboratory, Wright-Patterson Air Force Base, Ohio, 1968.

20. Marloff, R. H., and Daniel, J. M., "Three Dimensional Photoelastic Analysis of a Fiber-reinforced Model," Experimental Mechanics, 9, 1969, pp. 156-162.

21. Jenkins, D. R., "Analysis of Behavior Near a Cylindrical Glass Inclusion by Scattered Light Photoelasticity," Experimental Mechanics, 8, 1968, pp. 467-473.

22. Rollins, C. T., "Micromechanic Stresses in Photoelastic Composite Coupons," Paper 2175A presented at Third International Conf. on Experimental Mechanics, Los Angeles, Calif., May 13-18, 1973.

23. Sierakowski, R. L., Nevill, G. E., Jr., Ross, C. A., and Jones, E. R., "Studies of the Dynamic Fracture Characteristics of Composites," AFATL-TR-72-44, Air Force Armament Laboratory, Eglin Air Force Base, Florida.

24. Pagano, N. J., and Chou, P. C., "The Importance of Signs of Shear Stress and Shear Strain in Composites," Journal of Composite Materials, 3, 1969, pp. 166-173.

25. Riley, V. R., "Fibre/Fibre Interaction," Journal of Composite Materials, 2, 1968, pp. 436-446.

26. Dally, J. W., and Alfrevich, J., "Application of Birefringent Coatings to Glass-fiber-reinforced Plastics," Experimental Mechanics, 9, 1969, pp. 97-102.

27. Daniel, I. M., and Rowlands, R. E., "Experimental Stress Analysis of Composite Materials," ASME paper 72-DE-6, presented at ASME Design Engineering Conference, Chicago, May 8-11, 1972.

28. Rowlands, R. E., Daniel, I. M., and Whiteside, J. B., "Stress and Failure Analysis of a Glass-Epoxy Composite with a Circular Hole," Experimental Mechanics, 13, 1973, pp. 31-37.

29. Daniel, I. M., Rowlands, R. E., and Post, D., "Moire Methods for Strain Analysis of Composites," SESA Paper 1995A, presented at SESA Spring Meeting, Cleveland, Ohio, May 23-26, 1972.

30. Pipes, R. B., and Daniel, I. M., "Moire Analysis of the Interlaminar Shear Edge in Laminated Composites," Journal of Composite Materials, 5, 1971, pp. 255-259.

31. Pipes, R. B., and Dalley, J. W., "On the Birefringent Coating Method of Analysis for Fiber-reinforced Laminated Composites," Experimental Mechanics, 12, 1972, pp. 272-277.

32. Sokolnikoff, I. S., Mathematical Theory of Elasticity, McGraw-Hill Book Company, Inc., New York, 1956, pp. 35-39.

33. Truesdell, C., and Toupin, R., "The Classical Field Theories," from Encyclopedia of Physics, Vol. III, edited by S. Flugge, Springer-Verlag, Berlin, 1960, pp. 537-538.

34. Sokolnikoff, I. S., op. cit. pp. 5-23.

35. Tsai, S. W., "Structural Behavior of Composite Materials," NASA CR-71, July 1964.

36. Azzi, V. D., and Tsai, A. W., "Elastic Moduli of Laminated Anisotropic Composites," Experimental Mechanics, 5, 1965, pp. 177-185.

37. Ashton, J. E., Halpin, J. C., and Petit, P. H., Primer on Composite Materials, Technomic Publishing Co., Inc., Stanford, Conn., 1969, Chapter 6.

38. Chou, P. C., Carleone, J., and Hsu, C. M., "Elastic Constraints of Layered Media," Journal of Composite Materials, 6, 1972, pp. 80-93.

39. Whitney, J. M., "Experimental Determination of Shear Modulus of Laminated Fiber Reinforced Composites," Experimental Mechanics, 7, 1967, pp. 447-448.

40. Rose, J. L., "On the Use of Photoelastic Composite Models," Experimental Mechanics, 13, 1973, pp. 59-63.

41. Armenakas, A. E., and Sciammarella, C. A., "Experimental Investigation of the Failure Mechanism of Fiber-reinforced Composites Subjected to Uniaxial Tension," Experimental Mechanics, 13, 1973, pp. 49-58.

42. Pih, H., and Knight, C. E., "Photoelastic Analysis of Anisotropic Fiber Reinforced Composites," Journal of Composite Materials, 3, 1969, pp. 94-107.

43. Sampson, R. C., "A Stress-Optic Law for Photoelastic Analysis of Orthotropic Composites," Experimental Mechanics, 10, 1970, pp. 210-215.

44. Dally, J. W., and Prabhakaran, R., "Photo-orthotropic-elasticity," Experimental Mechanics, 11, 1971, pp. 346-356.

45. Coker, E. G., and Filon, L. H. G., "A Treatise on Photoelasticity," revised by H. T. Jessop, Cambridge University Press, Cambridge, 1957.

46. Frocht, M. M., Photoelasticity, Vol. 1, John Wiley and Sons, Inc., New York, N. Y., 1941, pp. 135-136.

47. Ibid, pp. 334-340.

48. Frocht, M. M., Photoelasticity, Vol. 2, John Wiley and Sons, Inc., New York, N. Y., 1948, pp. 333.

49. Weller, R., "A New Method for Photoelasticity in Three Dimensions," Journal of Applied Physics, 10, 1939, p. 266.

50. Jessop, H. T., "The Scattered Light Method of Exploration of Stresses in Two and Three Dimensional Photoelastic Models," British Journal of Applied Physics, 2, 1951, pp. 249-260.

51. Srinath, L. S., and Frocht, M. M., "Scattered Light in Photoelasticity-Basic Equipment and Techniques," Proc. 4th U. S. National Congress of Applied Mechanics, 1972, pp. 775-781.

52. McKinney, J. M., and Swinson, W. F., "Location of Maximum Secondary Principal Axis in Scattered Light Photoelasticity," Prov. 4th Southeastern Conf. for Theoretical and Applied Mechanics, Pergamon Press, New York, 1970.

53. Frocht, M. M., and Guernsey, R., "A Special Investigation to Develop a General Method for Three-Dimensional Photoelastic Stress Analysis," NACA Technical Note 2822, December, 1972.

54. Frocht, M. M., and Srinath, L. A., "A Non-destructive Method for Three-Dimensional Photoelasticity," Proc. 3rd U. S. National Congress of Applied Mechanics, 1958, pp. 329-337.

55. Taylor, C. E., Bowman, C. E., North, W. B., and Swinson, W. F., "Application of Lasers to Photoelasticity," Experimental Mechanics, 6, 1966, pp. 289-296.

56. Langhaar, H. L., Dimensional Analysis and Theory of Models, John Wiley and Sons, New York, 1951.

57. Azzi, V. D., and Tsai, A. W., "Anisotropic Strength of Composites," Experimental Mechanics, 5, 1965, pp. 283-288.

58. Calcote, L. R., The Analysis of Laminated Composite Structures, John Wiley and Sons, Inc., New York, N. Y., 1951.

59. Sampson, R. C., "A Three Dimensional Photoelastic Method for Analysis of Differential Contraction Stresses," Experimental Mechanics, 3, 1963, pp. 225-234.

60. Berghaus, D. G., Aderholdt, R. W., Buban, J. P., and Womack, D. R., "Instrumentation Improvements for Scattered Light Photoelasticity," submitted for publication to Experimental Mechanics.

61. Berghaus, D. G., and Cannon, J. P., "Obtaining Derivatives from Experimental Data Using Smoothed-Spline Functions," Experimental Mechanics, 13, 1973, pp. 38-42.

62. Berghaus, D. G., "Overdetermined Photoelastic Solutions Using Least Squares," Experimental Mechanics, 13, 1973, pp. 97-104

63. Sokolnikoff, I. S., op. cit. pp. 40-42.

64. Frocht, M. M., op. cit. 2, Chapter 8.

65. Sokolnikoff, I. S., op. cit. pp. 42-44.

66. Tsai, A. W., Private communication to A. G. H. Dietz, published in Composite Engineering Laminates, MIT Press, Cambridge, Mass., 1969, p. 141.

67. Daniel, I. M., unpublished results from IIT Research Institute, Chicago, Ill., from Modern Composite Materials by Broutman and Krock, Addison Wesley Publishing Co., Reading, Mass., 1967.

68. McGarry, F. J., "Composite Structural Materials," Experimental Mechanics, 6, 1966, pp. 331-336.

69. Kies, J. A., "Maximum Strains in the Resin of Fiberglass Composites," NRL-5752, March, 1962.

70. Reinsch, C. H., "Smoothing by Spline Functions," Namerische Mathematik 10, (1967) pp. 177-183.

VITA

Robert W. Aderholdt, the son of Wendell H. and Sarah (Rivers) Aderholdt, was born in Jacksonville, Alabama on July 31, 1941. After attending the public schools in Calhoun, County, he was graduated from high school in 1959. He enrolled at Auburn University in September, 1960 and received the degree of Mechanical Engineering in March, 1966. While attending Auburn University, he participated in the co-operative education program.

After working for a year at Arnold Research Organization, he re-enrolled at Auburn University and received a Master of Science in Mechanical Engineering in March, 1969. He was employed as an instructor at Auburn University until June, 1970.

He is a member of Phi Kappa Phi honor society and the Society of the Sigma Xi.

In 1965 he married Carol Ann Thrasher, daughter of Tom L. and Annie (Davis) Thrasher of Gadsden, Alabama. They have two children, Susan and Mark.